ABSTRACT

Title of dissertation: MULTIVARIATE RETRIEVAL OF CARBON MONOXIDE

R. Chris Wilson, Doctor of Philosophy, 2011

Dissertation directed by: Professor W. Wallace McMillan
Professor Raymond Hoff
Department of Physics

A new technique is presented here to retrieve carbon monoxide (CO) profiles from Atmospheric Emitted Radiance Interferometer (AERI) spectra. This retrieval version deviates from the previous AERI CO retrieval method, which utilized signal processing to determine a constant CO mixing ratio representative of the entire troposphere. Instead, this retrieval version utilizes linear mapping to ascertain an estimate of the CO profile. A detailed analysis is conducted to estimate the error from all aspects of the the linear mapping procedure including measurements, forward modeling of atmospheric radiation, and uncertainty from inputs to the forward model. It was found that the dominant sources of error were from cloud contaminated spectra and uncertainty in absorption line strengths inside the forward model. A new cloud flagging technique that uses a neural network to identify spectra affected by clouds was tested and compared to the previously used version based on brightness temperature contrast. The neural network method decreased uncertainty between AERI and forward model spectra by 30 percent when compared with the

previously used version.

First guess CO profiles to the AERI retrieval were from two different sources. One source was an *a priori* CO profile calculated as the mean profile from 56 individual measurements where each CO profile encompasses tower, aircraft, and satellite CO measurements. The other first guess CO profile came from the AIRS version 5 (AIRSv5) retrieved CO product. Incorporating the AIRS CO profile to the AERI retrieval provided a better estimate of free tropospheric CO when compared with the *a priori* profile. Using a better upper tropospheric CO estimate resulted in more accurate results from the AERI retrieval below 2 km, thus revealing that an AERI plus AIRS retrieved CO product is superior to either instrument's own CO retrieval working alone. The combined retrieval product is shown to have an RMSE of 10% in the first 2 km of the atmosphere.

Multivariate Retrieval of Carbon Monoxide

by

Chris Wilson

Dissertation submitted to the Faculty of the Graduate School of the
University of Maryland, Baltimore County in partial fulfillment
of the requirements for the degree of
Doctor of Philosophy
2011

Advisory Committee:
Professor Raymond Hoff, Chair/Advisor
Dr. Eric Maddy
Professor Lynn Sparling
Professor Kevin McCann
Dr. Juying Warner

Dedication

To Wallace McMillan

Acknowledgments

It is with great joy that after 7 years of graduate school I finally get to write the acknowledgements for my dissertation.

First I would like to express thanks and appreciation to the physics staff at Westminster College. I have so many fond memories of this time including building homemade potato cannons, helping with planetarium shows, and watching Dr. Sam Lightner lay on a bed of nails. Specifically, I would like to thank Dr. William Johnson who taught me how to break down physics problems into their most basic parts. He commonly would say to me, "What is the law that behind this problem", and I still use this thought process to begin a problem. I would like to thank Dr. Craig Caylor. Near the end of my studies at Westminster I frequently would go to him for advice on many topics, including grad school, help in classes, or just life. Much of my success in my graduate school classes is due to the great education I received from the physics department at Westminster.

I owe much gratitude to my parents and grandparents who stressed the importance of a good education from as early as I can remember. My parents have supported me in so many ways over the years that it would have been impossible to complete this degree without them.

I have a deep sense of appreciation for my time I spent with Dr. Wallace McMillan. He was my advisor for the first 6 years of my graduate study. I am so fortunate to have an advisor who took so much time and care to ensure I always had the support I needed to succeed. Wallace was a unique person who loved his

ties, loved his trains, and always made time for his students. His unexpected and tragic loss is certainly felt by his colleagues, friends, family, and myself. Something I will always remember is Wallace telling me how proud of the progress I have made just before he passed. Let his unexpected passing remind all of us how important life is and that we must remember to invest time in developing relationships with the people we interact with on a daily basis.

Many people throughout the UMBC community came out to support me after the unexpected passing of my advisor. I need to thank Dr. Michael Hayden (Department Chair) and Dr. Vanderlei Martins (Graduate program director). These two people assured me that the Physics department would do whatever it took to help me to graduate. I am sure they were partly responsible for bringing back the Inverse Methods class that was so instrumental in developing my understanding of retrievals.

I owe so much to everyone on my committee and extend the deepest thanks. Dr. Juying Warner and Dr. Eric Maddy have done so much this past year to help me understand the mysteries of retrievals. They co-taught the Inverse Methods class whose theory formed the basis for my entire dissertation. Moreover, each one of acted as pseudo-advisors and experts in the field for me. I have had many correspondences and meetings with each one this past year and a half and appreciate all their work and patience they had with reading my dissertation.

I would like to thank my current advisor, Dr. Ray Hoff, who constantly pushed me to think about the broader picture of my project and spent countless amount of hours helping me to editing different versions of my dissertation. Dr. Lynn Sparling

and Dr. Kevin McCann made up the rest of my committee. I thank them and my entire committee for the patience they had with me while I had to start a job while finishing my degree.

There are so many friends who in my most stressful of times showed me great friendship. I thank the Salemis, who at a difficult time for me opened up their house and gave me a home. I thank Dr. Debra Wicks, who has been my lab mate the entire time at UMBC. Debra is very organized and always took care to remind me of any important date or note for a class. It has been a long road to graduation for the both of us. I am happy to call her a colleague of mine. I would like to a few of my other friends and roommates who I always could count on for good conversations, "muscle" to help me in one of my many moves, or just to physically push me up hills while running. These guys include Dr. Justin Hackley, Dr. Vincenzoo Tamma, Barry Baker, and Jason Simon. I am grateful for the time I spent playing ultimate frisbee at UMBC and have so many wonderful friends from Booya.

I need to thank Tiffany Hughes. Her love, support, and patience made a hard project much easier. She has spent countless hours helping me edit my dissertation as "dissertation station" moved across the country. The quality of this dissertation is a direct reflection of her significant abilities. I am forever in debt to her for all the sacrifices she made that allowed me to work nights finishing up the dissertation while she setup our new home in California. I greatly look forward to spending some fun and relaxing time with her.

Lastly, I need to acknowledge all the different organizations that provided data and support that were critical to my dissertation.

The hardware used in the computational studies is part of the UMBC High Performance Computing Facility (HPCF). The facility is supported by the U.S. National Science Foundation through the MRI program (grant no. CNS–0821258) and the SCREMS program (grant no. DMS–0821311), with additional substantial support from the University of Maryland, Baltimore County (UMBC). See `www.umbc.edu/hpcf` for more information on HPCF and the projects using its resources.

The results of this work would not have been possible without the well calibrated field data supplied by the Atmospheric Radiation Measurement Climate Research Facility that is supported by the U.S. Department of Energy. This facility provided the AERI-01 and MWR data that were critical to this project.

I should acknowledge Dr. Dave Turner who provided me with Neural Network Cloud flags that I used to determine when clear skies were present above the AERI-01 instrument.

It is impossible to thank everyone that may have been left out. So in conclusion, thank you all and thank God!

Table of Contents

List of Tables x

List of Figures xi

List of Abbreviations xviii

1 Introduction and Outline 1
- 1.1 Introduction . . . 1
- 1.2 Role in Tropospheric Ozone . . . 3
- 1.3 Previous CO Retrieval Studies . . . 5
  - 1.3.1 Previous Modeled Error Analysis . . . 6
- 1.4 New Techniques and Major Results . . . 9
  - 1.4.1 New Error Analysis . . . 9
  - 1.4.2 New Retrieval Techniques . . . 11
- 1.5 Outline . . . 12

2 Measurements, Models, and Theory 16
- 2.1 Tower . . . 16
- 2.2 Airplanes Profiles . . . 16
- 2.3 AIRS . . . 17
- 2.4 Radiative Transfer . . . 19
- 2.5 Forward Model . . . 26
  - 2.5.1 kCARTA . . . 26
  - 2.5.2 Carbon Monoxide Input Profiles . . . 27
  - 2.5.3 Water Vapor Continuum Modeling . . . 31
  - 2.5.4 kCARTA Grids . . . 32
- 2.6 AERI . . . 33
  - 2.6.1 Apodizing AERI and kCARTA . . . 37
  - 2.6.2 AERI Meteorological Profiles and Other Uses . . . 40
- 2.7 MWR . . . 43
- 2.8 Error Theory . . . 44
- 2.9 Retrieval Theory . . . 46
  - 2.9.1 Problem Formulation . . . 46
  - 2.9.2 Jacobians . . . 48
  - 2.9.3 Least Square Solution . . . 49
  - 2.9.4 First Guess . . . 55
  - 2.9.5 Information Content . . . 56
  - 2.9.6 Degrees of Freedom, Gain Matrix, and the Averaging Kernel . 57
  - 2.9.7 Shannon Information Content (H_S) . . . 59

3 Error Analysis 61
3.1 Cloud Filtering . . . 61
3.2 kCARTA Input Analysis . . . 65
3.3 Error Simulations . . . 67
3.3.1 Temperature Simulation . . . 69
3.3.2 Water Vapor Profile Simulation . . . 71
3.3.2.1 MWR Constraint Simulation . . . 72
3.3.3 kCARTA Model Error . . . 74
3.3.4 AERI Error Simulation . . . 76
3.3.5 Error Simulation Final Results . . . 82
3.4 Direct Comparison: AERI vs kCARTA . . . 84
3.5 Error Analysis Conclusions . . . 92

4 SAAC Retrieval Setup 96
4.1 Retrieval Grid . . . 97
4.1.1 CO Layer Linear Dependence . . . 100
4.1.2 *a priori Variance* . . . 100
4.2 Linearity . . . 102
4.3 Retrieval Equations . . . 108
4.3.1 Nearly Linear Solution (LSQ) . . . 108
4.3.2 Moderately non-linear (LSQwAP) . . . 112
4.3.3 Constraint Matrix (H_{TT}) . . . 113
4.4 Error Covariance Matrix . . . 115
4.4.1 Total Model Error Covariance (S_f) . . . 117
4.4.1.1 kCARTA Input Covariance (S_{temp},S_{h2o}) . . . 118
4.4.1.2 kCARTA Model Covariance (S_{mod}) . . . 121
4.4.2 AERI Error Covariance (S_y) . . . 122
4.5 Channel Selection . . . 124
4.5.1 Final Error Covariance Matrices . . . 128
4.6 Information Content of the Retrieval . . . 129
4.7 Retrieval Update . . . 131
4.7.1 First Guess profiles . . . 135

5 SAAC Retrieval System 137
5.1 Spectral Tuning Effect (Centering) . . . 138
5.2 SAAC vs. Version 1 CO Retrieval . . . 141
5.3 Retrieval Grid Layer Analysis . . . 141
5.3.1 LSQ Trials . . . 141
5.3.2 LSQwAP Trials . . . 145
5.4 Single Day Profile . . . 150
5.5 SAAC Conclusions . . . 152

6 SAAC plus AIRS 156
6.1 An Example Profile . . . 157
6.1.1 LSQwAP . . . 158
6.1.2 LSQ and Type of Problem . . . 159
6.2 Error Statistics . . . 162
6.3 Future Uses and Work . . . 164
6.4 Conclusion . . . 167

A AIRSv5 vs *A priori* First Guess 170

Bibliography 176

List of Tables

1.1 Two studies examining radiance difference of window channels. Input WVMR specifies what type of water vapor mixing ratio (WVMR) profile is used in the study. 9

2.1 Expected values of observed minus simulated radiance calculations for a perturbation in a gas profile. Also shown is the change in transmittance. This is for tropospheric sounding only; in the stratosphere, each situation is reversed because the sign of the lapse rate changes. . 22
2.2 Surface pressure in millibars (mb) for different grids developed for AERI. 32

3.1 Summary of cloud analysis on 2007 AERI data 64
3.2 Percent changes to absorption coefficients used to calculate σ terms. . 75
3.3 Mean standard deviation calculations $\left(\frac{mW}{m^2\ sr\ cm^{-1}}\right)$ between AERI and kCARTA simulations for different models, cloud clearing, and MWR input. For each combination of kCARTA version, continuum model, MWR input, and cloud filter, the bias is calculated and added to the simulated kCARTA spectra. Spectral score calculations for these kCARTA simulations represent the centered column. 89

4.1 Height Boundaries for the different retrieval grids in meters. TOA means top of atmosphere as defined in each RTP profile. 98
4.2 **5 Layer *a priori***: Note that the *a priori* is on the order of 10^{17}. p_{eff} is the mean p_{eff} for all 57 retrieval grids in a 5 layer scheme. . . 102
4.3 **3 Layer *a priori***: Note that the *a priori* is on the order of 10^{17}. p_{eff} is the mean p_{eff} for all 57 retrieval grids in a 5 layer scheme. . . 102
4.4 **2 Layer *a priori***: Note that the *a priori* is on the order of 10^{18}. p_{eff} is the mean p_{eff} for all 57 retrieval grids in a 5 layer scheme. . . 103
4.5 The channel indices and corresponding wavenumber from the AERI instrument used in the retrieval are shown. These are the base 19 channel indices that were common to all of the different layer and constraint schemes. 127
4.6 DOF are shown here for the different layering schemes using the H_{TT} constraint matrix. 128

5.1 28 dates corresponding to true composite CO profiles which were determined to be free of clouds by the NN cloud flag. Each date contained one measured true profile around local noon at the SGP site. 137
5.2 Linear regression coefficients for retrieval trials using no bias, BT bias, and NN bias spectrums. These trials compute linear regression coefficients from retrieved vs. *in situ* total column CO measurements, where both LSQ and LSQwAP retrieval equations are used. Root mean square error (RMSE) computed as a percent error (%) as well. . 139

5.3 Linear regression coefficients for retrieval trials using 2, 3 and 5 layer retrieval grids. These trials compute linear regression coefficients from retrieved vs. *in situ* total column CO measurements, where both BT or NN bias spectrums are used. Root mean square error (RMSE) computed as a percent error (%) as well. All results in this table are for the LSQ retrieval. 146
5.4 Linear regression coefficients for retrieval trials using 2, 3 and 5 layer retrieval grids. These trials compute linear regression coefficients from retrieved vs. *in situ* total column CO measurements, where both BT or NN bias spectrums are used. Root mean square error (RMSE) computed as a percent error (%) as well. This is for the LSQwAP retrieval equation 149

6.1 Cloud-free dates where AIRS first guess profiles from [89] match up well with the upper portion of the true composite CO profiles. Cloud clearing is done using the neural network discussed in Section 3.1. . . 157
6.2 Data taking periods for satellites measuring CO profiles [9]. 166

List of Figures

1.1 Version 1 AERI retrieved CO compared with convolved *in situ* measurements. This graph was taken from [90]. 7
1.2 (a) Average radiance difference in window channels 2142.7-2144.1 cm^{-1} and 2167.2-2168.7 cm^{-1} plotted as a function of PWV. Synthetic spectra was calculated using retrieved water vapor profiles from AERI as input to kCARTA. This plot was taken from [90]. (b) Average radiance difference in 900 cm^{-1} window channel. This was taken from [82], where Case B signifies that the input to the line by line radiative transfer model (LBLRTM) were radiosondes scaled by PWV from an MWR. Note the functional similarity among the two graphs despite using different water vapor input profiles and forward models used to calculate the synthetic spectra. 8
1.3 A schematic showing the setup of all the measurements used in the study. 13

2.1 (a) AIRSv5 CO bias estimates defined as AIRS - Truth. (b) AIRSv5 CO RMS estimates. Both figures were taken from [47] 18
2.2 AERI radiance compared to blackbodies emitting radiance with their temperatures in K listed in the label. 21
2.3 (a) A simulated AERI weighting function created from kCARTA simulation and apodized to AERI resolution. (b) A simulated AIRS weighting function from kCARTA apodized to AIRS resolution. Both figures cover the spectral range used in their respective CO retrievals [47]. 24

2.4 (a) True CO profile (blue) is 20070126 profile from [90]. The First Guess CO profile is the *a priori* for the data set defined on a 101 level grid with the surface defined at 980 mb. (b) This figure displays how the input CO is merged from its grid of 10 - 15 levels to a 100 level grid that is read into KLAYERS. 29
2.5 This figure shows profiles defined on the 100 layers capable of being read into kCARTA. Truth is the same profile from Figures 2.4(a) and 2.4(b) once it has been converted to column density by KLAYERS. The *a priori* is first guess profile from Figure 2.4(a) 30
2.6 (top) AERI long-wave channel. Portions of the spectra sensitive to certain gases are labeled. Red portions of spectra are used in the temperature retrieval and blue portions are used in the water vapor retrieval [72, 22]. (bottom) The short-wave channel of AERI with the CO region highlighted as well. 34
2.7 An illustration representing the setup of the AERI interferometer. Only the shortwave portion of the radiation is absorbed by the InSb detector, and allows the long-wave to pass through to the HgCdTe detector. 35
2.8 (a) Top graph is Norton-Beer apodization function used in the convolution of the interferogram of kCARTA and AERI spectra. Bottom graph is a boxcar apodization function which is the natural apodization function of a non-infinite FTIR such as AERI. (b) Response functions in spectral space of the Norton-Beer (Blue) and Boxcar (Red) apodization functions. 38
2.9 Noise Correlation coefficients measured as a function of distance away from band center (v_o) using units of wavenumber cm^{-1}. 39
2.10 Process to apodize spectra from kCARTA or an AERI measurement. IFFT stands for an Inverse Fast Fourier Transform and FFT stands for a Fast Fourier Transform. A_{NB}(d) is the NB apodization function used to multiply the interferogram I(d), where d is path length. $I(\nu)$ represents spectra from either AERI or kCARTA. 40
2.11 This figure, taken from [72], provides the validation results for the AERI temperature water vapor retrieval. The error statistics shown here are used in Chapter 3 to determine modeled spectral error due to errors in AERI retrieved temperature and water vapor profiles. . . 42
2.12 (a) Displays a time series for one day of retrieved PWV and retrieved CO. The top part of the graph is the measured PWV measured by AERI (purple) and MWR (grey) with its axis on the left. The bottom part of the graph is the version 1 CO retrieval with its axis on the left. The red time series represents the CO retrieval using water vapor profiles from AERI as input to kCARTA. The black time series represents the CO retrieval using constrained water vapor profiles as input to kCARTA. This figure is taken from [90] 45

2.13 (a) AIRS v5 AK with the effective pressures for each row of the AK listed in the legend. This plot comes from [87]. (b) SAAC averaging kernel. The components for this retrieval use a diagonal constraint matrix called H_{TT} and a 5 layer retrieval grid. These components are defined in Chapter 4. 56

3.1 Time Series of AERI spectra converted to brightness temperatures for 20070106 from AERI-01 instrument located at SGP. 62
3.2 Cloud climatology plot from [80]. Clouds are flagged via a neural network, and 250 (K) was chosen as a threshold between thin and thick clouds. 63
3.3 (a) Histogram cloud analysis on all AERI-01 spectra by the neural network method. (b) Histogram cloud analysis on all AERI-01 spectra using brightness temperature contrast to search for clouds. 65
3.4 (a) Temperature, water vapor, and CO Jacobians. Water and CO Jacobians are multiplied by a 10 percent variation of their gases column amount. Temperature Jacobian is for a 1K difference. Noise level is simulated as 1 percent of the measured radiance. (b) N_2O Jacobian is calculated using Equation 2.15 with a 1% perturbation.(c) O_3 Jacobian is calculated using Equation 2.15 with a 1% perturbation. (d) CO_2 Jacobian is calculated using Equation 2.15 with a 1% perturbation. For (b) - (d) CO Jacobian calculated by Equation 2.15 using a 10% perturbation. The perturbation sizes are chosen to assure the radiative transfer equation is approximately linear for a given percent change in gas amount. 68
3.5 Bias and RMS profiles for the AERI retrieved temperature product taken from an AERI temperature and water vapor validation study [72]. 69
3.6 Output profiles of RMS and bias once error is added to the temperature profile. Bias is calculated as the mean of $T - T_{error}$ 71
3.7 (a) Bias and RMS profiles for the AERI retrieved WVMR product taken from an AERI temperature and water vapor validation study [72]. These are used in Equations 3.6 and 3.7. (b) Bias and RMS statistics calculated between W and W_{error}. The constrained RMS and bias profiles are calculated from W and W_{error}, where W_{error} is constrained by a simulated MWR measurement. Equation 3.10 demonstrates how the WVMR profile is constrained by use of an MWR. Bias is calculated as the mean of $W - W_{error}$. 73
3.8 (a) All the different terms used to model the uncertainty kCARTA modeling error measured in brightness temperature (K). (b) Total modeled error, total water error, and error terms from CO are presented here in radiance units. Total water is the uncertainty in water lines, self broadening, and foreign broadening. Total is all the terms added together. Error terms are added together using equation 3.12 . 77

3.9 (a) FI function (red) for apodized AERI data set with the blue star corresponding to the minimum.(c) FI function (red) for unapodized AERI data set with blue star corresponding to the minimum. 80
3.10 (a)Eigenvalues (Red) for apodized AERI data set with blue star corresponding to the minimum in the FI function. (d) Eigenvalues (Red) for unapodized AERI data set with blue star corresponding to the minimum in the FI function. 81
3.11 (a) Reconstruction example of apodized AERI spectra (b) RMS error from the difference between the original AERI (L_{mxn}) and the reconstructed datasets (L^{low}_{mxn}). 83
3.12 Estimated error terms used to constrain the CO retrieval. *Modeled* represents all error terms estimated from kCARTA modeling added in quadrature. *Input temp* and *Input Water* are the estimated error terms that are created from the large random number simulation involving propagation of validated error in the Feltz data set. *Instrument* displays the instrument error resulting from PCA performed on the 2007 apodized AERI data set. *Ret Indices* are channels used in the retrieval. 85
3.13 (a) Bias and standard deviation measured for all 57 profiles. (b) Bias and standard deviation measured for 54 profiles filtered by BT contrast method. (c) Bias and standard deviation measured for 28 profiles filtered by the NN. 87
3.14 Histograms of the mean absolute brightness temperature difference between 2107 - 2189 cm^{-1}. No cloud filtering is performed and synthetic observations were created using kCARTA version 115, mtckd1, and no constraints from the MWR. 90
3.15 (a) Seasonal variation of MWR collocated with the CO measurements. (b) - (d) represent time series of mean difference between spectra from AERI and kCARTA for the spectral region 2107 - 2189 cm^{-1}. The model combinations are: (b) Centered and not constrained by MWR (c) Centered and constrained by MWR (d) Non centered and constrained by MWR. All cases are computed using kCARTA version 115, MT_CKD 1, true composite CO profiles, and were not cloudy as determined by the NN cloud flags. (b) and (c) are centered by adding the the bias corresponding to NN filtered data. 93

4.1 (a) Two layer retrieval grid used for the retrieval of CO. (b) Three layer retrieval grid used for the retrieval of CO. (c) Five retrieval layer grid used for the retrieval of CO. In each figure blue stars represent the RTP profiles read by kCARTA. The colored lines represent the super layers described above. 99
4.2 A three layer Jacobian comparison. This three layer Jacobian corresponds to the 3 layer scheme shown in Figure 4.1(b). Each Jacobian is calculated by perturbing the CO in the RTP layers encapsulated in the super layer by 10%. 101

4.3 Examples of linear, nearly linear, and moderately non-linear functions. Also shown is how the Jacobian would calculate y for a given step size of Δx. The Jacobian is not shown for the linear case because it would be the same as $f(x)$. 104
4.4 Two level linearity analysis. Each figure represents the percent difference between using a linear approximation (K) and true linear relationship (M) for a given step size in CO (Δx_n). The top graph is the result from perturbing the first 23 layers in the RTP CO profile (979-890mb). The bottom graph is the result from perturbing the layers with pressures between 878 and 729 mb in the RTP CO profile. In the Legend, "$New - base$" represents the 10% perturbation that is used to calculate kCARTA Jacobians. "$Manual - Base$" represents the percent uncertainty calculation from Equation 4.8 107
4.5 (a) - (d) represent the full error covariance (S_e) calculated using Equation 4.28. The full CO band from 2080 - 2197 (cm^{-1} is broken up into 4 spectral intervals.) 116
4.6 (a) through (d) represent the error covariance from uncertainties in temperature profiles used by kCARTA (S_{Temp}). The full CO band from 2080 - 2197 (cm^{-1} is broken up into four spectral intervals.) . . 119
4.7 (a) through (d) represent the error covariance from uncertainties in water profiles used in kCARTA (S_{water}). The full CO band from 2080 - 2197 (cm^{-1} is broken up into four spectral intervals.) 120
4.8 Displays the correlation among channels from a Beer apodization [39] 121
4.9 (a) through (d) represent the error covariance from uncertainties in absorption lines used by kCARTA to calculate synthetic spectra (S_{mod}). This is the total of all different modeling terms ($S_{modwater}, S_{self}, S_{foreign}, S_{CO}$). The full CO band from 2080 - 2197 (cm^{-1} is broken up into four spectral intervals. 123
4.10 (a) Plot of indices that increased H by more than 0.02. (b) The first layer Jacobian defined on the 2 layer retrieval grid. The retrieval indices used are plotted in red as well. 127
4.11 (a) through (d) show the covariance matrices for modeled kCARTA error, Input Water, Input Temperature, and total error respectively. Retrieval indice # correspond to the 21 channel indices listed in table 4.5. Retrieval indice # 1 starts with AERI channel index 665. . . 130
4.12 The estimated error covariance matrix (S_y) due to instrumental uncertainty. 131
4.13 (a) 2 layer AK for 20070218. (b) A 3 layer AK for the same day. (c) A 5 layer scheme for the same day. All three averaging kernels are calculated using Equation 2.28. 132
4.14 (a) 2 layer cumulative DOF for 20070218. (b) 3 layer cumulative DOF for 20070218. (c) Same as (a) and (b), except for 5 layers. Each cumulative sum is calculated along the diagonal of the corresponding averaging kernels shown in Figures 4.13(a)- 4.13(c). 133

5.1 Scatter plots and linear fit coefficients using (a) LSQwAP and BT bias spectrum (b) LSQ and BT bias spectrum (c) LSQwAP and NN bias spectrum (d) LSQ and NN bias spectrum. 140
5.2 Scatter plots and linear fit coefficients using (a) LSQwAP and no bias spectrum (b) LSQ and no bias spectrum (c) Version 1 CO Retrieval. . 142
5.3 RMS and bias calculations for the 28 days determined to be cloud-free for LSQ on the 2, 3 and 5 layer retrieval grid. True composite CO profiles are mapped to the retrieval grid representation through relation $z = Wx$ described in Section 4.1. All results presented here use the LSQ retrieval equation, *a priori* first guess, and the BT bias spectrum. The retrieval grids used in each figure are (a) and (b) 2 layer, (c) and (d) 3 layer, and (e) and (f) 5 layer. 144
5.4 RMS and bias calculations for the 28 days determined to be cloud-free for LSQ on the 2,3 and 5 layer retrieval grid. True composite CO profiles are mapped to the retrieval grid representation through relation $z = Wx$ described in Section 4.1. All results presented here use the LSQwAP retrieval equation, *a priori* first guess and the BT bias spectrum. The retrieval grid used in each figure is (a) and (b) 2 Layer, (c) and (d) 3 Layer, and (e) and (f) 5 layer. 148
5.5 (a) CO retrieval on the merged profile grid (*ppbv*) using a 5 layer LSQ retrieval equation and the NN bias spectrum for 20070126 (b) Averaging kernel for the 5 layer retrieval grid using LSQ and the NN bias spectrum for 20070126. (c) CO retrieval on the merged profile grid (*ppbv*) using a 5 layer LSQwAP retrieval equation and the NN bias spectrum for 20070126. (d) Averaging kernel for the 5 layer retrieval grid using LSQwAP and the NN bias spectrum for 20070126. 151
5.6 CO retrieval on the 5 layer retrieval grid using the LSQwAP retrieval equation and the NN bias spectrum for 20070126. The first guess profile is the *a priori* profile. 153

6.1 (a) Retrieval using the LSQwAP retrieval equation with the NN bias spectrum, and AIRSv5 first guess. (b) Retrieval using the LSQwAP retrieval equation with the NN bias spectrum, and the *a priori* profile used as the first guess. Both retrieval results take the RTP CO profiles and convert them to merged profiles. 158
6.2 (a) Retrieval using the LSQ retrieval equation with the NN bias spectrum, and AIRSv5 first guess.(b) Retrieval using the LSQ retrieval equation with the NN bias spectrum, and the *a priori* profile used as the first guess. Both retrieval results take the RTP CO profiles and convert them to merged profiles. 160
6.3 RMS error calculations for LSQwAP retrieval equation on the retrieval grid. (a) AIRS first guess and NN bias spectrum (b) *a priori* and NN bias spectrum(c) AIRS first guess and BT bias spectrum (d) AIRS first guess, NN bias spectrum, and using all channels from 2107-2189 cm^{-1}. 163

6.4 (a) Total column CO scatter plot and linear regression coefficients for retrieval vs *in situ* using LSQwAP, AIRS first guess, and bias spectrum for days listed in Table 6.1. (b) Total column CO scatter plot and linear regression coefficients for retrieval vs true composite CO using LSQwAP, *a priori*, and bias spectrum for days listed in Table 5.1. 165

A.1 5 layer retrieval using the NN bias spectruum and the LSQwAP retrieval equation on the merged profile grid measured in *ppbv*. (a) and (c) represent the retrieval days using AIRSv5 CO as the first guess profile. (b) and (d) represent the retrieval results using an *a priori* first guess. 171

A.2 5 layer retrieval using the NN bias spectruum and the LSQwAP retrieval equation on the merged profile grid measured in *ppbv*. (a) and (c) represent the retrieval days using AIRSv5 CO as the first guess profile. (b) and (d) represent the retrieval results using an *a priori* first guess. 172

A.3 5 layer retrieval using the NN bias spectruum and the LSQwAP retrieval equation on the merged profile grid measured in *ppbv*. (a) and (c) represent the retrieval days using AIRSv5 CO as the first guess profile. (b) and (d) represent the retrieval results using an *a priori* first guess. 173

A.4 5 layer retrieval using the NN bias spectruum and the LSQwAP retrieval equation on the merged profile grid measured in *ppbv*. (a) and (c) represent the retrieval days using AIRSv5 CO as the first guess profile. (b) and (d) represent the retrieval results using an *a priori* first guess. 174

A.5 5 layer retrieval using the NN bias spectruum and the LSQwAP retrieval equation on the merged profile grid measured in *ppbv*. (a) and (c) represent the retrieval days using AIRSv5 CO as the first guess profile. (b) and (d) represent the retrieval results using an *a priori* first guess. 175

List of Abbreviations

CO	Carbon Monoxide
AERI	Atmospheric Emitted Radiance Interferometer
kCARTA	kCompressed Radiative Transfer Algorithm
AIRS	Atmospheric Infrared Sounder
ARM	Atmospheric Radiation Measurement program
SGP	Southern Great Plains
SSEC	Space Science and Engineering Center
HeNe	Helium Neon
FTIR	Fourier Transfer Interferometer
EPA	Environmental Protection Agency
RMS	Route Mean Square
FI	Factor Indicator
PCA	Principal Component Analysis
DACOM	Differential Absorption CO Measurement
INTEX	Intercontinental Chemical Transport Experiment
FOV	Field of View
TPW	Total Precipitable Water
HITRAN	HIgh resolution TRaNsmission molecular absorption database
pdf	Probability Distribution Function
BT	Brightness Temperature
NN	Neural Network
pdf	Probability Distribution Function
DOF	Degrees of Freedom
AK	Averaging Kernel
LSQ	Least Square
LSQwAP	Least Square with A priori
TES	Tropospheric Emission Spectrometer
MOPITT	Measurements of Pollution in the Troposphere
SAAC	Stand Alone AERI Co retrieval
PWV	Precipitable Water Vapor
RUC	Rapid Update Cycle
CAPE	Convective Available Potential Energy
CIN	Convective Inhibition
FFT	Fast Fourier Transform
IFFT	Inverse Fast Fourier Transform
RTE	Radiative Transfer Equation
LBLRTM	Line by Line Radiative Transfer Model
WVMR	Water Vapor Mixing Ratio
CKD	Clough-Kneizys-Davies
MTCKD	Mlawer-Tobin Clough-Kneizys-Davies
MNL	Moderately non-linear
NL	Nearly Linear
MWR	Microwave Radiometer
VMR	Volume Mixing Ratio

Chapter 1

Introduction and Outline

1.1 Introduction

Carbon monoxide (CO) influences both climate change and surface air quality. CO is the primary sink for the hydroxyl radical OH, and indirectly affects climate change because methane and other greenhouse gases are removed from the atmosphere through reactions with OH [19]. Carbon monoxide influences surface air quality through its role as a precursor in the tropospheric ozone chemistry cycle [12, 54]. The current ability to forecast the CO budget has been shown to be inadequate in studies [71, 19] in which chemistry transport models (CTM) showed large biases compared to National Oceanic and Atmospheric Administration/Ground Measuring Division (NOAA/GMD) stations measuring CO at the surface [61]. A primary source of uncertainty in the modeled CO budget comes from CTM assimilating CO measurements from satellites that have shown observational error of 10-30%, where the highest uncertainty is near pollution outflow regions [32]. Satellites are ideal for measuring the well mixed CO distribution in the mid-troposphere, but do a poor job measuring lower tropospheric CO, which can have variability of 50-100% in a profile [37, 4, 17, 52].

This dissertation has two objectives:

1. Characterize all significant sources of error between measured spectra and

modeled spectra in the band commonly used for the remote sensing of carbon monoxide (2100 - 2200 cm^{-1}) from both satellite [42, 88, 47] and ground based sensors [48].

2. Present new remote sensing techniques that measure total column density and profile information (when combined with satellite retrievals) that improves upon a previous CO retrieval method [48, 28, 90].

By creating a retrieval algorithm that incorporates measurements from both ground based and satellite sensors, the retrieved boundary layer CO value is decoupled from the true value for free tropospheric CO. Thus, the uncertainty in the vertical sensitivity present in the previous CO retrieval method is eliminated.

A ground based Fourier Transform Infrared Radiometer (FTIR) is the primary instrument providing data; specifically, the Atmospheric Emitted Radiance Interferometer (AERI) is used to sample infrared radiation in a spectral region (2100 - 2200 cm^{-1}) sensitive to carbon monoxide [28]. Temperature and water vapor profiles are produced from different sections of AERI spectra [22, 53], allowing synthetic AERI measurements to be created from the k Compressed Atmospheric Radiative Transfer Algorithm (kCARTA) [13]. Retrieved CO columns are produced from measured AERI calibrated spectra every 8-10 minutes.

With calibrated AERI measurements at 8 minute resolution already existing back to 1995, the new remote sensing measurements provide a wealth of information about surface CO measurements including climatologies and diurnal cycles of CO. Moreover, when combined with satellite retrieved CO, this new CO measurement

accurately measures boundary layer CO and can be used to better constrain the CTM. The Atmospheric Radiation Measurement (ARM) program run by the Department of Energy (DOE) keeps data records of AERI measurements in the tropical western Pacific (TWP), North Slope of Alaska (NSA), and Southern Great Plains (SGP) [29]. Ten new E-AERIs are expected to come online in the near future also, providing many more observation locations [29].

Remote sensing techniques in this dissertation are developed and tested against CO profiles that are a composite of measurements, including a 60 meter tower [7], aircraft [60, 59], and version 5 CO profiles retrieved from the Atmospheric Infrared Sounder (AIRS) [47]. These measurements are compiled together and used to validate an earlier version of the CO retrieval (Version 1) [90].

1.2 Role in Tropospheric Ozone

Hemispheric asymmetry of tropospheric ozone first led to the idea that tropospheric ozone is not just the result of intrusions from stratospheric air [24]. The presence of ozone in the troposphere is a result of stratospheric intrusions and photochemical reactions involving CH4-CO-NO_x [11]. Carbon monoxide's role as a source or sink of ozone depends on the concentration of NO_x [33, 11, 36]

Ozone is removed in the troposphere photochemically:

$$O_3 + h\nu \rightarrow O_2 + O \tag{1.1}$$

, or through a reaction with nitric oxide:

$$NO + O_3 \rightarrow NO_2 + O_2 \tag{1.2}$$

Tropospheric ozone is produced through the oxidation of CO with the hydroxyl radical OH. The chemical cycle for the production of ozone is shown below (M is a non reacting body required in the equation):

$$OH + CO \rightarrow H + CO_2$$

$$H + O_2 \rightarrow HO_2 + M$$

$$HO_2 + NO \rightarrow NO_2 + OH$$

$$NO_2 + h\nu \rightarrow NO + O$$

$$O + O_2 + M \rightarrow O_3 + M$$

The net reaction of this cycle, shown in equation 1.3, demonstrates that one ozone molecule is produced from the oxidation of one CO molecule [36].

$$CO + 2O_2 \rightarrow CO_2 + O_3 \tag{1.3}$$

It has been estimated that the concentration of nitric oxide must be at least 10 parts per trillion (ppt) in order to overcome the loss of nitric oxide through equation 1.2 [11]. When an adequate amount of nitric oxide is present the oxidation of CO is estimated to produce 2.5x10^{11} molecules cm^{-2} s^{-1} of ozone. The ozone yield from oxidation of both CO and methane is estimated to be 8x10^{11} molecules cm^{-2} s^{-1} [36].

1.3 Previous CO Retrieval Studies

Previous remote sensing studies of CO have been done using an AERI [48, 28, 90] and an FTIR measuring solar absorption [15, 91, 63]. Using an AERI, which measures infrared photons passively, allows for diurnal studies and night time measurements of CO, which are not possible with a sun-viewing FTIR [28]. A study comparing retrieved total tropospheric column density from an AERI, an FTIR, and a grating spectrometer showed agreement within 10% [48].

The previous AERI studies perturb a constant volume mixing ratio (VMR) for the entire troposphere to minimize spectral residuals [48, 28]. The algorithm takes spectra between 2135-2200 cm^{-1}, measured in brightness temperature, and utilizes a Fourier signal processing technique known as the Welch method [8, 20] to estimate the cross-spectral density of the CO signal [52]. The CO signal is defined as the observed spectrum from AERI minus a synthetic spectra produced from kCARTA. This Fourier technique takes advantage of the regularly spaced and nearly sinusoidal signal from the fundamental 1 - 0 vibration-rotation CO lines [51]. The final retrieved VMR is proportional to the amplitude of the sinusoid [52].

The single retrieved VMR represents a weighted average of the entire troposphere that is mostly sensitive to the boundary layer. In general, the retrieved VMR is 70% sensitive to the boundary layer CO and 30% sensitive to the rest of the troposphere [48]. As stated in [48], there is ambiguity as to whether the version 1 retrieval is better compared to boundary layer (≈0-2km) CO abundances or to total tropospheric columns [48]. A validation campaign using 96 *in situ* composite

true profiles was compared to version 1 retrieved CO in [90]. To overcome the ambiguity with the proper comparison for the version 1 CO retrieval, the *in situ* CO measurements were convolved with the averaging kernel (AK in equation 1.4) [66] of the retrieval to produce a *Convolved Truth* measurement [90] (FG is the first guess used in the CO retrieval). An averaging kernel defines relative weights of the true and *a priori* profile in a retrieved profile, and therefore accounts for the sensitivity of the retrieval to the true state [14].

$$Convolved\ Truth = FG + AK(Truth - FG) \tag{1.4}$$

The results of the validation from [90] indicate that version 1 AERI CO retrieval has a large systematic bias; specifically, version 1 retrievals from AERI consistently underestimate the CO abundance in the atmosphere. The validation results report a standard deviation of ± 12 ppbv and a bias of -16 ppbv for a RMS error of 20 ppbv. The RMS error corresponds to a percent error of 11 - 20%. This demonstrates that the 10% reported in [48] is the minimum expected error, and the theoretical estimation of 5% reported in [28] is not accounting for all error sources.

1.3.1 Previous Modeled Error Analysis

The first error analysis related to retrieving CO investigated three sources of error [49, 28]: Error due to measured spectra from AERI, error due to temperature profiles input to kCARTA, and error due to water vapor mixing ratio profiles input to kCARTA. A simulation study found that the effect from these sources on the VMR retrieved from AERI was 0.75, 1.5, and 2.5% respectively, for a total error of 5% [49,

28]. None of these error sources should produce a systematic bias, and considering the validation results shown in Figure 1.1, the theoretical error underestimates the real error.

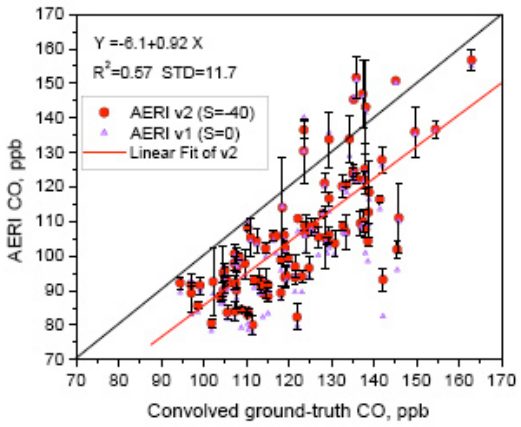

Figure 1.1: Version 1 AERI retrieved CO compared with convolved *in situ* measurements. This graph was taken from [90].

The validation study in [90] noted the radiance difference between synthetic spectra from kCARTA and AERI measurements, and attributed the radiance difference to systematic error in the water vapor profiles input to kCARTA and scattered solar photons from thin clouds. A result from [90] is shown in Figure 1.2(a) Radiance difference plotted as a function of precipitable water vapor (PWV), shown in Figures 1.2(a) and 1.2(b), are for two separate studies summarized in Table 1.1. Both figures show a quadratic dependence on PWV; however, the study in [82] states that the error is a result of the self broadening absorption coefficient, used to model the collisional effect of water, being 3-8% to strong in 900 cm^{-1} window region. Between the two studies [82, 90], 3 different water vapor profiles (AERI retrieved, radiosonde, Raman Lidar) were used as input to forward models and all displayed

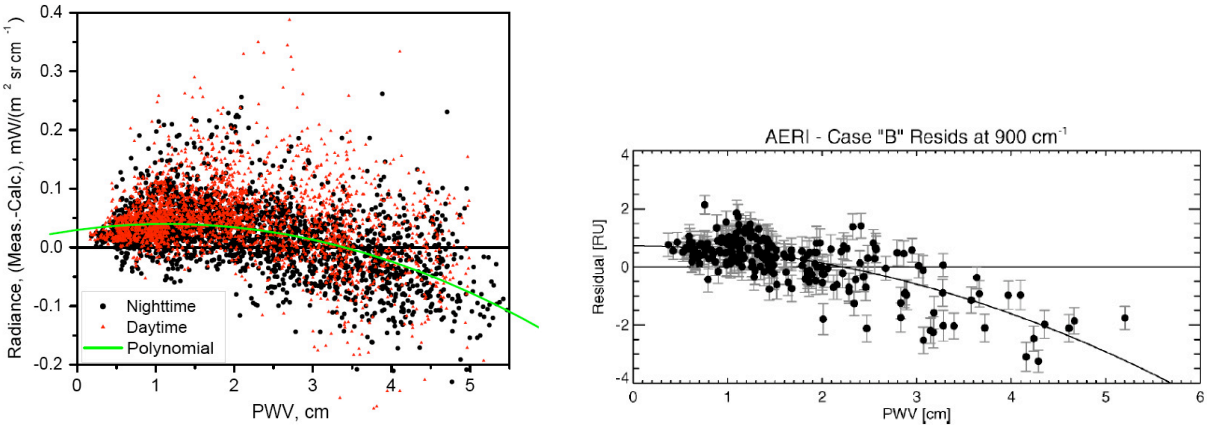

(a) Yurganov (b) Turner

Figure 1.2: (a) Average radiance difference in window channels 2142.7-2144.1 cm^{-1} and 2167.2-2168.7 cm^{-1} plotted as a function of PWV. Synthetic spectra was calculated using retrieved water vapor profiles from AERI as input to kCARTA. This plot was taken from [90]. (b) Average radiance difference in 900 cm^{-1} window channel. This was taken from [82], where Case B signifies that the input to the line by line radiative transfer model (LBLRTM) were radiosondes scaled by PWV from an MWR. Note the functional similarity among the two graphs despite using different water vapor input profiles and forward models used to calculate the synthetic spectra.

the same quadratic error as a function of PWV. This suggests that errors in the water vapor profiles are not the main contributor to error in the CO band. Aerosol optical thickness (AOT) and *in situ* surface aerosol measurements showed no correlation with radiance difference in this spectral region as well. Considering the similarity between Figures 1.2(a) and 1.2(b), the radiance difference is most likely due to self broadening errors and accounts for the bias shown in Figure 1.1.

Study	Forward Model	Input WVMR	Spectral Region
Yurganov [90]	kCARTA	AERI Retrievals	Window around 2140 and 2160 cm^{-1}
Turner [82]	LBLRTM	Radiosonde	Window at 900 cm^{-1}

Table 1.1: Two studies examining radiance difference of window channels. Input WVMR specifies what type of water vapor mixing ratio (WVMR) profile is used in the study.

1.4 New Techniques and Major Results

1.4.1 New Error Analysis

This is the first study that presents the estimated radiance error in the CO band (2100-2200 cm^{-1}) from synthetic spectra produced by kCARTA due to errors in the AERI retrieved temperature and water vapor input profiles (a previous study presented an estimate on the percent error in the version 1 CO retrieval due to error in the input profile [28]). Moreover, this is the first work that investigates the

significance of modeling errors in forward modeling spectra in the CO band. One major result from this work, as discussed more fully in Chapter 3, is that the error in synthetic spectra produced by kCARTA due to forward modeling errors is a full order of magnitude larger than error from the input profiles and is likely systematic, as was shown for a different spectral region (900 cm^{-1}) [82]. Instrumental error in AERI was estimated using the principal component analysis technique [81], and was found to be two orders of magnitude smaller than modeling errors.

The error analysis in this work provides some conclusions about the retrieval bias found in the version 1 retrieval [90]. By using a new cloud flagging technique [80], this work shows that many days (28 out of 56 for 2007 - 2008) used to validate the version 1 CO retrieval contained clouds that were not flagged by an earlier cloud flag technique [28]. The spectral contrast in the CO band is reduced when clouds are present in the AERI field of view, thereby reducing retrieved CO for the version 1 retrieval. Direct comparison of AERI and kCARTA spectra for cloud free days showed that kCARTA is biased low. The magnitude of the difference between kCARTA and AERI shows a temporal variation quite similar to the seasonal cycle of PWV measured from an microwave radiometer (MWR). This seasonal cycle persisted even after scaling water vapor profiles from AERI, used as inputs to kCARTA, with the PWV measurement from the MWR. This provides further proof that absorption coefficients used to model water (water, self broadening, foreign broadening) are the dominant error term for this region and have a systematic bias. The full effect of this seasonal bias is not tested, but likely contributes to the retrieval bias shown in Figure 1.1 as well.

1.4.2 New Retrieval Techniques

Two retrieval techniques are created, which use the estimated error statistics from part one of this dissertation to create an error covariance matrix for use in a constrained nonlinear least squares retrieval technique [67]. This new remote sensing technique is called the Stand-Alone AERI CO retrieval, or SAAC for short.

The first new measurement is a single layer CO column density measurement whose averaging kernel is very similar to the version 1 CO retrieval [48]. When the bias was removed from kCARTA spectra, total column density CO matched up with *in situ*. When the bias was not removed from kCARTA spectra, retrieved CO from this technique exhibited a similar systematic bias as was found in the study by Yurganov [90].

A 5 layer retrieval is created that remotely measures CO VMR profiles. Results confirm that when using an AERI without other information, profiling is not possible; however, it is shown that using the AIRSv5 CO retrieval [47] as a first guess created a SAAC+AIRS retrieval that retrieves boundary layer CO to better than 10 percent while preserving the free tropospheric retrieval from AIRS. Profiles from this combined retrieval scheme are more accurate than retrievals from SAAC or AIRSv5 working independently. Further, this retrieval method effectively decouples the boundary layer CO value from the free tropospheric value. This presents an improvement over the version 1 CO retrieval, where it is not clear what the retrieved value really represents.

1.5 Outline

In Chapter 2, an overview of the instrumentation and platforms used in this study is presented. In a study by [90], an assortment of platforms, including AIRS retrieved CO, *in situ* gas measurements from aircraft and a tower are used in order to construct the best estimate of a true CO profile. The primary instrument used is the AERI-01 instrument located at the SGP research site in Oklahoma. Data obtained from the AERI-01 instrument is the measurement to be linearly mapped to an estimated CO profile. Next, details about the Atmospheric Infrared Sounder are presented. AIRS is an instrument aboard the Aqua satellite which provides daily CO profiles globally [46]. Next, the near surface *in situ* trace gas measurements are detailed. Small aircraft were used to sample air at standard heights from 450 to 4500 meters above sea level (a.s.l.) [60, 59]. Below this, CO data was sampled by gas samplers on a 60 meter tower [7]. Lastly, information on the MWR used to constrain water vapor profiles used in kCARTA to generate synthetic spectra is presented. An illustration demonstrating all the different measurement platforms used in this project can be seen in Figure 1.3.

Chapter 2 presents the aspects of radiative transfer theory, error theory, and inverse theory used in this dissertation. The radiative transfer equation describing the physics for an up-looking instrument measuring infrared energy from clear sky conditions is presented. Error theory describes how measurement error is understood and uncertainty is quantified . The inverse methods describe why the inverse problem is ill-posed, and constraints are needed. In developing the retrieval

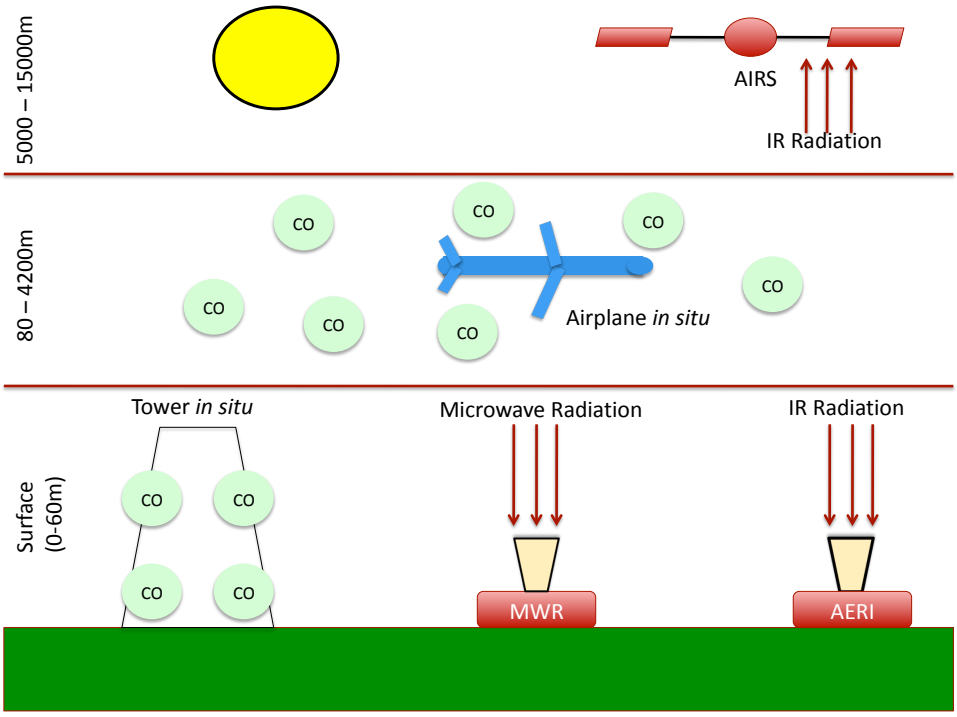

Figure 1.3: A schematic showing the setup of all the measurements used in the study.

solutions, information content and the effect of the first guess is also described.

In Chapter 3, an overview of all the modeling efforts taken to simulate a measurement from the AERI-01 instrument is presented. In this section, an examination of which atmospheric variables make strong contributions to the radiant energy, in the part of the spectrum where CO has strong emission lines, is presented. It is determined that the important variables are temperature, water, and carbon monoxide. Investigations are done that examine how the choice of a radiative transfer grid, water continuum model, and kCARTA version affect the simulated AERI measurements. Finally, tests are conducted that examine the bias between the best forward model and AERI measurements.

Chapter 4 is an in depth discussion of the two SAAC retrieval algorithms, where the first retrieval technique is an iterative constrained least square approach [34] constrained to the previous iteration. The second is similar to the first; however, it is constrained to the first guess [67]. Critical to these inverse methods is the estimation of the covariance matrices used in the retrieval scheme. Care is taken to make the best statistical estimation of the error and *a priori* covariance matrices. The retrieval grids and *a priori* profiles are built on 1,2, 3 and 5 layers. The *a priori* profile is taken as the mean state of all 56 profiles in the true composite CO data set.

Chapter 5 presents the results of both retrieval algorithms for retrieval grids of 1,2,3 and 5 layers using the *a priori* as the first guess. Single layer measurements are total columns and are shown to have high correlation to the true total column measurements. Also shown are comparisons to the version 1 CO retrieval.

Chapter 6 presents results using AIRSv5 CO retrievals as a first guess for the retrieval and demonstrates how CO profiles using AIRSv5 CO is superior to using an *a priori* profile for the first guess. The chapter concludes with directions for future work and conclusions.

Chapter 2

Measurements, Models, and Theory

2.1 Tower

In situ CO measurements from the 60m tower at the SGP site are acquired by the Lawrence Berkeley National Laboratory (LBNL) using a non-dispersive infrared gas correlation instrument (ThermoScientific TE-48C) [7]. This instrument uses additional pressure control, frequent zero correction and multi-point calibrations to provide precision and accuracy near 5 *ppbv* when compared with NOAA network flask measurements [62]. These measurements provide the surface measurements of CO for use in the construction of the true CO profiles.

2.2 Airplanes Profiles

In situ CO profiles at the SGP site are measured weekly by the NOAA Earth System Resources Laboratory (ESRL) using an automated programmable flask package operated on a small aircraft. Flasks are filled by air at standard heights above sea level (a.s.l.): 450, 610, 914, 1220, 1520, 1830, 2440, 3050, 3660, 4570m a.s.l. (the surface altitude at SGP is 374m a.s.l.). Following each flight, the flasks are returned to NOAA/ESRL for analysis via gas chromatography to determine CO mixing ratios [59]. Measurements are reported in units of nanomol/mo

(10^{-9} molCO per mol of dry air) relative to the WMO CO scale [60]. Reliability of the measurements, based on repeated analysis of air from a high-pressure cylinder, is $\pm$ 1 *ppbv* for measurements near 50 *ppbv* and $\pm$ 2 *ppbv* for measurements near 200 *ppbv* [59]. From 2007-2008, there were 57 occurrences when aircraft measuring CO were collocated in time and space with AERI measurements and tower data [90].

2.3 AIRS

The AIRS instrument is a high spectral resolution ($\frac{\nu}{\Delta\nu} \approx 1200$) grating spectrometer [74]. AIRS has been providing well calibrated spectral radiances since its launch date of May 4, 2002 aboard the Aqua satellite and measures two bands with a total coverage from 660 to 2655 cm^{-1}. Launched in a 705 km polar sun-synchronous orbit, it was designed to retrieve day and night profiles of temperature and moisture with high vertical resolution [47]. Also aboard the Aqua satellite are the Advanced Microwave Sounding Unit A (AMSU-A) and the Humidity Sounder for Brazil (HSB). Both the AIRS and the HSB have a footprint of 13 km at nadir. A 3 x 3 array of AIRS and HSB footprints are contained within one AMSU-A footprint [74]. By combining these instruments together AIRS can retrieve CO in scenes that are up to 80% cloudy [74, 41, 75].

AIRS utilizes 36 spectral channels from 2189.49 to 2221.12 cm^{-1} to retrieve CO. Above 5 km, AIRSv5 CO is used to construct the true composite CO profiles. The level 5 CO product has been validated extensively by the Differential Absorption CO Measurement (DACOM) instrument flown aboard NASA's DC-8 aircraft.

These flights were flown during two measurement campaigns by NASA known as the Intercontinental Chemical Transport Experiment (INTEX -A and INTEX -B). Results from the extensive validation efforts of [47] are shown in Figures 2.1(b) and 2.1(a). The estimated error from AIRS above 5km is expected to range from 14 to 21%.

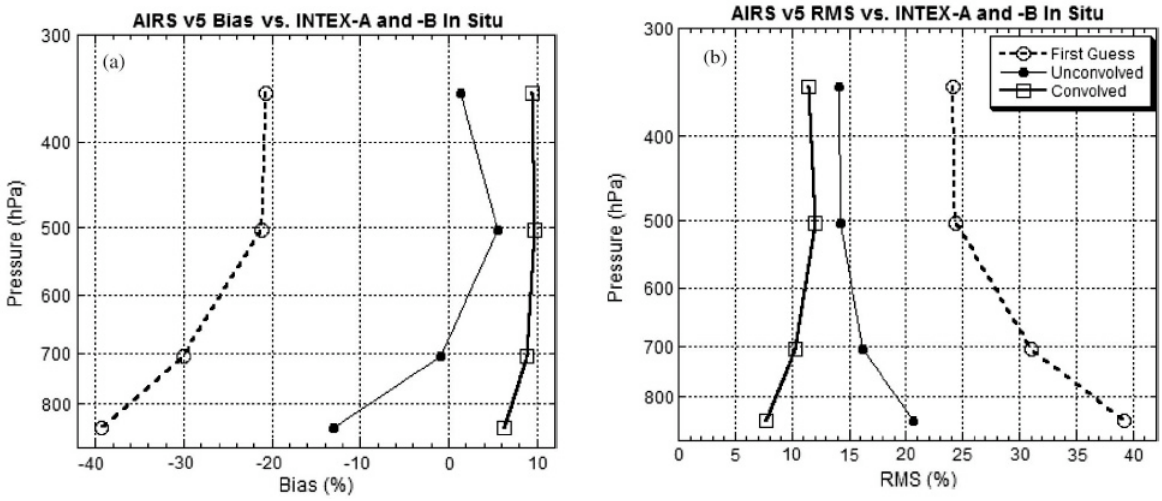

(a) (b)

Figure 2.1: (a) AIRSv5 CO bias estimates defined as AIRS - Truth. (b) AIRSv5 CO RMS estimates. Both figures were taken from [47]

It must be understood that the true profiles used in this study contain error from each source (tower, aircraft, AIRS) and the inclusion of the error from each source should be included into kCARTA studies. The true AIRS error is the unconvolved error estimation, and its effect on the spectra must be analyzed. Further, the AIRS retrieved CO is used as the true profile above 5 km and the unconvolved error is 14-21%, as seen in Figure 2.1(b). Because the instrument and retrieval are highly sensitive to the first 2-3 km, a 14% error in the true profile, above 5 km,

has limited effect on the retrieval. Therefore, the AIRS CO retrieval can be used as truth above 5 km [90].

2.4 Radiative Transfer

A forward model (e.g. kCARTA) is used to simulate what an instrument would measure. To understand the relationship CO has with measured spectra the radiative transfer equation (RTE) must be analyzed. First, a number of assumptions about the nature of the AERI retrieval setup simplifies the radiative transfer equation.

1. The AERI instrument field of view (FOV) is very small and the beam above the instrument contributing to the measurement will be homogeneous. This means a plane parallel atmosphere can be assumed.

2. All AERI measurements occur under clear sky conditions, therefore cloud effects or scattering from clouds are not included into the RTE.

3. All scattering effects are ignored because AERI measurements occur in portions of the infrared spectrum where scattering is negligible.

4. Any portion of the atmosphere that will contribute to the spectra measured at the ground is in local thermodynamic equilibrium.

Using these assumptions the radiative transfer equation in differential form is simplified [86].

$$\frac{dI(\nu,\theta)}{dz} = (-I(\nu,\theta) + B[\nu,T(z)])\sec\theta \sum_{i=1}^{N} k_i(\nu)\rho_i \tag{2.1}$$

where,

$B[\nu, T(z)]$ = *Planck blackbody function at frequency ν and at Temperature T(z)*

$I(\nu, \theta)$ = *radiance at frequency ν and in the direction θ from local vertical*

$k_i(\nu)$ = *absorption coefficient of an absorbing gas i*

$\rho_i(z)$ = *density of absorbing gas i*

N = *Total number of absorbing gases in the atmosphere*

The Planck function describes the spectral radiance for an ideal body emitting radiation at a certain temperature. Equation 2.2 displays how to calculate the Planck blackbody radiation for a given temperature. An effective temperature can be calculated by inverting Equation 2.2 and solving for the temperature. This effective temperature is commonly known as the brightness temperature. Figure 2.2 displays an example of AERI spectra compared to blackbodies radiating energy with different temperatures.

$$B(\nu, T) = \frac{2hc^2}{exp[hc\nu/kT] - 1} \tag{2.2}$$

where,

h = *the Planck constant*

c = *the speed of light*

k = *the Stefan-Boltzman constant*

ν = *wavenumber*

T = *temperature in Kelvin*

A few more simplifications of the RTE can be made before writing down the integral version. Because AERI's FOV is directly vertical $\sec\theta \approx 1$. Next, the hydrostatic equation can transform height to pressure by $\rho dz = -\frac{dp}{qg}$, where q is

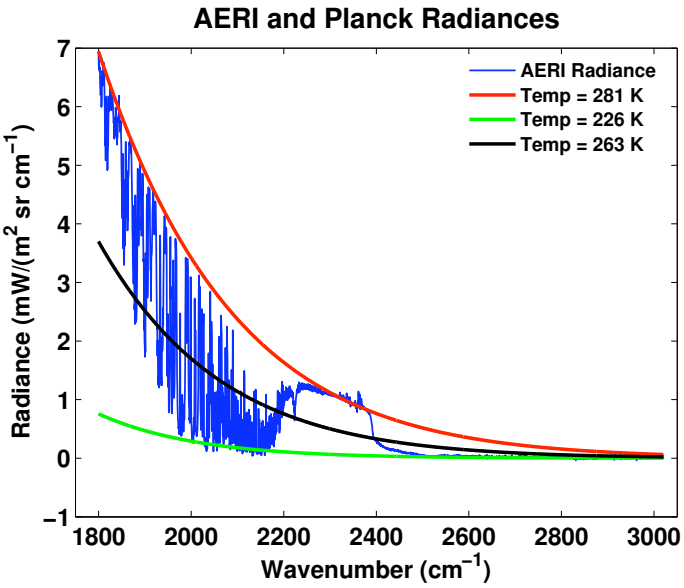

Figure 2.2: AERI radiance compared to blackbodies emitting radiance with their temperatures in K listed in the label.

the mass mixing ratio of the absorbing gas and g is acceleration due to gravity. It becomes convenient here to define the fractional transmittance of a layer, T:

$$\tau(\nu, p) = \exp[\frac{-1}{g} \sum_{i=1}^{N} \int_{p}^{p_{surf}} k_i(\nu, p) q_i(p) dp] \tag{2.3}$$

Equation 2.3 describes how gases absorb radiation and how they effect measured spectra. For regions where k(ν,p) is not negligible, an increase in gas will decrease the transmission coefficient. Therefore, photons reaching an instrument are coming from regions closer than before the increase. For an up looking instrument, this means that photons are coming from warmer regions in the atmosphere and the measured energy will now be greater. The opposite is true for a satellite, an increase in gas amount means that photons reaching the instrument are emitted higher up in the atmosphere where regions are cooler and decrease the top of atmosphere (TOA) radiance. The summary of this is provided in Table 2.1.

Instrument Position	gas_i truth - guess	τ_{truth} - τ_{guess}	obs. - calcs.
Ground looking up	positive	negative	positive
Ground looking up	negative	positive	negative
Space looking down	positive	negative	negative
Space looking down	negative	positive	positive

Table 2.1: Expected values of observed minus simulated radiance calculations for a perturbation in a gas profile. Also shown is the change in transmittance. This is for tropospheric sounding only; in the stratosphere, each situation is reversed because the sign of the lapse rate changes.

Regions where *k(ν)* is very small are known as window regions. Here, the gases do not absorb or emit much radiation and photons can travel the entire length of the atmosphere. An uplooking instrument would measure photons from space and a satellite would measure photons traveling from the earth's surface.

By making the substitutions listed above it becomes possible to integrate and solve for the radiative transfer equation.

$$I(\nu, p_{surf}) = \epsilon(\nu)[B(\nu, T(p_{top})\tau(\nu, p_{top})] + \int_{p}^{p_{surf}} B(\nu, T(p)\frac{\partial\tau(\nu, p)}{\partial p}dp \qquad (2.4)$$

Equation 2.4 displays the integral version of the radiative transfer equation for an uplooking instrument [86] under the assumption of no clouds. The first term is not negligible but much smaller than the second term because $T(p_{top}) \approx 3\text{K}$. Equation 2.5 displays a simplified version of the RTE to better illustrate the role

transmission has in determining radiation at an instrument.

$$I(\nu, p_{surf}) = \int_{p}^{p_{surf}} B(\nu, T(p) \frac{\partial \tau(\nu, p)}{\partial p} dp \tag{2.5}$$

There are two factors in the integrand in Equation 2.5: the source term $B(\nu, T(p))$, which is the Planck radiative energy emitted at a certain level, and $\frac{\partial \tau(\nu, p)}{\partial p}$ is known as the weighting function or the kernel of the RTE. A weighting function describes which parts of the atmopshere contribute radiation to a corresponding portion of spectra (ν).

When the distribution of radiatively active gases for a spectral channel is well known, the weighting function can be precomputed and $B(\nu, T(p))$ can be determined. If the temperature profile is known or determined from other channels, then the weighting function can be determined for new channels. Figures 2.3(a) and 2.3(b) show simulated weighting functions for AERI and AIRS CO spectral retrieval bands respectively. These figures demonstrate that the upwelling radiation measured by AIRS is a result of broad weighting functions in the mid-troposphere, while downwelling radiation measured by AERI is primarily a result of more strongly peaked weighting functions in the boundary layer.

Equation 2.5 is a Fredholm equation of the first kind [84, Ch.1]. A generalized version of the the Fredholm equation is seen in Equation 2.6:

$$g(t) = \int_{a}^{b} K(t, s) f(s) ds \tag{2.6}$$

where,

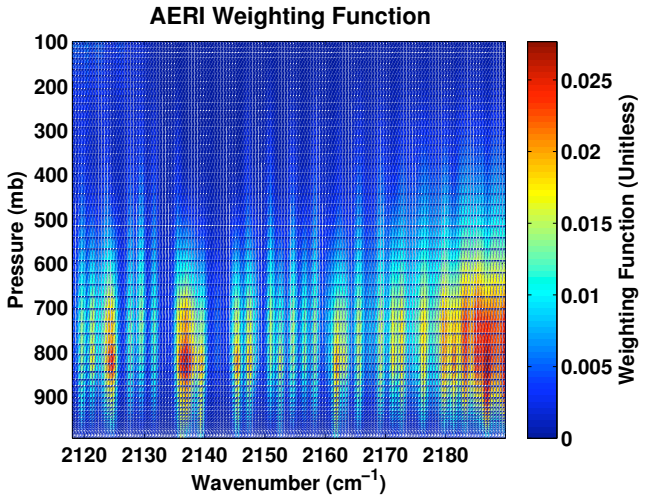

(a)

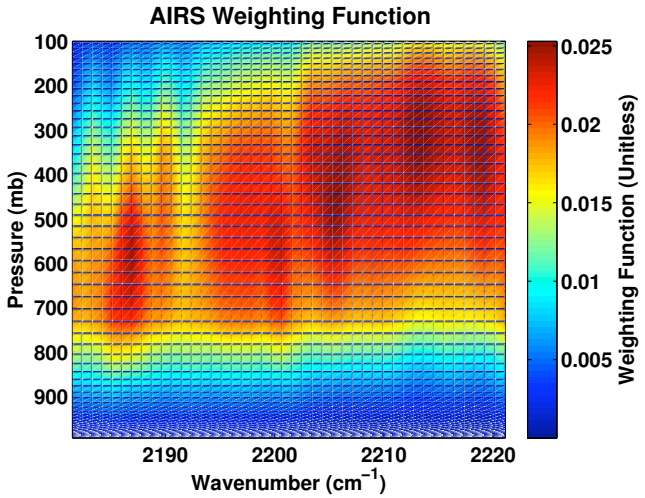

(b)

Figure 2.3: (a) A simulated AERI weighting function created from kCARTA simulation and apodized to AERI resolution. (b) A simulated AIRS weighting function from kCARTA apodized to AIRS resolution. Both figures cover the spectral range used in their respective CO retrievals [47].

$$
\begin{aligned}
K(t,s) &\equiv \textit{weighting function} \\
&= \frac{\partial \tau(\nu,p)}{\partial p} \textit{from equation } 2.5 \\
f(s) &= B(\nu, T(p))
\end{aligned}
$$

At first inspection Equation 2.6 may look simple enough to look up the inverse in a math formula book; however, the Fredholm equation does not allow for analytic inverse solutions. The form of Equation 2.6 is very similar to a Laplace transform and therefore it may be expected that a solution to the problem would be the same as inversion for the Laplace transform. The equation for the Laplace transform and its inversion can be seen in Equations 2.7 and 2.8 respectively. In Equation 2.7, $g(t)$ represents our measured radiance $I(\nu)$ from AERI. The integral in Equation 2.8 is taken along the path lying to the right of any singularities in $g(t)$; however, this path does not exist because our measurement is real valued and cannot be evaluated at imaginary points. Because the measurement $g(t)$ is real valued and measured at discrete locations, functional solutions to our problem cannot be used. This is why the radiative transfer equation must be linearized about a base point and solutions can be found using linear mapping methods.

$$
g(t) = \int_0^\infty e^{-ts} f(s) ds \tag{2.7}
$$

$$
2\pi i f(x) = \int_{\alpha - i\infty}^{\alpha + i\infty} e^{ts} g(t) dt \tag{2.8}
$$

2.5 Forward Model

A forward model is required in all retrieval methods to simulate what an instrument would measure based on a model atmosphere. Success of any retrieval scheme is limited by the accuracy with which the forward model can represent measurements from any instrument. kCARTA is used to take atmospheric profiles and simulate measurements from AERI.

2.5.1 kCARTA

kCARTA is the radiative transfer code which uses profiles of temperature and atmospheric constituents to produce synthetic spectra [13]. kCARTA is a lookup table that is based on absorption line parameters determined from the HIgh resolution TRaNsmission molecular absorption database (HITRAN) [69, 68]. kCARTA can output gas optical depths, transmittances, Jacobians, and radiances at .0025 cm^{-1} resolution for uplooking and downlooking instruments [13]. The high spectral resolution of synthetic spectra from kCARTA allows it to easily be convolved to AERI's spectral resolution of approximately .5 cm^{-1}.

kCARTA has been used previously to simulate measured radiances from AERI for studies that remotely sense trace gases [28, 34, 90] . The high spectral resolution of kCARTA and its previous use in trace gases retrievals make it a good choice to use as a forward model for this project. Two versions of kCARTA exist: (1) Version 114 which is based on the HITRAN 2004 molecular spectroscopic data base [69] (2) Version 115 which is based on the HITRAN 2008 molecular spectrospcopic data

base [68]. Synthetic spectra modeled by both versions is compared to measured spectra from AERI. Version 115 was used to model spectra for the use in retrievals.

2.5.2 Carbon Monoxide Input Profiles

Carbon monoxide profile input to kCARTA is defined on layered grids where each layer has its own average column density ($\frac{number\ of\ molecules}{cm^2}$). The true composite CO profiles from [90] are 12 - 15 point profiles defined in parts of CO per billion parts of dry air (*ppbv*). True composite CO profiles encompass measurements from tower, aircraft, and AIRS. The bottom CO measurement is on the 60 meter tower (usually between 10 and 20 mb less than surface pressure) and the top of the AIRSv5 CO profile (around 150-200mb).

Converting a profile defined by volume mixing ratio (VMR) to a profile defined by layers of average column density is done by an algorithm known as KLAYERS. For CO this program takes CO profiles defined in parts per million by volume (ppmv) defined on a 101 level grid and outputs a 100 layered grid of column densitites.

The input profiles from [90] are not defined down to the surface or up to the top of the atmosphere, nor are they defined on a fine enough grid for input to KLAYERS. The process of converting CO profiles from 10-15 points defined by a VMR to a 101 VMR point capable of being input to KLAYERS is described below:

1. The input profile is linearly interpolated by log pressure, from the input grid to the finer grid used in KLAYERS. The fine grid layers that cover the input CO pressure layers are used for the interpolation.

2. The lowest CO profile measurement is on the 60 meter tower at the SGP site. CO profiles were extrapolated linearly down to the surface on a finer grid. The surface pressure is defined as the first pressure listed in the temperature and water vapor retrievals from AERI.

3. The top of the input profile is linearly extrapolated, and then is forced to relax back to a reference profile. There are characteristic profiles built for mid latitude summer, mid latitude winter, and US standard. This is represented in Figure 2.4(b). The large values near the top of atmosphere (TOA) occur due to the low density of air.

Figure 2.4(a) displays two CO profiles used as input to KLAYERS. The first guess CO is *a priori* and represents the 56 profiles from [90] interpolated to a common grid and averaged together. The *a priori* measurement is one of the first guess profiles used in SAAC. The true CO profile in Figure 2.4(a) is one of the true composite CO profiles from [90].

Figure 2.4(b) displays the same true CO profile from Figure 2.4(a) after it has been processed to the 101 level grid and converted to *ppmv*. The results of putting this profile and others into KLAYERS is shown in Figure 2.5.

A short summary of the different representations of carbon monoxide used in this dissertation are given below:

- **True composite profiles:** Provided by [90], These are the profiles made up of 10-15 CO measurements taken from the three different platforms (AIRS, tower, and aircraft). The CO measurements are VMR values measured in

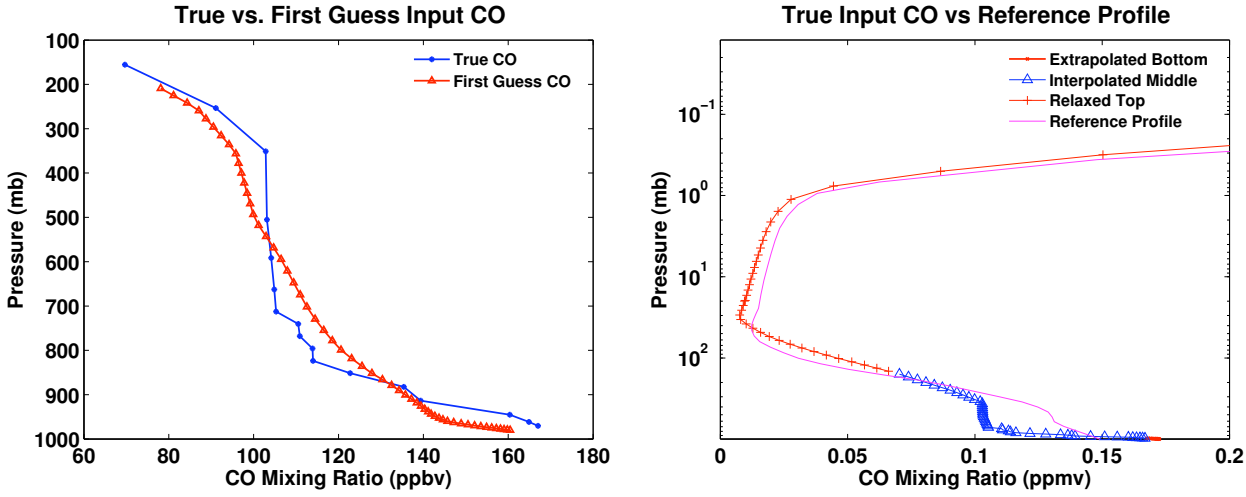

(a) (b)

Figure 2.4: (a) True CO profile (blue) is 20070126 profile from [90]. The First Guess CO profile is the *a priori* for the data set defined on a 101 level grid with the surface defined at 980 mb. (b) This figure displays how the input CO is merged from its grid of 10 - 15 levels to a 100 level grid that is read into KLAYERS.

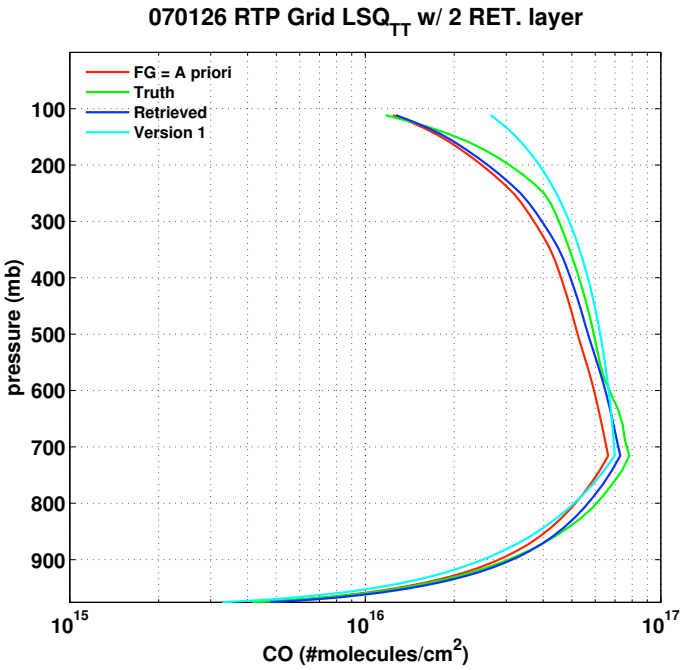

Figure 2.5: This figure shows profiles defined on the 100 layers capable of being read into kCARTA. Truth is the same profile from Figures 2.4(a) and 2.4(b) once it has been converted to column density by KLAYERS. The *a priori* is first guess profile from Figure 2.4(a)

ppbv.

- **Merged profiles:** Shown in Figure 2.4(b), these are the profiles of CO that are ready to be input into the KLAYERS algorithm. The units for these profiles are *ppmv*. Constructing these profiles come from both the true measurement and a reference profile on a grid made up of 85 - 101 levels.

- **RTP Profiles:** CO profiles in this grid are average column density values for a given layer. The units are $\frac{molecules}{cm^2}$. If there are n CO values in the merged grid then there will be $n-1$ values for CO in the RTP profile.

2.5.3 Water Vapor Continuum Modeling

Because the physics of water is not completely understood, empirical fits must be used to approximate foreign and self broadening features of water [82]. The continuum is usually determined experimentally, as the difference between the absorption coefficient between measurement and a calculation based on a Voigt line shape [23]. As experimental methods are improving, the empirical fits are constantly being updated. The most popular versions of continuum models are the CKD (Clough-Kneizys-Davies) or MT_CKD (Mlawer-Tobin-Clough-Kneizys-Davies) which are named after their creators [55]. The newest continuum model, MT_CKD version 1 has new multipliers for self and foreign broadening in a window ranging from 600 to 1400 cm^{-1} [56, 82]. Continuum models CKD version 2.4 [10, 25, 77] and MT_CKD version 1.0 [82] are both used in kCARTA to create synthetic spectra which is compared to measured spectra from AERI.

2.5.4 kCARTA Grids

Important to a forward model's accuracy is how the atmosphere is divided up into layers. The grid layers closer to the observing instrument typically are divided into smaller layers to increase the accuracy of the synthetic spectra from kCARTA. Using smaller layers allows for a more accurate calculation of the change in transmittance with height that then create more accurate weighting functions.

Six radiative transfer grids have been developed for kCARTA to simulate measurements from the the AERI instrument [26]. Each grid is 101 levels with varying surface pressure, allowing for a conversion to a 100 layer profile. The surface pressures for each grid are listed in Table 2.2. In [34, 90] one standard grid was used to simulate AERI spectra with kCARTA. SGP has a surface pressure that ranges from 960 - 990 mb. This results in up to 15 layers not being used in the standard 1013 layering scheme. By using a kCARTA for a more accurate representation these variable grids were used. The grid with the lowest surface pressure while still being greater than the surface pressure of the instrument was used. This resulted in 6 -7 unused layers on the radiative transfer grid.

1033	1013	999
993	980	961

Table 2.2: Surface pressure in millibars (mb) for different grids developed for AERI.

Figure 2.4(b) displays how the input CO profiles are changed from true composite profiles to the merged profiles that then input to the algorithm known as

KLAYERS. KLAYERS converts profiles defined on levels by mixing ratios to layers where each layer has it's own average column density ($\frac{number\ of\ molecules}{cm^2}$) [26]. This profile representation allows kCARTA to easily calculate the transmission coefficients needed to compute the radiance.

2.6 AERI

Spectral data is taken from the AERI-01 instrument run by the ARM program at their SGP site [22]. AERI is an automated instrument measuring downwelling infrared radiance emitted from the atmosphere. It was developed by the Space Science and Engineering Center (SSEC) at the University of Wisconsin - Madison to make highly accurate radiance measurements in order to validate satellite measurements [31]. Figure 2.6 displays AERI's short-wave and long-wave channels along with portions of the spectra sensitive to H_2O, O_3, CO_2, and CO. The red and blue portions of the spectrum are used in temperature and water vapor retrievals respectively [72, 79, 22].

The interferometer used by the AERI is the commercially available MR-100 series by ABB/BOMEM. Exact details of the optics used in the bench design of the MR -100 may be found in [30]. The setup of the interferometer acts as a Michelson Interferometer, with two detectors each measuring different portions of the infrared spectrum. AERI's two detectors are cryogenically cooled, in a sandwich configuration measuring infrared radiation from 3.3-19 μm. A picture of the interferometer setup with the two detectors in a sandwich configuration is shown in Figure 2.7.

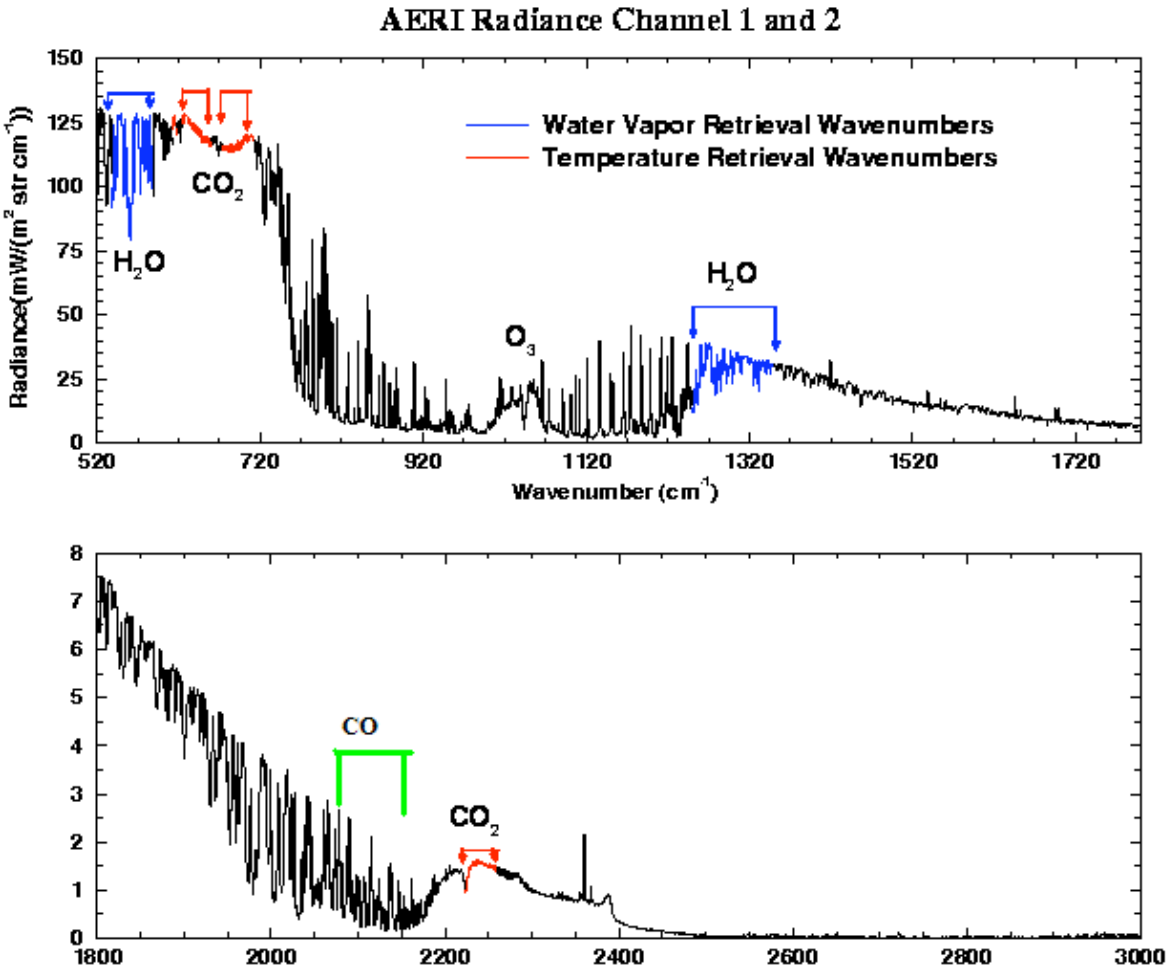

Figure 2.6: (top) AERI long-wave channel. Portions of the spectra sensitive to certain gases are labeled. Red portions of spectra are used in the temperature retrieval and blue portions are used in the water vapor retrieval [72, 22]. (bottom) The short-wave channel of AERI with the CO region highlighted as well.

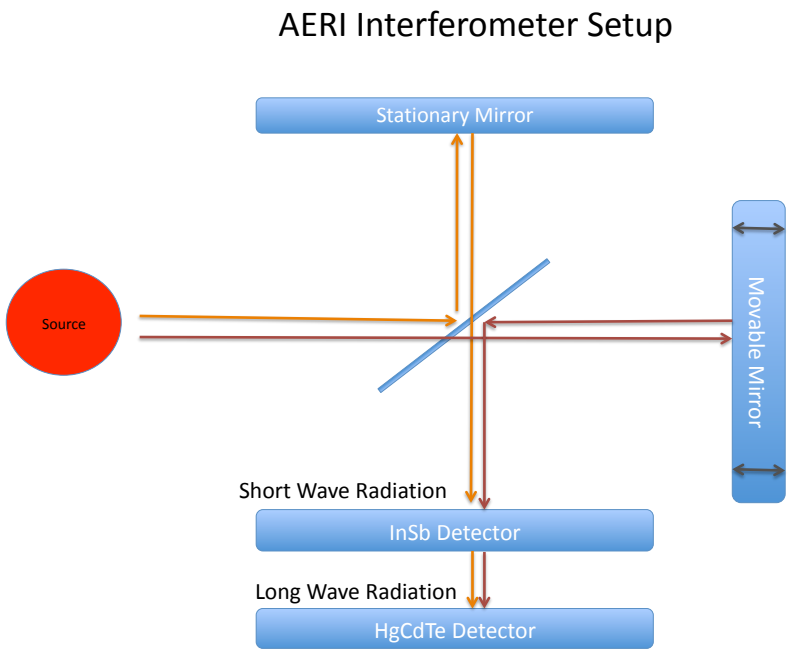

Figure 2.7: An illustration representing the setup of the AERI interferometer. Only the shortwave portion of the radiation is absorbed by the InSb detector, and allows the long-wave to pass through to the HgCdTe detector.

Using the maximum path length difference of the MR-100 (1.037 cm) to solve Equation 2.9 results in an AERI spectral point spacing of approximately .5 cm^{-1} [30]. The location of each spectral channel has an uncertainty of .01 cm^{-1} which is a direct result of the stability of the helium neon laser used to sample each point on the interferogram [30].

$$\Delta\nu = \frac{1}{2X} \tag{2.9}$$

where,

$\Delta\nu$ = *spectral domain frequency point spacing (cm^{-1})*

X = *maximum optical path difference (cm)*

AERI contains two blackbodies [30], one kept at 60°C and the other which can vary with ambient temperature. By using these highly accurate blackbodies and applying a correction for non-linearity in the detector, unapodized spectra is produced to 1% accuracy [31].

A normal AERI measurement cycle contains 3 minutes of sky viewing, 2 minutes at each blackbody, and approximately a minute of computations. Thus, a normal AERI view cycle produces a calibrated spectrum every 7 - 8 minutes resulting in 178 calibrated spectra per day. The AERI used in this study (AERI-01) has been running continuously at the ARM-SGP site since 1995 with only one stop in coverage from 2005 - 2006 due to a malfunctioning sterling cooler [80].

2.6.1 Apodizing AERI and kCARTA

An interferogram measured by AERI ($I(d)$) is the inverse Fourier transform of the incoming radiance ($I(\nu)$). The channel i radiance produced by AERI ($y_{AERI}(\nu_i)$) is calculated by taking the Fourier transform of the product of the inteferogram with an apodization function ($A(d)$) [85, Ch. 1]. Applying an apodization function to spectra is similar to applying a running mean, which introduces correlated error among channels [5, 34]. Without any numerical apodization techniques applied, the normal apodization function for an interferometer of path length L is a boxcar function (shown in the bottom of Figure 2.8(a)) where,

$$A_{boxcar}(d) = 1 \; for \; d \leq L$$

$$A_{boxcar}(d) = 0 \; for \; d \geq L$$

and d is optical path difference [85, Ch. 1].

Figure 2.8(b) shows that the *sinc* function ($\frac{sin(y)}{y}$) has alternating side lobes in between zeros located at $y = \pm n\pi$. The first four side lobes have heights of -21.7 %, 12.8 %, -9.1 %, and 7.1 % with respect to the central lobe [5]. In fact, only 45% of the area of SRF_{boxcar} comes from the central lobe [5]. This demonstrates that the contributions to the radiance at any given spectral channel have significant contributions from other channels far away in the band. This will cause spectral error to be correlated among channels, and the construction of an instrument error covariance matrix will have have many off diagonal terms. Moreover, it has been found that using boxcar functions to apodize kCARTA caused negative radiances in the modeled spectra [34]. Therefore the Norton-Beer (NB) apodization function is

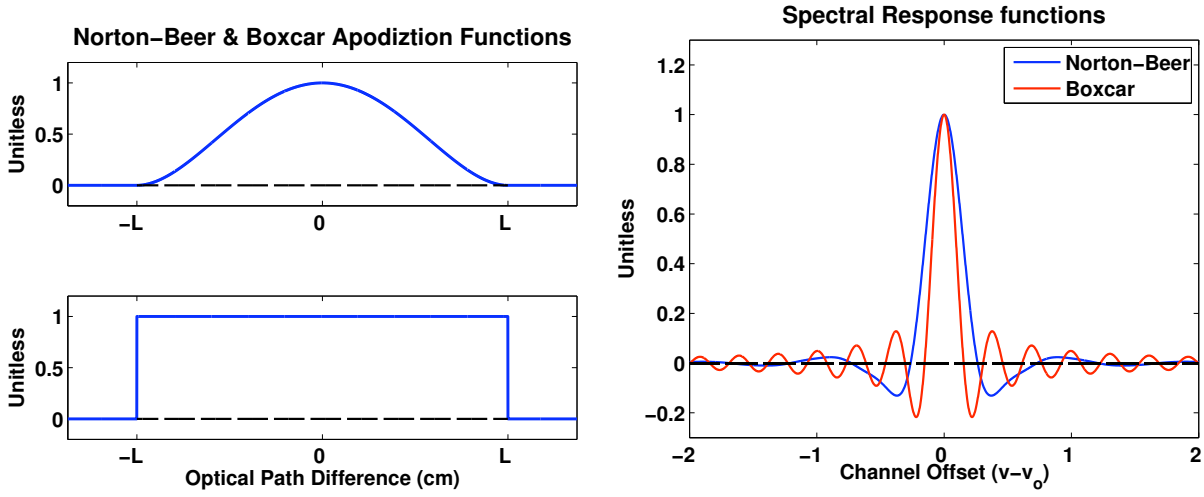

(a) (b)

Figure 2.8: (a) Top graph is Norton-Beer apodization function used in the convolution of the interferogram of kCARTA and AERI spectra. Bottom graph is a boxcar apodization function which is the natural apodization function of a non-infinite FTIR such as AERI. (b) Response functions in spectral space of the Norton-Beer (Blue) and Boxcar (Red) apodization functions.

used on both kCARTA and AERI spectra [57, 58]. The NB apodization function is ideal because it localizes noise correlation across channels and reduces ringing. This effect is shown in Figure 2.8(b) where the side lobes of the Norton-Beer SRF are comparatively smaller and the main lobe is comparatively wider to the *sinc* SRF. Figure

It has been shown that the apodization function can be written as a matrix where, $y_{apodized}(\nu) = My_{unapodized}(\nu)$ and for certain circumstances $y_{unapodized}(\nu) = M^{-1}y_{unapodized}(\nu)$ [5]. This indicates that the process of apodization is not removing information as transformations exist between apodized and unapodized spectra. In this same study noise reduction (NR) factors and channel noise correlation coefficients are calculated for many apodization functions. The noise reduction factor for NB (NR = 1.568738) and correlation coefficients are provided by [39] using the methods and results from [5]. Figure 2.9 shows that noise correlation from NB apodization is localized and drops to approximately zero after 3 terms.

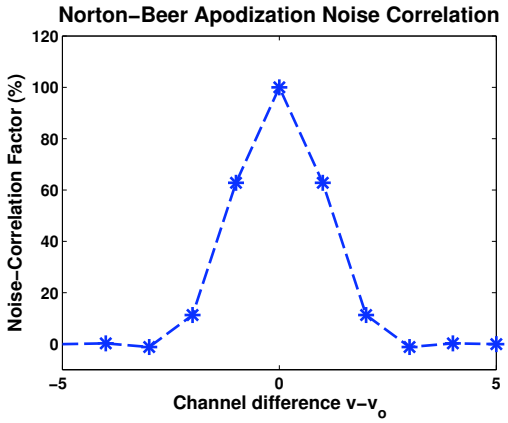

Figure 2.9: Noise Correlation coefficients measured as a function of distance away from band center (v_o) using units of wavenumber cm^{-1}.

Synthetic spectra from kCARTA must be convolved with the spectral response function (SRF) of the AERI instrument to properly compare spectra from kCARTA and AERI [34]. This creates synthetic spectra that has the same resolution and sensitivity as an AERI instrument.

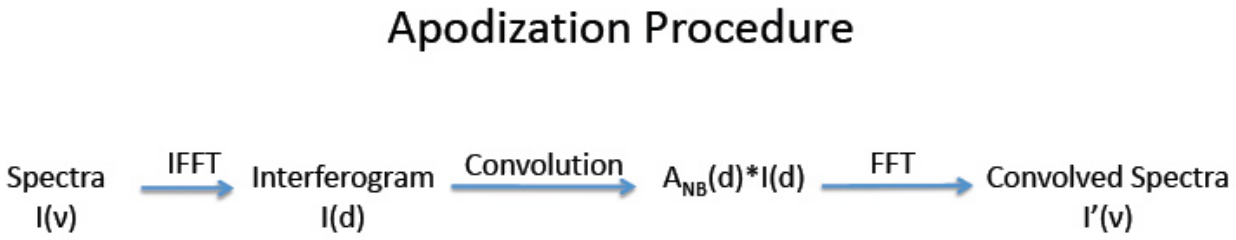

Figure 2.10: Process to apodize spectra from kCARTA or an AERI measurement. IFFT stands for an Inverse Fast Fourier Transform and FFT stands for a Fast Fourier Transform. A_{NB}(d) is the NB apodization function used to multiply the interferogram I(d), where d is path length. $I(\nu)$ represents spectra from either AERI or kCARTA.

The apodization process for kCARTA and AERI spectra is shown in Figure 2.10. Both spectra are Fourier transformed to an interferogram ($I(d)$) and multiplied by the NB apodization function (A_{NB}) from Figure 2.8(a). An FFT is performed on the inteferogram ($I(d)$) to produce apodized spectra ($I'(\nu)$).

2.6.2 AERI Meteorological Profiles and Other Uses

Temperature and water vapor retrievals have been developed which make use of the sensitivity in AERI spectra to meteorological profile information in the boundary layer (0-3km) [72, 22]. The AERI retrieval combines a statistical retrieval with the

version 2 hourly Rapid Update Cycle (RUC) numerical weather prediction model to create a first guess to the AERI physical retrieval. An optimal combination set of satellite information, numerical weather prediction, and radiosondes collocated in time with an AERI were used to develop the statistical profile [22]. The physical retrieval then adjusts the first 3 km of the hybrid first guess profiles for temperature and water vapor to fit the measured downwelling radiance [22]. Extensive validation efforts have shown the temperature retrieval has RMS differences of 1K [72, 22], approximately .005%. Water vapor retrievals have an absolute RMS differences of 5% [79]. Both temperature and water vapor retrievals were compared with Vaisala radiosondes scaled by MWR measurements to account for known dry biases [65]. Validation results for temperature and water are shown in Figure 2.11. These results are used in Chapter 3 to determine the error in modeled spectra resulting from errors in the temperature or water vapor profiles used as input to the model.

High resolution temporal monitoring of temperature and water vapor in the boundary layer allow AERI to nowcast stability indices of the atmosphere such as convective available potential energy (CAPE) and convective inhibition (CIN) [22]. One such study showed a rapid decrease in CIN just prior to thunderstorm development near Purcell, Oklahoma on May 3, 1999 [21]. This led to an outbreak of 63 tornados across Oklahoma including one F5 tornado. Another study increased the temporal resolution of AERI to 1 minute in order to measure the effect horizontal roll verticies had on AERI retrieved water vapor profiles [53]. To run with the increased temporal resolution (rapid sampling mode) Principal Component Analysis (PCA) is used to remove uncorrelated error that is introduced by decreasing the view times of

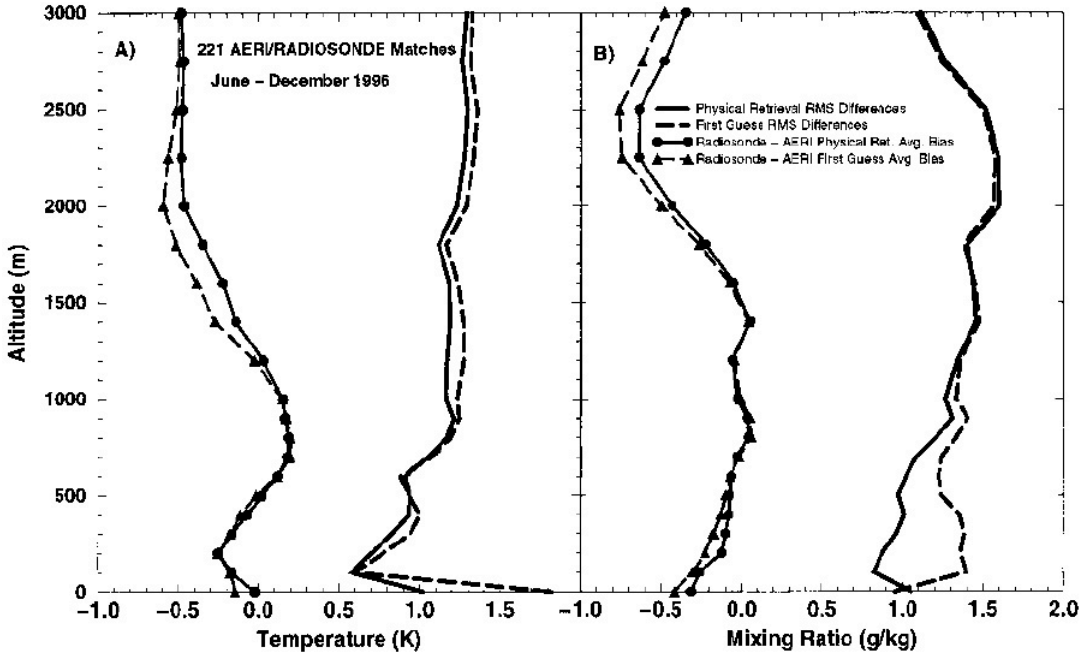

Figure 2.11: This figure, taken from [72], provides the validation results for the AERI temperature water vapor retrieval. The error statistics shown here are used in Chapter 3 to determine modeled spectral error due to errors in AERI retrieved temperature and water vapor profiles.

sky and blackbodies [81]. Other uses of AERI include providing accurate radiance measurements to improve radiative transfer algorithms [82] and for the use in the detection of clouds [80].

The term **Feltz** is used in this study when referencing the set of temperature and WVMR profiles from the ARM site at SGP. This is because the temperature and WVMR profiles provided by the ARM archive come in one data file named Feltz.

2.7 MWR

The Microwave Radiometer (MWR) located at the SGP site provides time series measurements of column integrated amounts of water vapor and liquid water. MWR is a 2 channel radiometer measuring microwave radiation at 23.8 and 31.4 GHz [45]. The MWR retrieval method combines radiance measurements with a statistical retrieval to retrieve integrated liquid water and water vapor [35]. According to [45], the accuracy of the MWR's precipitable water vapor (PWV) measurement is on the order of .1 cm.

It is well known that water lines dominate the fundamental CO band [76], and errors in the water vapor profiles used by kCARTA can cause a significant amount of error in relation to the size of the CO signal. A previous study showed that PWV measured from retrieved water vapor profiles from AERI can be different by up to 20-40 % when compared to MWR retrieved PWV [90]. To overcome this difference the retrieved water vapor profiles from AERI are scaled by MWR measurements as

shown in Equation 2.10.

$$Constrained\ WVMR(p) = \frac{PWV_{MWR}}{PWV_{AERI}} WVMR(p) \tag{2.10}$$

$WVMR(p)$ in the equation above is the retrieved WVMR profile from AERI, and it is multiplied by PWV measured by an MWR divided by PWV measured by an AERI.

The top part of Figure 2.12 demonstrates the difference between PWV measured from AERI and an MWR. Retrieved PWV from AERI (purple) experiences a sharp increase around 3 UTC while the MWR (grey) more smoothly changes; subsequently, the version 1 CO retrieval using constrained water vapor profiles shows a more natural and smooth change for the black time series in Figure 2.12.

2.8 Error Theory

Spectra measured by AERI or modeled by kCARTA each contain error when compared to the true spectra produced from the radiation coming from the atmosphere. As demonstrated in [67], any experimental error of a measurement or model represents the state of knowledge about the measurement. In this view point, any measurement y containing error has an expected value $\overline{y}$ described by a probability distribution function (*pdf*) $P(y)$. This all says that the probability that y is a value between y and $y+dy$ is $P(y)dy$. If the y and $P(y)$ are well known the expected value of y can be determined using Equation 2.11 and the variance of the measurement is

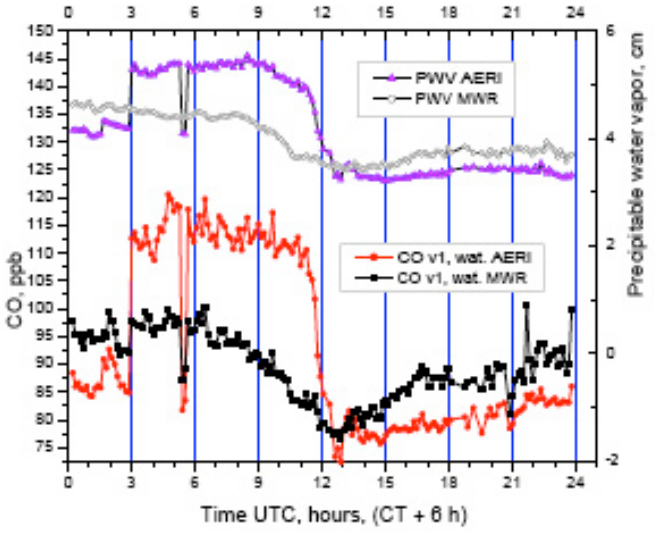

Figure 2.12: (a) Displays a time series for one day of retrieved PWV and retrieved CO. The top part of the graph is the measured PWV measured by AERI (purple) and MWR (grey) with its axis on the left. The bottom part of the graph is the version 1 CO retrieval with its axis on the left. The red time series represents the CO retrieval using water vapor profiles from AERI as input to kCARTA. The black time series represents the CO retrieval using constrained water vapor profiles as input to kCARTA. This figure is taken from [90]

calculated using Equation 2.12.

$$\overline{y} = \int yP(y)dy \tag{2.11}$$

$$\epsilon^2 = \int (y - \overline{y})^2 P(y)dy \tag{2.12}$$

The *pdf* of y demonstrates knowledge about the precision of y and is not a distribution function of repeated measurements; however in the absence of the distribution function, repeated trials provide a useful method to estimate probability and variance [67]. Repeated measurements of kCARTA simulations with small perturbations to temperature and WVMR profiles are used in this work to determine the variance (ϵ^2) and uncertainty (ϵ), where the RMS error for the simulations represents the uncertainty (ϵ).

2.9 Retrieval Theory

2.9.1 Problem Formulation

The radiative transfer equation that operates with no error is defined as the forward function $f(x)$ [67]. The forward function perfectly models atmospheric radiation and is described by Equation 2.13.

$$y_{atm} = f(x, b) \tag{2.13}$$

where,

$$
\begin{aligned}
y_{atm} &= \textit{true spectra } (I(\nu)) \textit{ from atmosphere} \\
f(x,b) &= \textit{function which describes radiative transfer perfectly} \\
x &= \textit{atmospheric parameter of interest (i.e. CO profiles)} \\
b &= \textit{all other constituents in the atmosphere}
\end{aligned}
$$

In this project two different methods are used to determine the true atmospheric radiation (y_{atm}). (1) The AERI instrument measures downwelling infrared radiation. (2) Atmospheric radiation is modeled by kCARTA using knowledge of temperature and other constituents in the atmosphere. Each of these methods contains some error between itself and true atmospheric radiation. If it was possible to know the error on a case by case basis then perfect estimates of atmospheric radiation could be obtained; however, there are only statistical estimates of the error. Therefore, error is actually an uncertainty in each measurement.

The process for relating an AERI measurement to simulated kCARTA spectra is described by Equation 2.14. Each ϵ is the uncertainty between the true atmospheric state and either an AERI measurement or a kCARTA simulation. Therefore, the total uncertainty between AERI and kCARTA is a combination of the two.

$$
\begin{aligned}
y_{AERI} &= y_{atm} \pm \epsilon_{AERI} \\
y_{kCARTA} &= y_{atm} \pm \epsilon_{kCARTA} \\
y_{AERI} &= y_{kCARTA} \pm (\epsilon_{AERI} + \epsilon_{kCARTA}) \\
y &= F(x,b) \pm \epsilon
\end{aligned} \tag{2.14}
$$

where,

y = *refers to AERI measurements*

$F(x,b)$ = *refers to modeled spectra from kCARTA*

x = *variable to be retrieved (CO).*

b = *other parameters essential to the correct modeling of spectra (T,H_2O).*

ϵ = *combined uncertainty between AERI and kCARTA spectra.*

2.9.2 Jacobians

The inverse methods used to map measured spectra from AERI to measurements of CO require the RTE to be written in a linear form [67]. As previously stated, the RTE is a nonlinear function; however, for small changes in the state variable (x), the RTE is approximately linear. Depending on the degree of linearity, the linearized form of the RTE takes Equation 2.14 and writes it as $y = Kx$, or $\Delta y = K\Delta x$. K represents the Jacobian and formally is the derivative of the RTE with respect to a small change in the state vector. The Jacobian can be calculated analytically; however for this work the Jacobian is calculated using Equation 2.15.

$$\frac{\partial F(\nu_m)}{\partial x_n} = \frac{F(x_n + \sigma_n x_n, \nu_m) - F(x_n, \nu_m)}{\sigma_n x_n} = K_{mxn} \tag{2.15}$$

where,

$$
\begin{aligned}
F(x_n, \nu_m) &= \textit{kCARTA spectra using base state input} \\
F(x_n + \sigma_n x_n, \nu_m) &= \textit{kCARTA spectra using perturbed state input} \\
\nu_m &= \textit{wavenumber } (cm^{-1}) \textit{ with } m \textit{ channels} \\
\sigma(n)x_n &= \textit{perturbed state as a function of } n \textit{ layers} \\
x_n &= \textit{base state as a function of } n \textit{ layers} \\
\sigma_n &= \textit{size of perturbation as a function of } n \textit{ layers}
\end{aligned}
$$

In practice, σ_n varies in size and depends on the state variable being perturbed and which part of the electromagnetic spectrum is being modeled. Determining the magnitude of σ_n where the linear approximation of the RTE remains valid is required to calculate the Jacobian and for limiting the size of changes to the state variable from a retrieval. Also, σ_n may or may not be a function of pressure. In this work the CO Jacobian is calculated with a constant 10% ($\sigma = 0.1$) perturbation to CO column density values in RTP profiles.

2.9.3 Least Square Solution

This section provides the basis for the inversion process and formulates the simple equation which solves the retrieval problem. To illustrate the role different variables play in the inversion process a purely linear case will be presented first. Then, the formal iterative solution will be given.

A purely linear case without error begins with Equation 2.16. The goal is to minimize the difference between Kx and y.

$$y = Kx \tag{2.16}$$

This is done by finding the minimum in the cost function J shown in Equation 2.17. Finding the minimum in the cost function is done by taking the derivative of J with respect to x and finding its root. y is a $nx1$ vector, so J is a scalar value. Finding the minimum in J requires taking a derivative of a scalar with respect to a vector.

$$J = (Kx - y)^T(Kx - y) \tag{2.17}$$

$$J = x^T K^T Kx - y^T Kx - x^T K^T y + y^T y \tag{2.18}$$

$$\frac{\partial J}{\partial x} = 0$$

Multiplying Equation 2.17 out shows that J is made up of matrices multiplied by vectors.

The formal method for determining this derivative is given in [67, A.6] and the result is shown in Equation 2.19

$$\frac{\partial}{\partial x}[x^T Ax + \gamma^2 b^T x] = A^T x + Ax + \gamma^2 b \tag{2.19}$$

Now the terms from Equation 2.18 can be substituted into the general expression for the derivative given above.

$$y^T K = b^T$$

$$K^T K = A$$

$$\gamma^2 = 1 \tag{2.20}$$

The value of x which minimizes the cost function from Equation 2.19 is shown in

Equation 2.21

$$\frac{\partial J}{\partial x} = 2(K^T K\hat{x} - K^T y) = 0$$

$$K^T K\hat{x} = K^T y$$

$$\hat{x} = (K^T K)^{-1} K^T y \tag{2.21}$$

This least square solution assumes all information about the state variable x can be found from the measurements. It assumes no prior information about noise or the state. A simple example using the least square solution, taken from [84, 73, 40], demonstrates how the least squares solution works is now presented.

First, the assumption is made that an instrument and forward model exist that have no error. The instrument makes two measurements termed y_{true} given below. The state variable x_{true} is given below as well.

$$y_{true} = \begin{pmatrix} 2 \\ 4.0001 \end{pmatrix} K = \begin{pmatrix} 1.0000 & 1.0000 \\ 2.0000 & 2.0001 \end{pmatrix} x_{true} = \begin{pmatrix} 1 \\ 1 \end{pmatrix}$$

$$\hat{x} = \left(K^T K\right)^{-1} K^T y_{true} = \begin{pmatrix} 1 \\ 1 \end{pmatrix}$$

With a perfect instrument the retrieved quantity was exactly the same as the true quantity. What happens though if the instrument has a slight uncertainty in it?

$$y_{est} = y_{true} - \epsilon = \begin{pmatrix} 2 \\ 4.0001 \end{pmatrix} - \begin{pmatrix} 0 \\ .0001 \end{pmatrix} = \begin{pmatrix} 2 \\ 4 \end{pmatrix}$$

$$\hat{x} = \left(K^T K\right)^{-1} K^T y_{est} = \begin{pmatrix} 2.000 \\ 0 \end{pmatrix}$$

The uncertainty in y_{est} was four orders of magnitude less than the measurement, yet the retrieved quantity is over 100 percent in error. Let's make another example to compare:

$$y_{true} = \begin{pmatrix} 4.0000 \\ \\ 7.0000 \end{pmatrix} K = \begin{pmatrix} 1 & 3 \\ \\ 2 & 5 \end{pmatrix} x_{true} = \begin{pmatrix} 1 \\ \\ 1 \end{pmatrix}$$

The same uncertainty in the measurement will again be applied:

$$y_{est} = y_{true} - \epsilon = \begin{pmatrix} 4.0000 \\ \\ 7.0000 \end{pmatrix} - \begin{pmatrix} 0 \\ \\ .0001 \end{pmatrix} = \begin{pmatrix} 4.0000 \\ \\ 6.9999 \end{pmatrix}$$

And the least square solution for this process is presented below.

$$\hat{x} = \left(K^T K\right)^{-1} K^T y_{true} = \begin{pmatrix} .9997 \\ \\ 1.0001 \end{pmatrix}$$

The retrieved value of $\hat{x}$ in this example is much more accurate then the previous example's retrieved value for $\hat{x}$. In fact, the error in the retrieved value of $\hat{x}$ has the same magnitude as the noise. In each case the same error was applied and values of the true measurement were the same magnitude. The difference between the two examples is from their respective Jacobians. To understand the difference between the two examples, first define the gain as the linear mapping from measurement space to state space. A calculation for least square gain matrix is shown in Equation 2.22. When error terms for the forward model or instrument are estimated, the expected error in the state variable can be determined simply from $G\epsilon$. For any form of retrieval equation the gain matrix makes up all the variables preceding the

multiplication of the measurement.

$$G = \left(K^T K\right)^{-1} K^T \tag{2.22}$$

The gain matrix for each example is shown below. It should be noted that each term in the gain matrix for the first example is four orders of magnitude larger then the terms in the second example's gain matrix. Any error in the first example will be multiplied by a factor of 1E4, causing the solution to be highly oscillatory.

$$G_1 = \begin{pmatrix} 2.0001E4 & -1.0000E4 \\ -2.0000E4 & 1.0000E4 \end{pmatrix} G_2 = \begin{pmatrix} -5.0000 & 3.0000 \\ 2.0000 & -1.0000 \end{pmatrix}$$

The ideal K matrix is diagonal. If a diagonal K was an nxn matrix, then that would correspond to n linearly independent equations to solve x for. If x had m terms, and $m \leq n$, then x could be completely determined from the measurement. In the first example above, the K matrix was not diagonal. Close examination of the K matrix reveals the second row is nearly 2 times the first row. This means the Jacobian for this example is not a linearly independent quantity. The number of linearly independent rows in the K matrix define its effective rank [67]. If this rank is denoted p and the m quantities are greater than p, then some parts of x resides outside the effective row space of the measurement. Parts of the state that cannot be determined by the measurement are termed the *null* space of K [67].

Identification of the effective rank of K can be done with singular value decomposition [67]. The form of the singular value decomposition is shown in Equation 2.23. The number of non-zero singular values in K is the rank of K.

$$K = U\Lambda V^T \tag{2.23}$$

where the singular values for each case are given below:

$$\Lambda_1 = \begin{pmatrix} 3.1623 & 0 \\ 0 & 3.1622E-5 \end{pmatrix} \Lambda_2 = \begin{pmatrix} 6.249 & 0 \\ 0 & 1.602E-1 \end{pmatrix}$$

The second singular value for the first case is 5 orders of magnitude smaller than the first singular value. In contrast, the second singular value for the second example is only 1 order of magnitude smaller than its first value. Having rows that are linearly dependent cause the singular values to decrease rapidly. Equation 2.21 can be rewritten in terms of the singular value decomposition of K to examine the effect of the singular values. As is shown in Equation 2.24, any $\hat{x}$ value is a combination of the singular vectors U and V, while being divided by the corresponding singular value. In the first example, the second singular vector is on the order of 1E-5 and causes the gain matrix to be highly oscillatory for even a tiny measurement error. The higher singular values in the second example allow the second measurement to be less sensitive to error.

$$\begin{aligned} \hat{x} &= (K^T K)^{-1} K^T y \\ K^T &= V\Lambda U^T \\ \hat{x} &= (V\Lambda U^T U\Lambda V^T)^{-1} V\Lambda U^T y \\ \hat{x} &= V\Lambda^{-1} U^T y \\ \hat{x_i} &= \sum_{t=1}^{N} \frac{V_{i,t}(U^T y)_t}{\lambda_t} \end{aligned} \tag{2.24}$$

2.9.4 First Guess

When using inverse methods to map the state (CO profile) back to the measurement (AERI) many parts of the state reside in the null space of the measurement [67]. A well constructed first guess will constrict solutions of the retrieval equation to reasonable answers in the parts of the state where the measurement is not providing any information [67, 87]. Components of the state space that are contained in the effective row space are measured well enough that they are unaffected by the choice of a first guess [67, 87]. A first guess can use a climatology of measurements, models, or retrieval measurements from another instrument. A climatology of measurements or model can also be used to create an *a priori* profile and *a priori* covariance matrix for use in an optimal estimation method, where the *a priori* is the mean state of all the measurements [87].

This work compares a static first guess profile using an *a priori* profile, defined as the mean state of all 57 CO profiles from [90], to AIRSv5 CO used as the dynamic first guess profile. The purpose of using AIRSv5 CO profiles as a first guess is to improve the accuracy of retrieved CO in regions above 700 mb where SAAC has no sensitivity and AIRSv5 CO retrievals provide a better estimate of the true CO profile compared with the *a priori*.

Figures 2.13(b) and 2.13(b) present both averaging kernel matrices (AK) for the AIRSv5 and SAAC 5 layer respectively. Figures 2.13(b) and 2.13(b) both show that retrievals from either AERI or AIRS data only have one peak and only measure one piece of information about the atmosphere. Using the AIRS v5 CO product as

the first guess to SAAC makes use of the different sensitivity locations for each instrument's respective retrieval process.

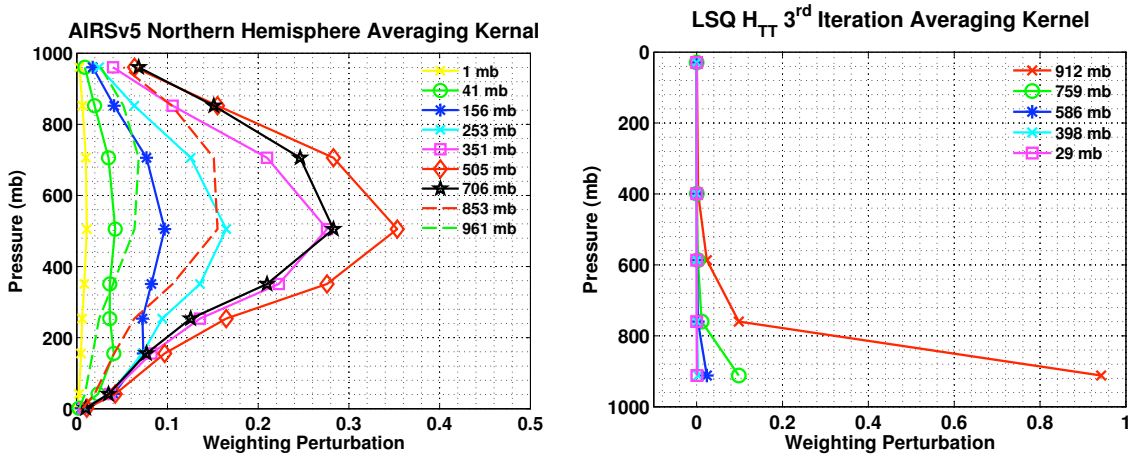

(a) (b)

Figure 2.13: (a) AIRS v5 AK with the effective pressures for each row of the AK listed in the legend. This plot comes from [87]. (b) SAAC averaging kernel. The components for this retrieval use a diagonal constraint matrix called H_{TT} and a 5 layer retrieval grid. These components are defined in Chapter 4.

2.9.5 Information Content

Three different diagnostic variables were used to determine information contained in the retrieval system are briefly described below:

1. **SVD:** The Jacobian matrix K was decomposed into its eigenvectors and eigenvalues described by equation 2.23. A transformation of the linear problem to an orthogonal basis the number of pieces of information greater than measurement error can be determined. The number of singular values greater than

one from $S_\epsilon^{-1/2} K S_a^{1/2}$ is the effective rank of the measurement space [67, Ch 2.]

2. **Degrees of Freedom (DOF):** The degrees of freedom separate the measurement signal into two components. The first component is the number of degrees of freedom due to the signal d_s, and the second component is the number of degrees of freedom due to error d_e. Results from this work use d_s to describe information of the SAAC retrieval.

3. **Shannon information content:** This concept was originally developed to describe information carrying capacity of communication channels [70]. It relates the entropy of the system before and after a measurement is made.

2.9.6 Degrees of Freedom, Gain Matrix, and the Averaging Kernel

The purpose in calculating the degrees of freedom (DOF) is to separate how many independent pieces of information are contained in the signal (d_s) from how many independent pieces of information are contained in the noise (d_n). DOF are calculated under the assumption that the prior state *pdf* and error *pdf* have a Gaussian distribution, and the mapping made by the retrieval is a linear process. There are not enough CO profiles to create a *pdf* of the prior state; however, it has been shown that CO has a log-normal distribution [14].

The expression for calculating the DOF for the signal is taken from [67, Ch. 2] and is given by:

$$d_s = trace([K^T S_e^{-1} K + S_a^{-1}]^{-1} K^T S_e^{-1} K) \tag{2.25}$$

where S_e and S_a are the error and *a priori* covariance matrices respectively. In the least square solution from Section 2.9.3, a gain matrix is defined as all the components that propagate the measurement to the retrieval. This is demonstrated by the differential form of the gain matrix $G = \frac{d\hat{x}}{dy}$. The general form of the gain matrix in a retrieval is demonstrated below:

$$\hat{x} - x_a = G(y - Kx_a)$$

, where for this case $G = (K^T S_e K + S_a^{-1})^{-1} K^T S_e^{-1}$.

Substituting the gain matrix into Equation 2.25 simplifies the expression which calculates the DOF for the signal, as seen below.

$$d_s = trace(GK) \tag{2.26}$$

A calculation for the DOF of the signal than is simply the trace of the gain matrix G times the Jacobian matrix, K. This quantity is commonly known as the the averaging kernel (AK) [3]. As it is shown in Equation 2.27, the AK maps changes in the true state back to the retrieved state.

$$A = \frac{d\hat{x}}{dx} \tag{2.27}$$

The averaging kernel has two primary functions. First, it describes the sensitivity that a retrieved state variable has in relation to the true profiles. The rows of the averaging kernel describe the sensitivity a layer in the retrieved state has to changes in the true state. An ideal averaging kernel would be a series of delta functions. Thus each retrieved layer would be effected in the corresponding true layer. The

solution for the averaging kernel (A) is

$$A = GK \tag{2.28}$$

The DOF due to the signal can be calculated using Equations 2.25- 2.26. Equation 2.26 is easily derived by remembering that the gain matrix for any retrieval problem is all the quantities that used to map the measurement vector y to the retrieved state $\hat{\text{h}}$at. This is shown in differential form with Equation 2.29.

$$G = \frac{d\hat{x}}{dy} \tag{2.29}$$

2.9.7 Shannon Information Content (H_S)

The result of making a measurement improves the knowledge of a quantity. Therefore, a *pdf* which describes the probability that x is in a certain state has its variance and entropy reduced through measurement. Shannon used the entropy of the system as a way to quantify the amount of knowledge of the state. Shown in Equation 2.30, the entropy of a system defined by Shannon, is the same as the Gibbs thermodynamic definition of entropy apart from the Boltzmann constant.

$$S(P) = -k \sum_i p_i ln p_i \tag{2.30}$$

If two *pdf*s, $P1$ and $P2$ correspond to states before, and after a measurement, then the information content of the process is calculated as the reduction in entropy [70]. This relationship is demonstrated below:

$$H_S \;\; = \;\; S(P_1) - S(P_2) \tag{2.31}$$

In practice, the Shannon information content of the system (H_S) is measured in bits as it was first developed to describe the information carrying capacity of communication wires [67]. The relationship used to calculate H_S is seen below:

$$H_S = -\frac{1}{2}\left|I_n - A\right| \tag{2.32}$$

Beginning with the relation for a reduction in entropy shown in equation 2.31, it is possible to relate Shannon information content (H_S) to degrees of freedom (d_s), singular values (λ) of K, and the averaging kernel (A). Derivations of the relationship between these values are straight forward when starting with the definition of entropy for a Gaussian distribution as described in [67, Ch. 2]. The relationships between all quantities used to determine information in the retrieval system are shown in Equations 2.33 and 2.34.

$$H_S = -\frac{1}{2}\left|I_n - A\right| = \frac{1}{2}\sum_i ln(1+\lambda^2) \tag{2.33}$$

$$d_s = trace(A) = \sum_i \frac{\lambda_i^2}{1+\lambda_i^2} \tag{2.34}$$

Chapter 3

Error Analysis

3.1 Cloud Filtering

Observed spectra from AERI is greatly affected when the FOV contains clouds. Portions of the spectra known as window channels, which normally receive radiation from very high in the atmosphere, receive radiation from much lower in the atmosphere during periods of cloudiness. Each different cloud type, ranging from thin cirrus to the thicker cumulus clouds, has its own characteristic effect on AERI spectra. Each AERI spectra results from an observation of the sky over a 3 minute period of time and clouds may fill the FOV for either the total amount of time or a fraction of that 3 minutes. Modeling the effect from each of the cloud scenarios would be quite difficult with kCARTA. Therefore, a method which effectively identifies cloudy spectra is required. This section gives an overview and directly compares two different methods that identify cloudy spectra.

The first AERI cloud flagging technique looks for a spectral contrast of 40 K in AERI spectra corresponding to the band between 2100 and 2200 cm^{-1} [28, 34, 90]. Spectra is converted from radiance to brightness temperature (K) by inverting the Planck function from Equation 2.2 and solving for temperature.

Clouds emit radiation like a blackbody with a brightness temperature close to its atmospheric temperature across all spectral channels. Therefore, an AERI

spectra observing a cloud in its FOV will have a small contrast in measured spectra converted to brightness temperature. Examples of cloudy spectra are shown in Figure 3.1 as vertical lines of the same color. This time series of AERI spectra shows clouds occurred from 0-3, 6-8, 12, and around 18 GMT. Searching for a brightness temperature contrast of 40 Kelvin is successful when thick clouds under 5 km in height fill the AERI FOV [50]. This method does not identify thin cirrus, or scenes that are only partially filled in time or space by clouds.

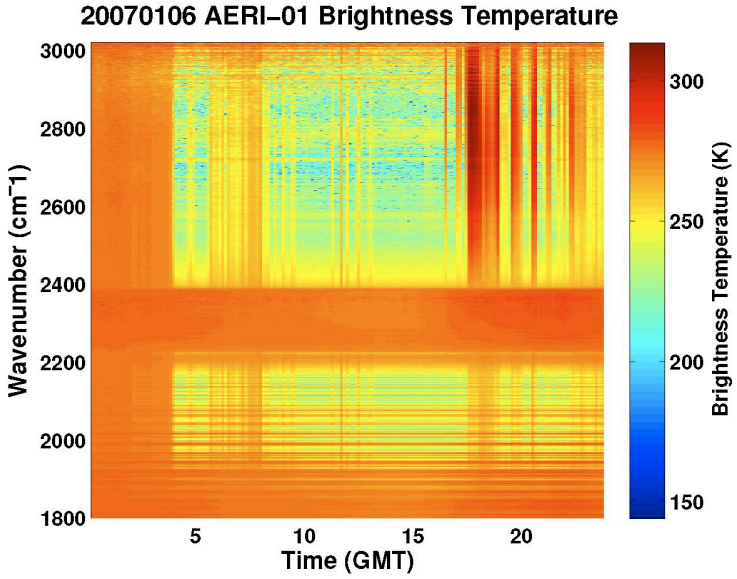

Figure 3.1: Time Series of AERI spectra converted to brightness temperatures for 20070106 from AERI-01 instrument located at SGP.

A new cloud flagging technique for AERI spectra has been developed that uses a neural network trained on AERI spectra, ceilometer measurements, and LIDAR measurements [80]. Figure 3.2 displays a histogram of measured AERI brightness temperatures for the 985 cm^{-1} window channel taken from [80]. A tri-modal behavior is displayed in the total history of measurements represented by the black

line. The neural network was applied to the spectra in order to differentiate clear sky from cloudy sky. Thin and thick clouds are differentiated by averaging spectra at 985 cm^{-1} for 70 minutes and either being less than or greater than 250 K. The third peak in the total history is clearly shown to be from thick clouds while the other two peaks are shown to be from a combinations of thin cloud and clear sky conditions.

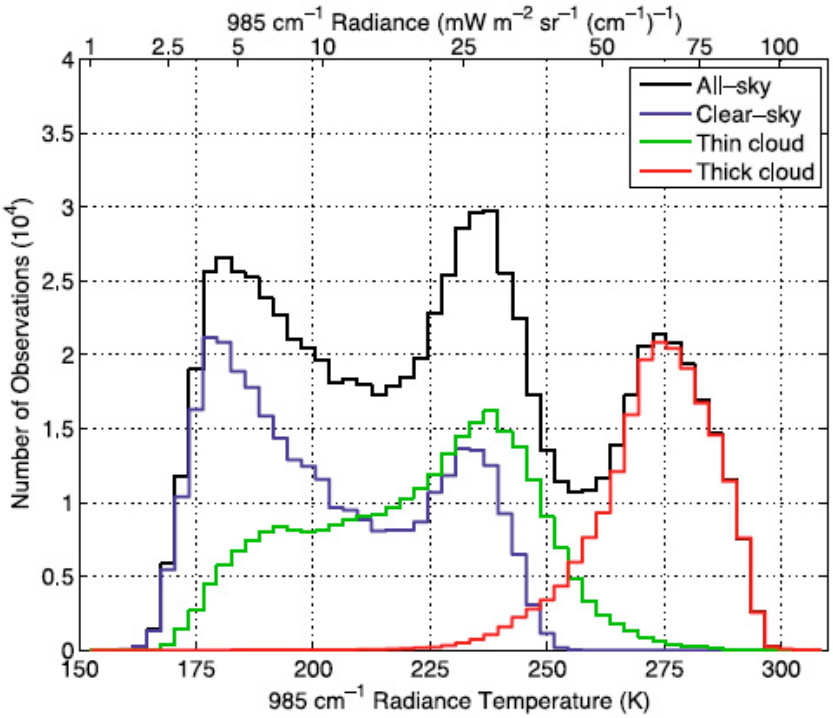

Figure 3.2: Cloud climatology plot from [80]. Clouds are flagged via a neural network, and 250 (K) was chosen as a threshold between thin and thick clouds.

Shorthand notation will be used to describe each method of cloud flagging for the remainder of this dissertation:

- **BT**: Cloud flags using the brightness temperature contrast of 40 K [28].
- **NN**: Cloud flags using the neural network in [80] are provided by [78].

Both methods of cloud flagging are applied to 2007 AERI spectra. First, bad spectra, those resulting from poor calibration or a closed hatch over the instrument, for the 2007 data set were identified by direct visual inspection and thrown out. Then, the BT cloud flags were collocated in time with NN cloud flags provided from [78]. Table 3.1 shows that the neural network greatly reduces the number of spectra classified as clear compared with BT.

Cloud Filter	Total Spectra	Spectra Analyzed	Clear Days	Percent Clear
BT	62964	57345	37319	65
NN	62964	58852	13735	23

Table 3.1: Summary of cloud analysis on 2007 AERI data

Following methodology from [80], a threshold of 250 K in the window channel at 2133 cm^{-1} is used to differentiate thin clouds from thick clouds for the BT cloud filter. Figures 3.3(a) and 3.3(b) are histograms of the 2133 cm^{-1} brightness temperature for the AERI 2007 data set with the BT and collocated NN cloud flag techniques applied. These two figures show that the 2133 cm^{-1} channel has the same tri-modal behavior as in the 985 cm^{-1}. Directly comparing Figure 3.3(a) with Figure 3.3(b) reveals that the BT cloud filter misclassifies AERI spectra with thin clouds in the FOV as clear. Previous studies using AERI spectra likely were affected by the thin cirrus clouds in the spectra [34, 90]. In fact, the large increase in AERI retrieved PWV shown around 3 UTC from Figure 2.12 is likely due to the presence

of a cloud that was not flagged by the BT cloud flag. The NN cloud flag's ability to determine spectra affected by thin cirrus provides a significant improvement over BT cloud filter and allows for a better examination of the error sources affecting kCARTA modeling.

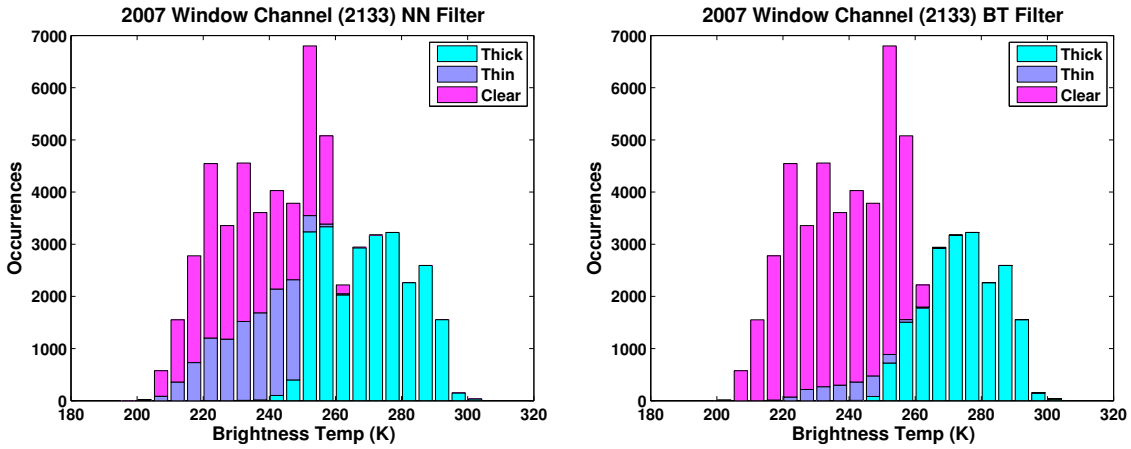

(a) (b)

Figure 3.3: (a) Histogram cloud analysis on all AERI-01 spectra by the neural network method. (b) Histogram cloud analysis on all AERI-01 spectra using brightness temperature contrast to search for clouds.

3.2 kCARTA Input Analysis

A forward model calculates radiance based on the radiative transfer equation defined in Equation 2.4. The Planck function, $B[\nu, T(p)]$, and the transmittance $\tau(\nu,p)$ need to be calculated at every point in the atmosphere. An accurate calculation of the fractional transmittance $\tau(\nu,p)$ requires knowledge of various atmospheric constituents' distributions by height, and the subsequent quantum mechanical tran-

sitions for each molecule. For a given portion of the electromagnetic spectrum, only certain gases are radiatively active. Therefore, three options exist for a gas' inclusion into the forward model:

1. **Ignored**: The gas molecule absorbs no energy at the given wavelength and does not need to be included in the forward model.

2. **Referenced**: Absorption by the gas molecule is small or the variability of the gas is small enough that a reference profile can be included to the forward model.

3. **Dynamically Included**: The gas molecule has a significant absorption and changes enough over time that no reference profile can be used. Thus the best estimate of gas distribution must be included in the forward model as input in order to achieve some desired accuracy.

A sensitivity study is presented here to determine which gases need to be dynamically included, referenced, or ignored. The study compares the size of the CO Jacobians to the size of the Jacobians of other significant gases. The Jacobian expression from Equation 2.15 is used to calculate Jacobians for ozone, water, nitrogen dioxide, and carbon dioxide. Temperature is calculated analytically by kCARTA.

Figure 3.4(a) shows that the results which compare temperature, water, and CO radiances change corresponding to a small perturbation in their lower tropospheric profile. Figure 3.4(a) shows that small perturbations in temperature and water vapor profiles will dominate this region and can hide the CO signal. Including reference profiles for temperature and water vapor does not provide the adequate

accuracy that is needed to model spectra. Therefore temperature and water vapor profiles retrieved from AERI spectra will be used in every kCARTA simulation. Figures 3.4(b) - 3.4(d) compare the CO Jacobian to Jacobians for N_2O, O_3, and CO_2 respectively. These figures demonstrate that the CO signal is much larger than the signal corresponding to small perturbations in other trace gases in this region. Therefore, reference profiles from the 1976 US standard atmosphere is used for N_2O, O_3, CO_2, and many other gases in kCARTA. The spectral channels corresponding to the two peaks in Figure 3.4(d) are not used to retrieve CO. This avoids possible errors in simulated spectra due to errors from the CO_2 profile used.

3.3 Error Simulations

A computer simulation was setup which simulates how error in the AERI retrieved temperature and water vapor profiles input into kCARTA project onto simulated spectra. This simulation examined the entire 2007 data set of AERI retrieved temperature and water vapor profiles from SGP. Cloud free profiles are determined by collocating in time the AERI retrieved profiles with the NN cloud flags. This resulted in 13735 sets of profiles to build the simulation with. The bias and RMS values for both temperature and water vapor retrievals from Figure 2.11 are propagated randomly through the kCARTA set to determine error due to profiles input to kCARTA.

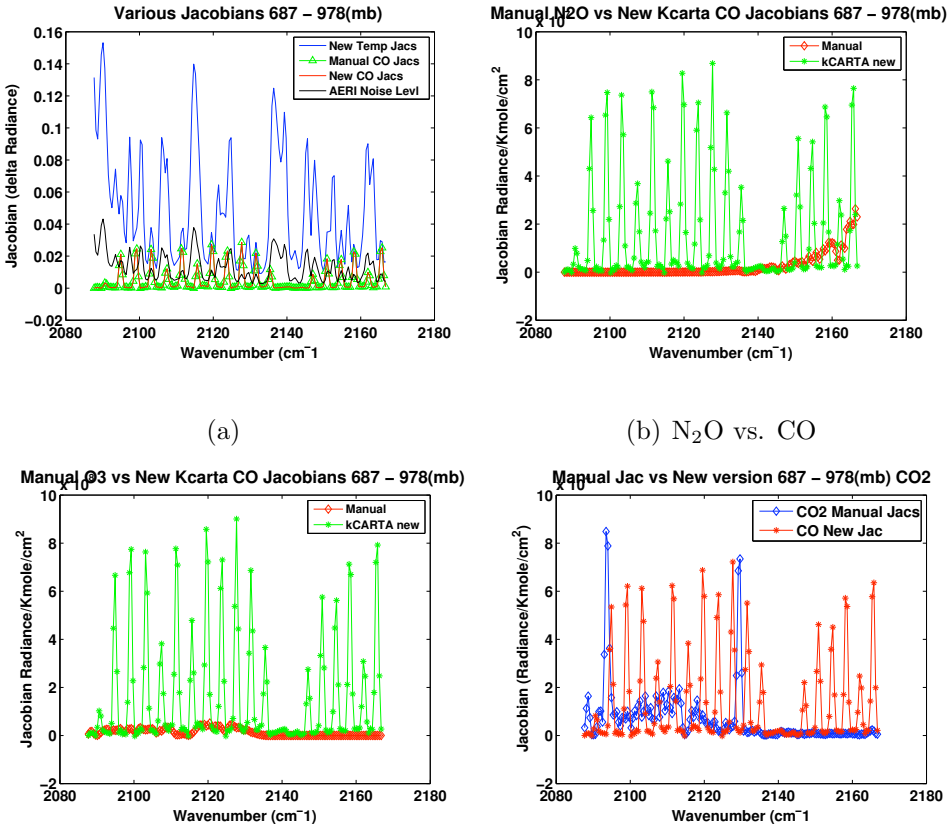

(a)

(b) N_2O vs. CO

(c) O_3 vs. CO

(d) CO_2 vs. CO

Figure 3.4: (a) Temperature, water vapor, and CO Jacobians. Water and CO Jacobians are multiplied by a 10 percent variation of their gases column amount. Temperature Jacobian is for a 1K difference. Noise level is simulated as 1 percent of the measured radiance. (b) N_2O Jacobian is calculated using Equation 2.15 with a 1% perturbation.(c) O_3 Jacobian is calculated using Equation 2.15 with a 1% perturbation. (d) CO_2 Jacobian is calculated using Equation 2.15 with a 1% perturbation. For (b) - (d) CO Jacobian calculated by Equation 2.15 using a 10% perturbation. The perturbation sizes are chosen to assure the radiative transfer equation is approximately linear for a given percent change in gas amount.

3.3.1 Temperature Simulation

The process for adding error randomly to the 13735 temperature profiles starts by defining two parameters, $a(h)$ and $b(h)$, which are both functions of the validated [72] bias and RMS values for temperature. T_{bias} and T_{RMS} are found by examining Figure 2.11.

$$a(h) = T_{Bias}(h) - \alpha T_{RMS}(h) \tag{3.1}$$

$$b(h) = T_{Bias}(h) + \alpha T_{RMS}(h) \tag{3.2}$$

Each of these parameters are defined on the same geopotential height grid (h) that is standard output with the AERI retrieved temperature and water vapor retrievals [22]. Figure 3.5 displays the bias (red) and RMS (blue) used as input to $a(h)$ and $b(h)$.

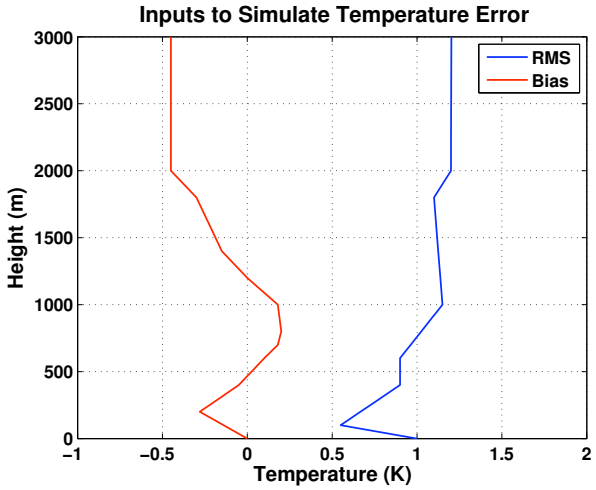

Figure 3.5: Bias and RMS profiles for the AERI retrieved temperature product taken from an AERI temperature and water vapor validation study [72].

The bias and RMS values in Figure 3.5 are taken from the AERI temperature

and water vapor validation study [72]. Bias and RMS values of -.45 K and 1.3 K were used above 3000 meters respectively.

Once the parameters $a(h)$ and $b(h)$ are created they are input into Equation 3.3 in order to create 13735 temperature error profiles.

$$\Delta T(h_i) = a(h_i) + [(b(h_i) - a(h_i))N(h_i)] \tag{3.3}$$

The variable N inside Equation 3.3 is a vector containing a uniform distribution of 13735 random numbers between 1 and 0. Computation of $\Delta T(h_i)$ is carried out with a for loop that circulates over the height index i.

The set of temperature profiles with simulated error is easily calculated since both the temperature profiles (T) and the temperature error profiles ($\Delta T(h)$) are the same size matrix (lxN), where l is the total number of heigh layers in the geopotential grid h and N stands for the 13735 profiles.

$$T_{error} = T + \Delta T \tag{3.4}$$

T_{error} in Equation 3.4 represents the set of temperature profiles with the validated RMS and bias errors mapped onto them. When Equation 3.4 was first calculated it was found that the output RMS was too small and did not match the input RMS from Figure 3.5. For this reason a scaling term (α) is used in Equations 3.1 and 3.2 to increase the output RMS values. For the temperature simulation this factor is found to be 1.66. Figure **??** shows that the RMS and bias computed from the set of 13735 temperature and temperature with error profiles is a good match to the validated RMS and bias profiles in Figure 3.5.

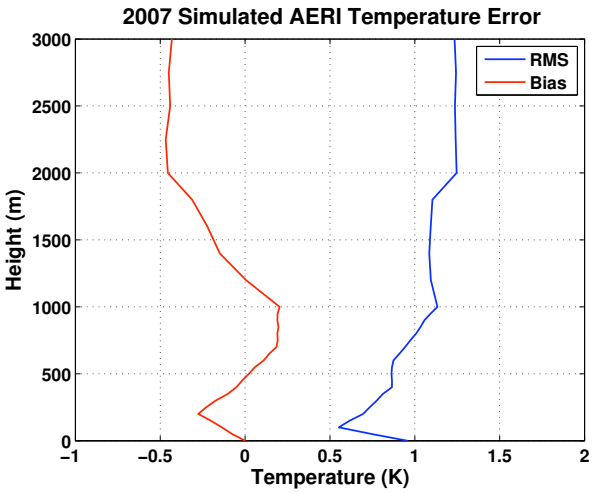

Figure 3.6: Output profiles of RMS and bias once error is added to the temperature profile. Bias is calculated as the mean of $T - T_{error}$

3.3.2 Water Vapor Profile Simulation

Adding error to the 13735 AERI retrieved water vapor profiles is a process similar to the temperature simulation; however, because water vapor mixing ratio (WVMR) profiles are much smaller in magnitude, simply adding random error causes some profiles to contain negative values. Therefore, the error must be added as a percentage change to the profile.

The process for adding error randomly to the 13735 WVMR profiles starts by defining the mean WVMR profile ($\overline{W}$) in Equation 3.5, with N equaling 13735.

$$\overline{W(h)} = \frac{1}{N}\sum_{i=1}^{N} W(h) \tag{3.5}$$

Next, profile parameters $a(h)$ and $b(h)$ are defined in equations 3.6 and 3.7 respectively. These parameters are functions of the mean profile from equation 3.5 and the bias and RMS profiles shown in Figure 3.7(a). Bias and RMS profiles are

based on the results from the AERI validation study in [72].

$$a(h) = \frac{\overline{W} - W_{Bias}}{\overline{W}} - \alpha \frac{W_{RMS}}{\overline{W}} \tag{3.6}$$

$$b(h) = \frac{\overline{W} - W_{Bias}}{\overline{W}} + \alpha \frac{W_{RMS}}{\overline{W}} \tag{3.7}$$

Once the parameters $a(h)$ and $b(h)$ are created they are input into Equation 3.8 in order to create 13735 fractional WVMR error profiles. The variable N inside Equation 3.8 is a vector containing a uniform distribution of 13735 random numbers between 1 and 0. Computation of $\Delta W(h_i)$ is carried out with a for loop that circulates over the height index i.

$$\Delta W(h_i) = a(h_i) + [(b(h_i) - a(h_i))N(h_i)] \tag{3.8}$$

The set of WVMR profiles with simulated error is easily calculated since both the WVMR profiles (W) and the WVMR fractional error profiles ($\Delta W(h)$) are the same size matrix (hxN). W_{error} in Equation 3.9 represents the set of WVMR profiles with the validated RMS and Bias errors mapped onto them. RMS and Bias Output profiles from this simulation are displayed as the solid red and blue lines respectively in Figure 3.7(b).

$$W_{error} = W\Delta W \tag{3.9}$$

3.3.2.1 MWR Constraint Simulation

To simulate the effect of constraining WVMR profiles with MWR data, Equation 2.10 , that describes how to constrain the water vapor profile from AERI, is adjusted. In order to get Equation 3.10 from Equation 2.10, W is substituted for

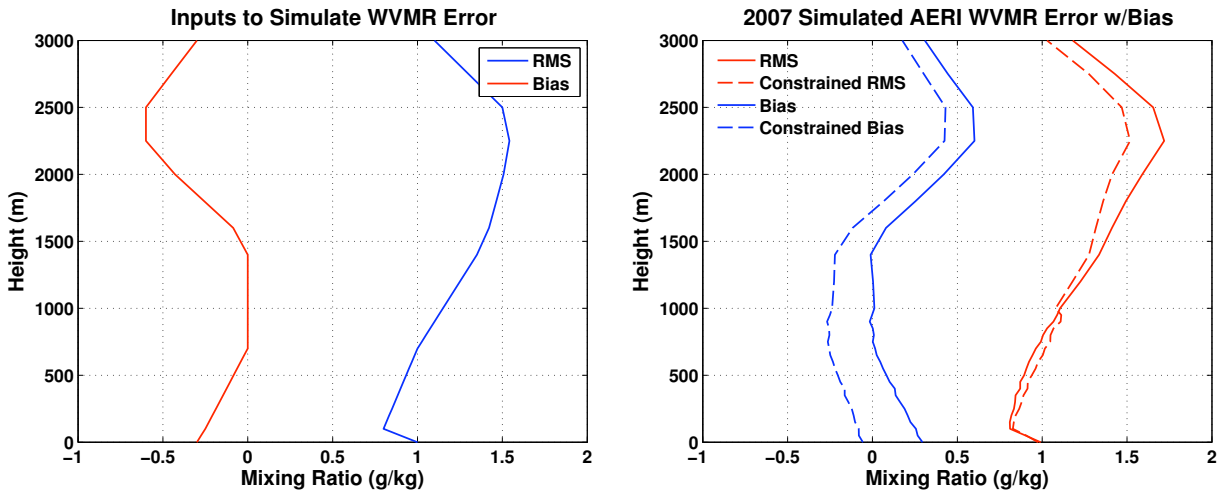

(a) Input

(b) Output

Figure 3.7: (a) Bias and RMS profiles for the AERI retrieved WVMR product taken from an AERI temperature and water vapor validation study [72]. These are used in Equations 3.6 and 3.7. (b) Bias and RMS statistics calculated between W and W_{error}. The constrained RMS and bias profiles are calculated from W and W_{error}, where W_{error} is constrained by a simulated MWR measurement. Equation 3.10 demonstrates how the WVMR profile is constrained by use of an MWR. Bias is calculated as the mean of $W - W_{error}$.

MWR data and W_{error} is substituted for AERI WVMR data.

$$Constrained\ W_{error} = \frac{TPW(W)}{TPW(W_{error})} W_{error} \tag{3.10}$$

As shown in the dashed profiles in Figure 3.7(b), constraining the WVMR profile with MWR data shifts the bias to the left (making it more negative). The constrained RMS (dashed red) profile in Figure 3.7(b) is smaller above 1000 meters when compared with the normal RMS profile (solid red). Therefore the simulation shows that MWR does improve the accuracy of the profile, but the improvement is above 1000 meters. The improvement in modeled spectra from using MWR is likely to be small because the effect that errors in the WVMR profile have on modeled spectra decreases with height.

3.3.3 kCARTA Model Error

The uncertainty in synthetic spectra from kCARTA due to uncertainty in modeling absorption lines represents an imperfect knowledge of the underlying physics in radiative transfer. Absorption line parameters for atmospheric constituents that make significant contributions in the CO band (2100-2200 cm^{-1}) are perturbed in order to understand how the uncertainty propagates through kCARTA. There are a total of 4 variables to perturb, with three dealing with modeling water, and one from the modeling of CO. Due to the complexity of modeling a water molecule, modeling its absorption coefficients is separated into water lines, self absorption, and foreign broadening [23]. Percent uncertainty for all species modeled is shown in Table 3.2 and were determined from [27].

Source	H_2O	Foreign	Self	CO
Percent Uncertainty	10	10	10	5

Table 3.2: Percent changes to absorption coefficients used to calculate σ terms.

One set of AERI retrieved temperature and WVMR profiles in September is chosen to run this modeling simulation. The PWV from this day had its average annual value. The uncertainty in a kCARTA simulation due to one of the absorption coefficients from Table 3.2 is the difference between a base state simulation and a perturbed state simulation. This calculation is demonstrated in equation 3.11.

$$\epsilon_a(\nu) = F(a\sigma_a, \nu) - F(\nu) \tag{3.11}$$

where,

$$\begin{aligned}
\epsilon_a(\nu) &= \textit{kCARTA uncertainty spectra (brightness temperature or radiance)} \\
F(\nu) &= \textit{Spectra produced from kCARTA} \\
F(a\sigma_a, \nu) &= \textit{Spectra produced from kCARTA with perturbation to abs. coeff.} \\
a &= \textit{A constituent from Table 3.2} \\
\sigma_a &= \textit{Multiplicative factor for constituent } a\textit{(ex. } a = CO\textit{, } \sigma_a = 1.05\textit{)} \\
\nu &= \textit{Wavenumber } cm^{-1}
\end{aligned}$$

Figure 3.8(a) displays the results from the simulation as brightness temperature. This figure demonstrates that the uncertainty in water is the most dominant term followed by self and foreign broadening, while uncertainty in CO lines have a small but non-negligible effect. Because each kCARTA modeling error term is independent of one another the error terms are added in quadrature. Quadrature

addition for the errors give:

$$\epsilon_{total}(\nu) = \sqrt{\sum_{i=1}^{N} \epsilon_i^2(\nu)} \tag{3.12}$$

On water lines the total modeling error is shown in Figure 3.8(a) to be around 1K in the CO band, with decreasing values past 2140 cm^{-1}. Figure 3.8(b) displays the error terms in radiance units. This figure compares total error, total water, and CO. Total water is the sum of water, foreign, and self broadening features and demonstrates that the total uncertainty in modeling water dominates the entire band, and uncertainty in CO is only comparable in a small band from 2160 -2190 cm^{-1}.

3.3.4 AERI Error Simulation

Principal Component Analysis (PCA) is an effective technique for reducing the dimensionality of large data sets that are characterized by many interdependent variables [1] and has shown to be an effective method for removing uncorrelated error that exists in AERI spectra [81]. In this study PCA is used to estimate the error rather than remove it.

The process begins by taking many spectra measurements from AERI, where each spectra produced by AERI contains an atmospheric component and a noise component. This is demonstrated in equation 3.13.

$$y_{AERI}(\nu_n) = y_{atm}(\nu) \pm \epsilon(\nu) \tag{3.13}$$

The entire AERI-01 data set for 2007 comprised 62964 AERI measurements of which 58852 could be collocated in time with the NN cloud flag. Removing AERI spectra

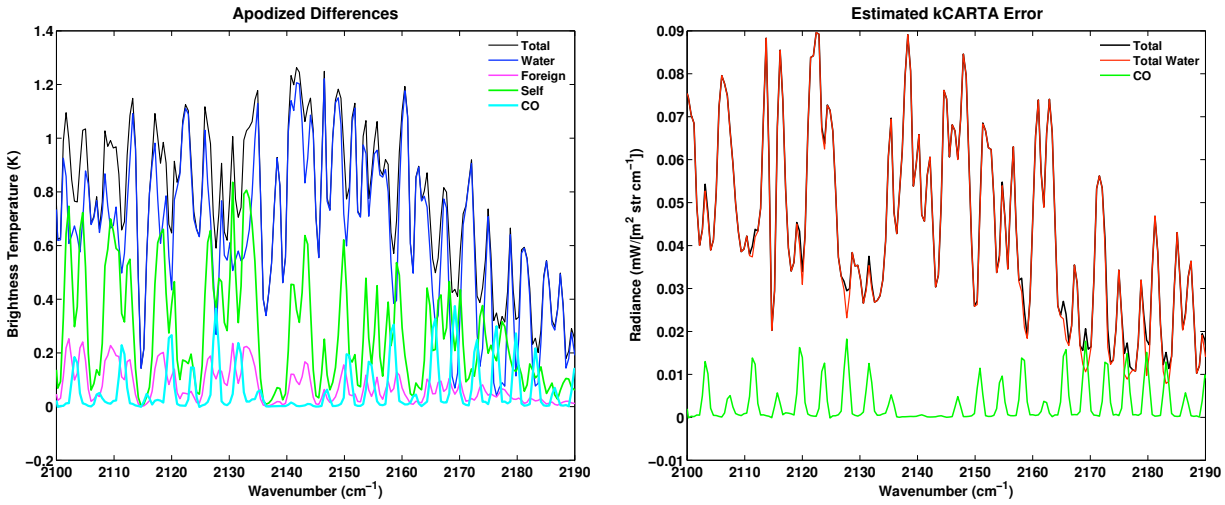

(a) (b)

Figure 3.8: (a) All the different terms used to model the uncertainty kCARTA modeling error measured in brightness temperature (K). (b) Total modeled error, total water error, and error terms from CO are presented here in radiance units. Total water is the uncertainty in water lines, self broadening, and foreign broadening. Total is all the terms added together. Error terms are added together using equation 3.12

that observes clouds results in 22679 cloud free spectra that each contain roughly 500 spectral channels. This provides sufficient amount of data to meet the requirement that there be at least two times as many sets of spectra as there are spectral points [1].

The entire set of AERI measurements is written as a matrix, L_{mxn}, where m is the number of AERI spectra and n is the number of spectral channels. The mean spectrum for all AERI measurements is then calculated in using equation 3.14.

$$\overline{L}_{1xn} = \frac{1}{M} \sum_{i=1}^{M} L_{ixn} \tag{3.14}$$

The mean spectrum then is used to create an $\overline{L}_{mxn}$ mean matrix that is used in Equation 3.15 to calculate deviation from the mean ($\tilde{L}_{mxn}$) for each spectrum.

$$\tilde{L}_{mxn} = L_{mxn} - \overline{L}_{mxn} \tag{3.15}$$

Principal components usually are calculated as the eigenvectors determined from the nxn spectral covariance matrix (C_{nxn}) [81]. Eigenvectors of C are the same as the eigenvectors of L_{mxn} [44] and are easier to create because C is a symmetric real valued matrix. The spectral covariance matrix is given by

$$C_{nxn} = \tilde{L}^T \tilde{L} \tag{3.16}$$

Singular value decomposition (SVD) is used to determine the eigenvectors and eigenvalues of C_{nxn}. The standard SVD routine provides a numerically stable and well behaved approach to calculating the eigenvectors and eigenvalues [64]. The computation is done using the standard Matlab svd routine: $U_{nxn} S_{nxn} V_{nxn}^T = svd(C)$, where the eigenvectors are the row vectors in U_{nxn} and the eigenvalues (λ) are the

diagonal in S. Eigenvalues describe the variance of the measurement set and are ordered such that they are sequentially decreasing ($\lambda_0 > \lambda_1 > \lambda_2 > ....\lambda_n$). Large eigenvalues contain information about the variance of the atmopshere, while smaller eigenvalues describe variance due to noise of the instrument [1]. The next step is to determine which eigenvectors relate to atmospheric variation, and then to use only them to reconstruct the original data set [1].

The minimum in an empirical function, called the factor indicator (FI) [43], is used to determine how many principal components to use in reconstructing the AERI data set. This function defined by

$$FI(k) = \frac{RE(k)}{(n-k)^2} \tag{3.17}$$

where,

$$RE(k) = \frac{\sum_{i=k+1}^{n} \lambda_i}{m(n-k)} \tag{3.18}$$

is solely determined on the the magnitude of the eigenvalues (λ), the number of spectra (m), and the number of spectral channels (n) in L_{mxn}. The number k states how many eigenvalues describe atmospheric variation, and eigenvalues $1 \rightarrow k$ are retained in the data set.

Equation 3.18 describes the real error in the data set [44]. Computations for RE and then FI are computed for values of k, ranging from $1 \rightarrow n-1$. The computation begins and $k = 2$ because the first eigenvalue is assumed to describe real atmospheric variation. Then the value of k that corresponds to the minimum in the FI function is used to reconstruct the data set. For a data set with uniform

random error (Gaussian distributed error with constant standard deviation for all spectral points and times) the minimum in the FI function is the correct choice for k [43].

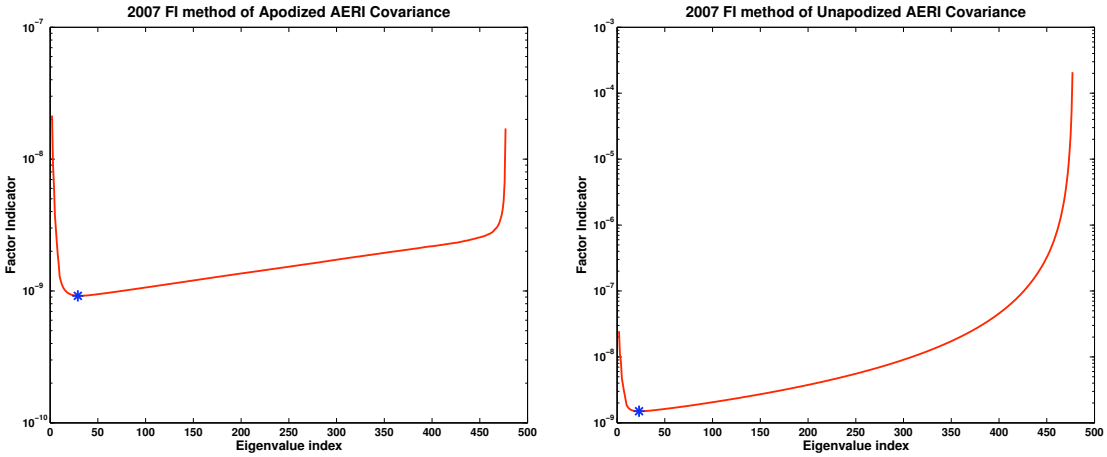

(a) Apodized FI Function

(b) Unapodized FI Function

Figure 3.9: (a) FI function (red) for apodized AERI data set with the blue star corresponding to the minimum.(c) FI function (red) for unapodized AERI data set with blue star corresponding to the minimum.

Plotted in Figures 3.9(a) and 3.9(b) are calculations of the FI function for eigenvalues corresponding to apodized and unapodized AERI data sets respectively. In each figure the blue star represents the minimum. The minimum in the FI function for the apodized AERI data corresponds to 23 eigenvalues and the minimum for the unapodized AERI data set corresponds to 30 eigenvalues. Less variation is described in the lower eigenvalues corresponding to the apodized data set because apodization acts like a running mean across the spectral channel, thereby reducing the spectral variation.

Figures 3.10(a) and 3.10(b) show that the eigenvalues not used in the reconstruction carry little information. The long flat part of Figures 3.10(a) and 3.10(b) represents eigenvalues describing variation due to the instrumental noise of the data set. Noisy eigenvalues for the unapodized AERI data set are approximately an order of magnitude higher than the noisy eigenvalues for the apodized AERI data set. A

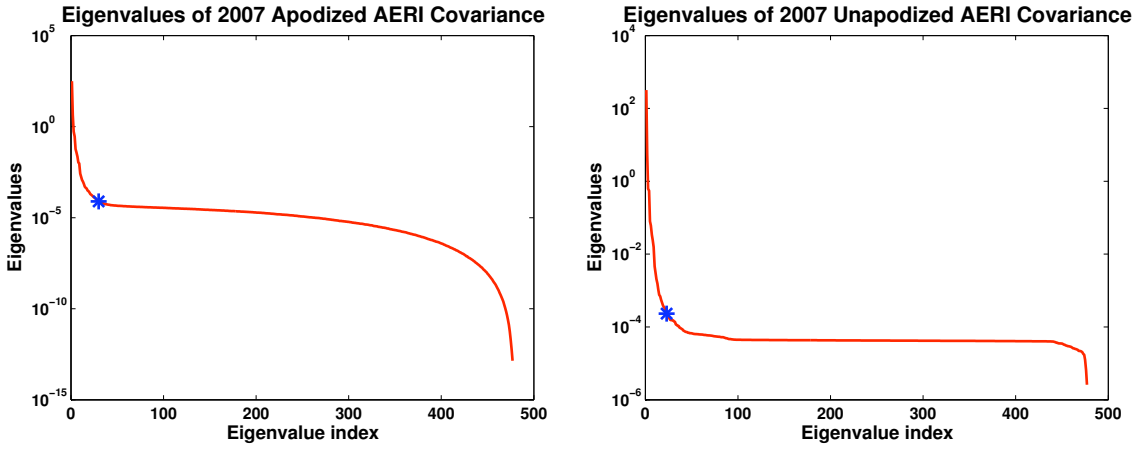

(a) Apodized Eigenvalues

(b) Unapodized Eigenvalues

Figure 3.10: (a)Eigenvalues (Red) for apodized AERI data set with blue star corresponding to the minimum in the FI function. (d) Eigenvalues (Red) for unapodized AERI data set with blue star corresponding to the minimum in the FI function.

low rank eigenvector matrix is created from the full set of eigenvectors (U_{nxn}) once the appropriate number of eigenvalues is determined from the FI function. If the FI function determines that k eigenvalues have contributions from the atmosphere, then the low rank eigenvector matrix is $\hat{U}_{nxk} = U_{nx(1\rightarrow k)}$ and the estimated AERI

data matrix is calculated as:

$$L_{mxn}^{low} = \tilde{L}_{mxn}\hat{U}_{nxk}(\hat{U}^T)_{kxn} + \overline{L}_{mxn} \tag{3.19}$$

Figure 3.11(a) takes one spectrum and demonstrates the similarity between the reconstructed AERI and the original AERI data. The RMS error is calculated in Equation 3.20 to determine the amount of uncertainty (ϵ_y) of the apodized and unapodized AERI data sets.

$$\epsilon_y(\nu) = \sqrt[2]{\frac{1}{m}\sum_{i=1}^{m}[L_{ixn}(\nu) - L_{ixn}^{low}(\nu)]^2} \tag{3.20}$$

Figure 3.11(b) demonstrates that the uncertainty in an AERI measurement is on the order of .004 and .007 $\left(\frac{mW}{m^2\ sr\ cm^{-1}}\right)$ for apodized and unapodized spectra respectively. It should be noted that the reduction in error by a factor of approximately 1.7 between apodized and unapodized spectra does not correspond to an increase in the signal by 1.7. This is due to the apodizing process which slightly degrades the amount of signal in a measurement.

3.3.5 Error Simulation Final Results

Presented in Figure 3.12 are the results from all the different error simulations. These include the error simulations due to the temperature and WVMR profiles, modeled spectra from kCARTA, and measured spectra from AERI. The simulation study on the AERI retrieved temperature and WVMR profiles contains 3x13735 sets of profiles. The three sets correspond to:

1. **Base State** ($F_{base}^{mxn}(\nu)$): 13735 spectra produced from the AERI retrieved temperature and WVMR profiles input to kCARTA.

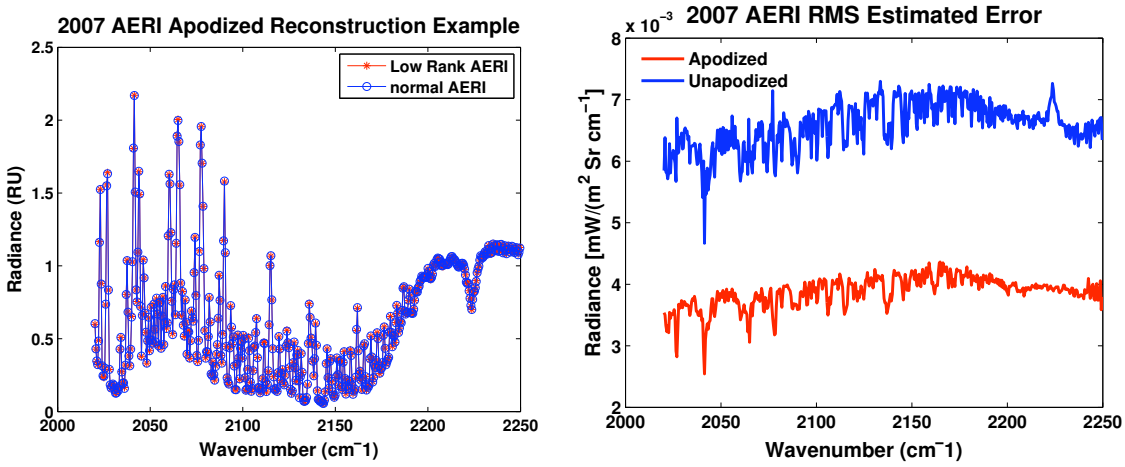

(a) (b)

Figure 3.11: (a) Reconstruction example of apodized AERI spectra (b) RMS error from the difference between the original AERI (L_{mxn}) and the reconstructed datasets (L_{mxn}^{low}).

2. **TEMP** ($F_{temp}^{mxn}(\nu)$): 13735 spectra produced by kCARTA using the perturbed AERI retrieved temperature from section 3.3.1 and normal WVMR profiles.

3. **WVMR** ($F_{h2o}^{mxn}(\nu)$): 13735 spectra produced by kCARTA using the perturbed AERI retrieved WVMR from section 3.3.2 and normal temperature profiles. The perturbed profiles were not fixed by simulated PWV measurements.

In the series of matrices relating to the input profiles, m corresponds to the 13735 profiles and n corresponds to the approximately 180 spectral channels that were modeled in the CO band with each kCARTA simulation. Uncertainty in kCARTA spectra due to errors in temperature and WVMR profiles is calculated as the RMS between the perturbed profile ($F_{temp}^{mxn}(\nu)$ or $F_{h2o}^{mxn}(\nu)$) and the base profile ($F_{base}^{mxn}(\nu)$).

The calculation is shown in equation 3.21 and 3.22

$$\epsilon_{temp}(\nu) = \sqrt[2]{\frac{1}{m}\sum_{i=1}^{m}[F^{ixn}_{temp}(\nu) - F^{ixn}_{base}(\nu)]^2} \tag{3.21}$$

$$\epsilon_{wvmr}(\nu) = \sqrt[2]{\frac{1}{m}\sum_{i=1}^{m}[F^{ixn}_{h2o}(\nu) - F^{ixn}_{base}(\nu)]^2} \tag{3.22}$$

Figure 3.12 shows the results of all error simuations conducted. All modeled terms (Water,Self,Foreign,CO) are added in quadrature (Equation 3.12) and represented as the "modeled" term in Figure 3.12. The results show that in relation to uncertainty from modeled parameters and input profiles, instrumental uncertainty from AERI is an order of magnitude less. Uncertainty due to the input profiles is smaller compared with uncertainty from modeling; however, they do make significant contributions in the spectral region from 2165 - 2190 cm^{-1} where most of the retrieval points (Green Dots) reside.

3.4 Direct Comparison: AERI vs kCARTA

This section shows the results from a direct comparison between synthetic spectra from kCARTA and measured spectra from AERI. Different variations of kCARTA (versions 114 and 115), continuum models (CKD 2.4 and MTCKD 1.0), and cloud flagging techniques (none, BT, and NN) are used to create synthetic spectra in order to compare with measured spectra from AERI. In combinations listed above, synthetic spectra from kCARTA is found to be biased low. Therefore, another set of comparisons is made with the bias removed from kCARTA synthetic

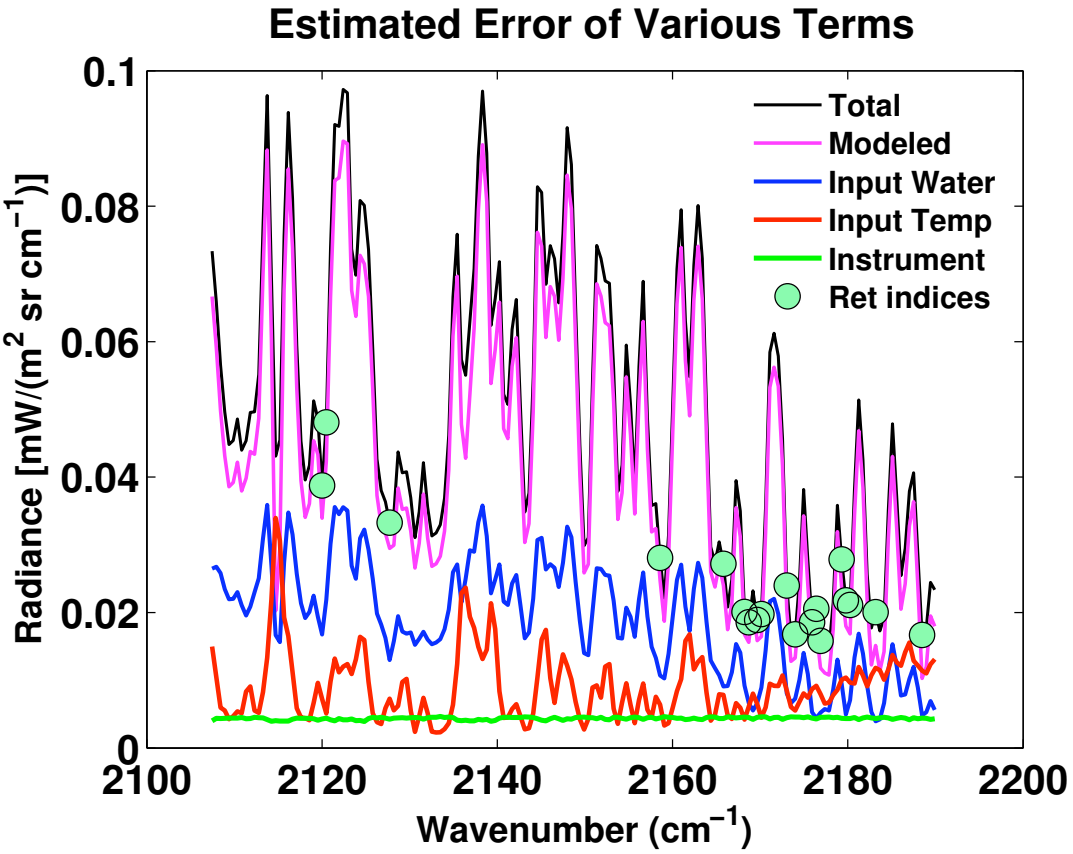

Figure 3.12: Estimated error terms used to constrain the CO retrieval. *Modeled* represents all error terms estimated from kCARTA modeling added in quadrature. *Input temp* and *Input Water* are the estimated error terms that are created from the large random number simulation involving propagation of validated error in the Feltz data set. *Instrument* displays the instrument error resulting from PCA performed on the 2007 apodized AERI data set. *Ret Indices* are channels used in the retrieval.

spectra. There are a total of 48 different combinations used to model spectra for this comparison study.

The 57 true composite CO profiles [90] measured from 2007 and 2008 are used as input to kCARTA. The flight of the aircraft which measures part of the CO profile takes roughly one hour to complete. A Feltz data set that matches up with the center of this time period is an input to kCARTA as well. Output of kCARTA is compared with AERI spectra matching up with the same time period as the Feltz data set.

Synthetic spectra are biased low for every combination used in this study. Figures 3.13(a), 3.13(b), and 3.13(c) show the bias (red) and standard deviation (blue) for non cloud filtered, BT cloud filtered, and NN cloud filtered respectively. kCARTA version 115 and continuum model MTCKD 1.0 are used to model synthetic spectra for these cases.

The bias is calculated in Equation 3.23 using $L_{mxn}(\nu)$ to describe the m number of AERI measurements with n spectral channels, and F_{mxn} to describe the m number of kCARTA measurements with n spectral channels. The non cloud filtered data set uses all 57 ($m = 57$) coincident measurements of AERI measured spectra and synthetic spectra from kCARTA using true composite CO as input. Fifty-four ($m = 54$) of the 57 coincident measurements are left once BT cloud filtering is performed. Twenty eight ($m = 28$) of the 57 coincident measurements are left after NN cloud filtering is performed.

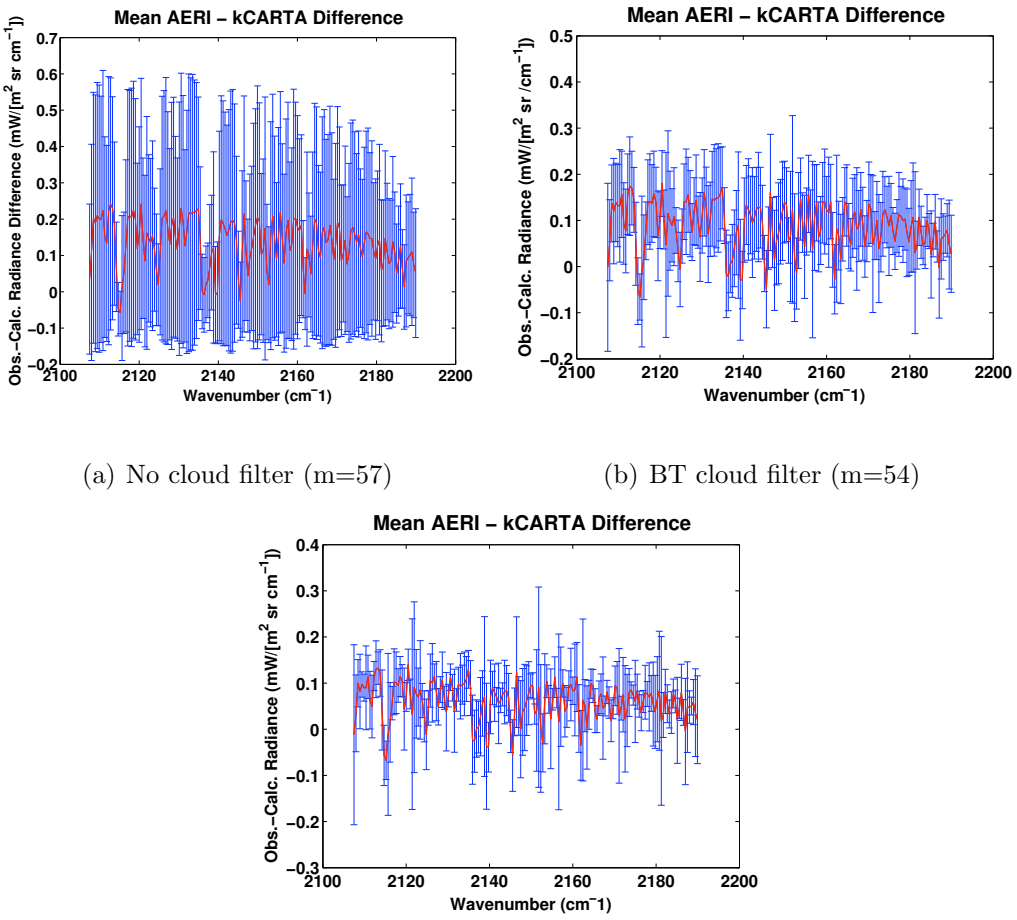

(a) No cloud filter (m=57)

(b) BT cloud filter (m=54)

(c) NN cloud filter (m=28)

Figure 3.13: (a) Bias and standard deviation measured for all 57 profiles. (b) Bias and standard deviation measured for 54 profiles filtered by BT contrast method. (c) Bias and standard deviation measured for 28 profiles filtered by the NN.

$$B(\nu) = \frac{1}{m} \sum_{i}^{m} L_{ixn}(\nu) - F_{ixn}(\nu) \tag{3.23}$$

With each combination of kCARTA version, continuum model, and MWR usage, a bias spectrum is calculated relating to non cloud filtered, BT cloud filtered, and NN cloud filtered. The process of adding the bias spectrum to kCARTA spectra is called centering.

The simulation study showed that error in AERI is more than an order magnitude lower than error in kCARTA. Thus AERI is considered as truth when its compared to kCARTA spectra. A spectral score, which is the mean standard deviation of AERI spectra minus kCARTA spectra, is used to assess the accuracy of kCARTA modeled spectra. The spectral score has the same units as radiance $\left(\frac{mW}{m^2\ sr\ cm^{-1}}\right)$.

Table 3.3 displays the results of testing all different combinations of modeling spectra. Moving left to right across the table shows the standard deviation reducing dramatically compared with moving top to bottom. This demonstrates that the most critical component to accurate forward modeling is cloud filtering. Using brightness temperature contrast or neural network cloud filters reduces noise by 2.5 and 3.5 times respectively when compared to simulations where no cloud filtering took place. Cloud filtering with the NN reduces the uncertainty between spectra from AERI and kCARTA by 45 - 50% when compared to BT cloud filtered data. This is for simulations where spectra from kCARTA is centered. Using the new cloud filter assures that true variability of the difference between AERI and kCARTA is

Name Combination	No cloud clearing		BT Cloud Clear		NN Cloud Clear	
	raw	centered	raw	BT centered	raw	NN centered
KC114 ckd24 noMWR	.2537	.2428	.0956	.0766	.0692	.0422
KC114 mtckd1 noMWR	.2540	.2430	.0957	.0768	.0691	.0422
KC115 ckd24 noMWR	.2537	.2429	.0956	.0767	.0691	.0424
KC115 mtckd1 noMWR	.2540	.2431	.0957	.0769	.0690	.0423
KC114 ckd24 MWR	.2556	.2463	.0888	.0702	.0652	.0365
KC114 mtckd1 MWR	.2556	.2463	.0890	.0704	.0651	.0365
KC115 ckd24 MWR	.2556	.2464	.0888	.0704	.0652	.0368
KC115 mtckd1 MWR	.2558	.2466	.0890	.0707	.0651	.0368

Table 3.3: Mean standard deviation calculations $\left(\frac{mW}{m^2\ sr\ cm^{-1}}\right)$ between AERI and kCARTA simulations for different models, cloud clearing, and MWR input. For each combination of kCARTA version, continuum model, MWR input, and cloud filter, the bias is calculated and added to the simulated kCARTA spectra. Spectral score calculations for these kCARTA simulations represent the centered column.

captured and effects from clouds are removed.

Centering the observations shows the second largest effect on reducing error. Adding the bias spectrum increases the accuracy by 5, 23 and 64 percent to non cloud filtered, BT cloud filtered and NN cloud filtered data respectively. The largest effect is clearly from the thick clouds. A histogram of unfiltered brightness temperature differences is shown in Figure 3.14. Two days with large error are evident with a mean absolute brightness temperature error of 22 and 26 Kelvin respectively. This is the cause of the large uncertainty between AERI and kCARTA measurements shown in columns 1 and 2 of Table 3.3.

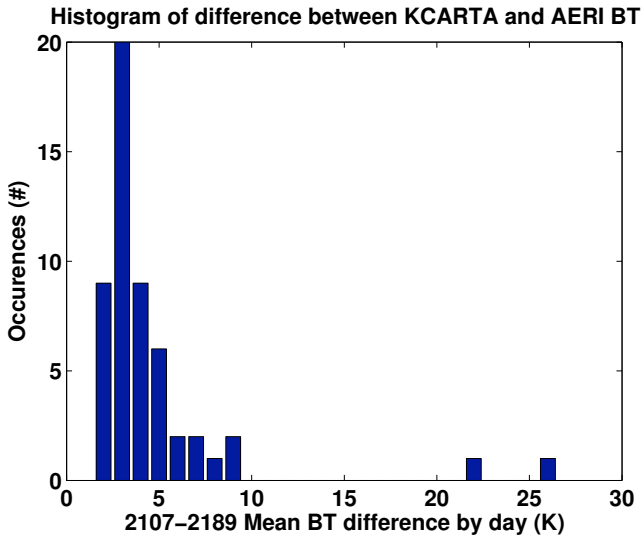

Figure 3.14: Histograms of the mean absolute brightness temperature difference between 2107 - 2189 cm^{-1}. No cloud filtering is performed and synthetic observations were created using kCARTA version 115, mtckd1, and no constraints from the MWR.

Inclusion of MWR data to constrain input profiles of water vapor proved to have the third largest effect. Table 3.3 is color coded to emphasize trials that used

or not did not use the MWR to constrain input water vapor profiles. The unfiltered data, represented by the trial with no cloud filtering, actually got slightly worse with the inclusion of MWR data. The possible reason is from the MWR sensing the water in the cloud.

Using the MWR from a day with thick clouds may increase the WVMR profile too much. For both BT filtered and NN filtered techniques the spectral score improved by 6 percent under non-centered simulations. Including MWR data into simulations where the BT or NN cloud flags improved the spectral score by 10 and 13% respectively. Comparing similar trials with different kCARTA versions or continuum models in Table 3.3 showed no significant difference, as typical changes in the spectral score was on the order of .1%.

Figure 3.15(a) is the seasonal variation of MWR measurements for this data set and shows the typical temporal variation where more humidity exists during the summertime and the atmosphere is drier during wintertime. Figures 3.15(b) - 3.15(d) display time series for the mean difference between AERI measurements and synthetic spectra from kCARTA. Each of these figures show the same seasonal variation as shown with MWR measurements in Figure 3.15(a). The affect of constraining the WVMR profile by MWR data is seen by comparing results using non constrained profiles in Figure 3.15(b) and constrained profiles in Figure 3.15(c). Using the MWR data reduces some of the variation, but does not remove the seasonality of the error. If the dominant source of error was due to uncertainty in water vapor profiles, using the MWR would have removed the seasonal variation; however, each figure has a seasonal variation quite similar to total precipitable water vapor

measured by the MWR. Figure 3.15(d) shows that when synthetic spectra from kCARTA is not fixed, kCARTA spectra is still biased low even for the coldest and driest parts of the year.

3.5 Error Analysis Conclusions

Its been shown that using the NN cloud filter reduces the uncertainty between AERI and kCARTA spectra by 45 - 50% compared to using the BT cloud filter. This is a result of the NN cloud filter catching 40% more of the cloudy scenes than the BT cloud filter. Even a thin cloud in the AERI FOV will reduce the off line on line spectral contrast between CO lines and is one cause for why the version 1 CO retrieval has a systematic low bias.

The simulation study shows that uncertainty in modeling absorption lines of water is more than an order of magnitude larger than uncertainty from AERI, and 2 to 3 times larger than the uncertainty resulting from errors in Feltz profiles.

For the estimated uncertainty terms shown in the simulation study WVMR is not fixed by MWR data. The total uncertainty in the simulation study has a mean of .049 $\left(\frac{mW}{m^2\ sr\ cm^{-1}}\right)$. This value compares well to the .042 mean standard deviation $\left(\frac{mW}{m^2\ sr\ cm^{-1}}\right)$ for the direct comparison trials that are setup using centered kCARTA spectra, NN filtered measurements , and non MWR fixed WVMR profiles. The similarity between the simulation and direct comparison demonstrates that the simulation study includes all the significant error terms.

Direct comparisons of spectra from AERI and kCARTA still exhibited a bias

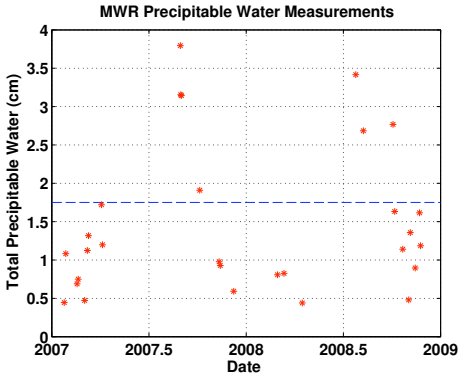

(a) MWR 2 year seasonal cycle

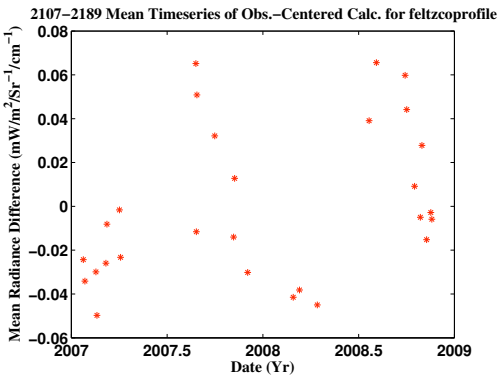

(b) Centered

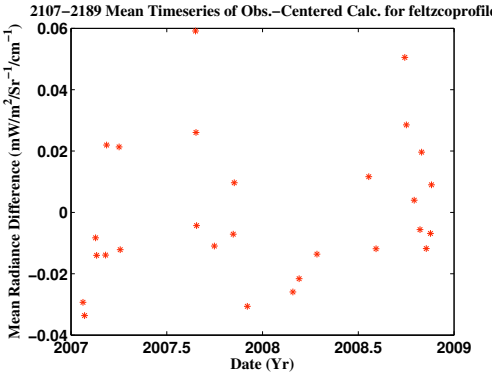

(c) Centered and Constrained by MWR

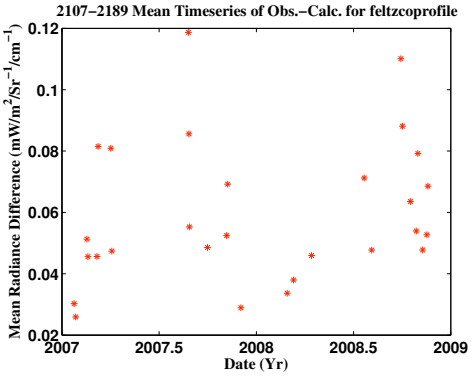

(d) Constrained by MWR

Figure 3.15: (a) Seasonal variation of MWR collocated with the CO measurements. (b) - (d) represent time series of mean difference between spectra from AERI and kCARTA for the spectral region 2107 - 2189 cm^{-1}. The model combinations are: (b) Centered and not constrained by MWR (c) Centered and constrained by MWR (d) Non centered and constrained by MWR. All cases are computed using kCARTA version 115, MT_CKD 1, true composite CO profiles, and were not cloudy as determined by the NN cloud flags. (b) and (c) are centered by adding the the bias corresponding to NN filtered data.

once the effect of clouds are effectively removed by the NN cloud flag. Centering spectra removes the bias contribution and shows improvements of 40% and 45% for non MWR fixed and MWR fixed trial respectively. This suggests that a small portion of the bias comes from WMR profiles. As demonstrated in [82], modeling absorption by water is complex and causes systematic errors. This type of bias will scale with the amount of water in the atmosphere. Time series of mean radiance error in the CO band shows the same seasonality as the amount of water in the atmosphere. This suggests that systematic errors in both continuum models (MT_CKD 1 and CKD 2.4) exist in the CO band. It's not entirely clear how this contributes to the systematic error on the version 1 CO retrieval.

All error terms estimated in this analysis are added together in quadrature to get a total error term. This assumes that each error term is independent of one another. The seasonality of radiance differences demonstrates the error due to modeling is correlated to the amount of water in the atmosphere. It has not been determined whether retrieved WVMR profiles from AERI has a systematic bias that is correlated with the amount of water in the atmosphere; however, it is known that vertical limitations in the AERI WVMR retrieval limit its ability to resolve large gradients of WVMR in the atmosphere [90]. If both types of error scale with the amount of water in the atmosphere then they certainly are not independent of one another; however, the quadrature addition seems reasonable from this study as error simulation and direct calculation of error are within 15%, with some of the difference likely due to the un-estimated error in the true composite profiles themselves.

This error analysis is beneficial for the use of any ground based sensor measur-

ing in the CO band with weighting functions peaking near the surface. Comparing this type of sensor to kCARTA or any radiative transfer algorithm which is based on HITRAN and some form of the CKD continuum model will be effected by the problems of modeling water.

Chapter 4

SAAC Retrieval Setup

This chapter gives all the necessary details to understand how to setup the stand alone AERI CO retrieval (SAAC). This includes a description of the retrieval grid that is a reduced representation of the RTP CO grid. The linearity of the radiative transfer equation as a function of change in CO is examined. The construction of two covariance matrices that contain the statistical descriptions of uncertainty in the spectral measurements and variations in the CO profile is demonstrated. These covariance matrices are used in two different retrieval equations that make different assumptions about the linearity of the radiative transfer equation.

A novel channel selection method is presented that makes use of the Shannon information content to determine the optimal channels to use in the retrieval. This new channel selection method accounts for the off-diagonal correlation in the error covariance matrix. Information content of the retrieval system is examined through calculating the degrees of freedom (d_s) and averaging kernels (A) for the different retrieval grids and retrieval equations. Finally, the two types of first guess profiles used, that provide the starting point for SAAC retrievals are presented.

4.1 Retrieval Grid

Results from this dissertation show that spectra from AERI contain little vertical information about the distribution of CO in the atmosphere. Therefore, retrieval grids are created that are reduced representations of the RTP grids defined in 2.5.2. The reduced RTP representation for CO is calculated on grids with 1-5 layers (excluding 4) where CO is defined on each layer by an average column density. A retrieval for column density CO is chosen because this representation is used as input to kCARTA. Errors by converting back and forth between column density and *ppbv* are then avoided and Jacobians are easily calculated using column density.

The new layering scheme is made up of super layers that are created by summing up the CO column densities (x) located in the RTP profiles. The calculation for this is shown in Equation 4.1, where t corresponds to the first RTP layer in the new super layer L, and N corresponds to the last RTP layer in the new super layer L. In Equation 4.1, $z(L)$ is a $Px1$ vector, where P is the total number of super layers in the retrieval grid, and L is a range of values from $1 \rightarrow P$.

$$z(L) = \sum_{i=t}^{N} x(i) \tag{4.1}$$

In order to speed up the calculation of $z(L)$, matrix multiplication is used from a summing matrix W. W is an $Px101$ matrix made up of 1^s and 0^s, where the 1^s and 0^s in L^{th} row of W corresponds to values of $x(i)$ summed to produce $z(L)$. If $x(t)$ is included in $z(L)$, then $W_{L,t} = 1$, otherwise $W_{L,t} = 0$. The matrix equation that calculates the average CO column density in the retrieval grid is displayed below:

$$z = Wx \tag{4.2}$$

Heights and effective pressures of each layer vary from one RTP profile to another RTP profile. Therefore, every combination consisting of the 56 RTP profiles and retrieval grid contains its' own summing matrix (W). The standard heights for each representation, shown in Table 4.1, are picked such that the mean of each retrieval grid CO profile contains roughly the same amount of CO molecules in each layer. This is done to avoid large changes in CO from small retrieved percentage changes. This situation occurs when one layer contains many more CO molecules than the other layers.

5 layer	0 - 1365	1365 - 3210	3210 - 5630	5630 - 9100	9100 - TOA
3 layer	0 - 1500	1500 - 5500	5500 - TOA		
2 layer	0 - 4000	4000 - TOA			
1 layer	0 - TOA				

Table 4.1: Height Boundaries for the different retrieval grids in meters. TOA means top of atmosphere as defined in each RTP profile.

A total of 4 different retrieval grids are tested in this dissertation. The first is a total column measurement where the super layer is the summation of an entire RTP profile. Next, 3 retrieval grids are used that contained 2, 3 and 5 super layers. A visualization of the retrieval grids and their corresponding super layers are shown in Figures 4.1(a), 4.1(b), and 4.1(c) respectively.

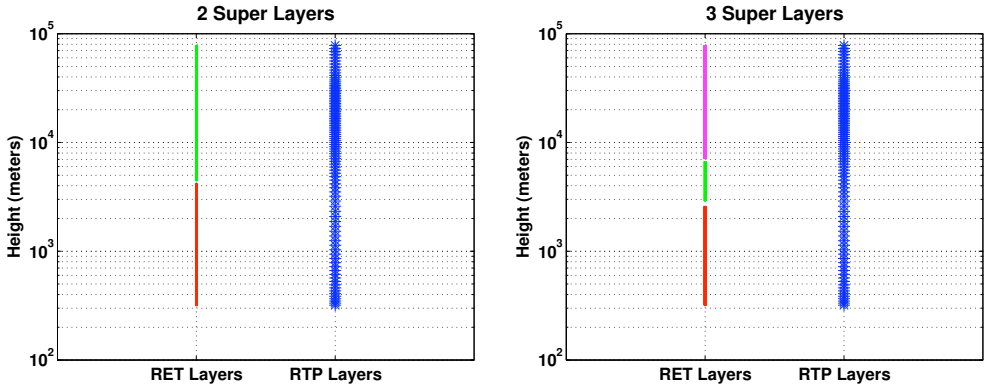

(a)

(b)

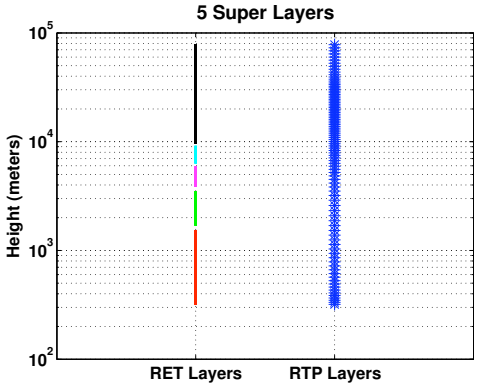

(c)

Figure 4.1: (a) Two layer retrieval grid used for the retrieval of CO. (b) Three layer retrieval grid used for the retrieval of CO. (c) Five retrieval layer grid used for the retrieval of CO. In each figure blue stars represent the RTP profiles read by kCARTA. The colored lines represent the super layers described above.

4.1.1 CO Layer Linear Dependence

Two examples of retrieval problems for the least square solution are shown in section 2.9.3. The rows of the Jacobian in the first example are close to being linearly dependent on each other. Consequently, the gain matrix amplified the noise be a few orders of magnitude and solutions from the retrieval were very poor. A second example was shown where rows of the Jacobian were linearly independent resulting in the affect from noise to be much smaller compared to the first example.

Examination of Figure 4.2 shows that Jacobians from different layers in the atmosphere have the same shape, but are just different scaled versions of each other. This indicates that Jacobians for CO are close to being linearly dependent and are highly affected by measurement noise. In this case, measurement noise is the result of differences between AERI spectra and kCARTA spectra when the best estimate of the atmospheric state is used as input profiles.

4.1.2 *a priori Variance*

The *a priori* covariance matrix (S_a) describes the variance and covariance of the state variable. *a priori* covariance matrices are built using the 56 true composite profiles. The 56 true composite CO profiles are converted to the merged profiles and input to KLAYERS which create 56 RTP profiles (x). Equation 4.2 is used to convert each profile to the retrieval grid representation for 1 ,2, 3 and 5 layers respectively. *a priori* CO profiles are calculated for all retrieval grid representations and are defined as the mean profile ($z_a = \frac{1}{N}\sum_{1}^{N} z_i$, where $N = 56$). The *a priori* CO profile is used

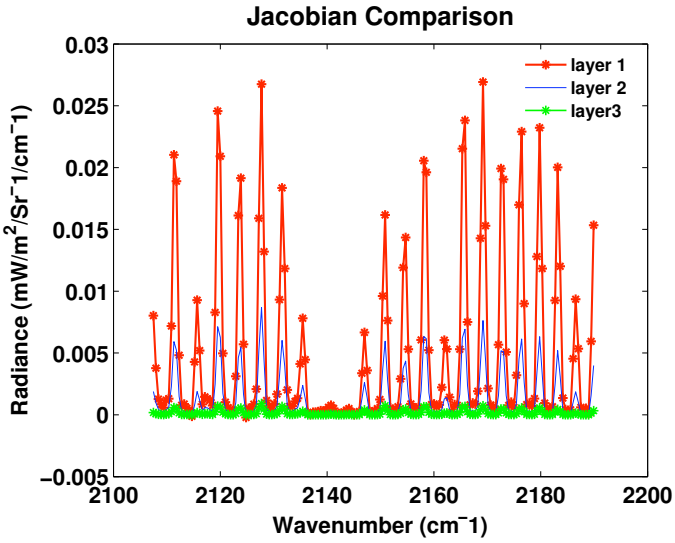

Figure 4.2: A three layer Jacobian comparison. This three layer Jacobian corresponds to the 3 layer scheme shown in Figure 4.1(b). Each Jacobian is calculated by perturbing the CO in the RTP layers encapsulated in the super layer by 10%.

in Equation 4.3 to calculate the covariance for a retrieval grid with P super layers.

$$S_a(P) = \frac{1}{N-1} \sum_{i}^{N} \left(\frac{z_i - z_a}{z_a} \right) \left(\frac{z_i - z_a}{z_a} \right)^T \tag{4.3}$$

Each CO profile on the retrieval grid (z) is a $Px1$ vector therefore, S_a is an PxP covariance matrix, where each element is weighted by the mean state. The diagonal of this matrix is the squared percent variation of the *a priori* state (σ_a^2). Tables 4.2, 4.3, and 4.4 display the percent variation ($x100$ to change from decimal to percent) and the *a priori* measurement of CO for each retrieval grid scheme.

A layer is defined by its top (p_{top}) and bottom (p_{bottom}) pressures. The defini-

p_{eff} (mb)	912	760	587	399	29
σ_a (%)	19.4	18.5	20.1	20.6	10.3
z_a ($\frac{\#\ mol.\ x10^{17}}{cm^2}$)	4.15	4.19	4.18	4.18	4.05
Height (m)	1365	3210	5630	9100	TOA

Table 4.2: 5 Layer *a priori*: Note that the *a priori* is on the order of 10^{17}. p_{eff} is the mean p_{eff} for all 57 retrieval grids in a 5 layer scheme.

tion of the effective pressure for a layer is shown below:

$$p_{eff}(L) = \frac{p_{bottom} - p_{top}}{ln\left(\frac{p_{bottom}}{p_{top}}\right)} \tag{4.4}$$

p_{eff} (mb)	856	581	41
σ_a (%)	18.1	19.9	13.3
z_a ($\frac{\#\ mol.\ x10^{17}}{cm^2}$)	6.88	6.88	6.96
Height (m)	1500	5500	TOA

Table 4.3: 3 Layer *a priori*: Note that the *a priori* is on the order of 10^{17}. p_{eff} is the mean p_{eff} for all 57 retrieval grids in a 5 layer scheme.

The single layer has a $\sigma_a = 15.2\%$ and a mean of $z_a = 2.07^{18}$ ($\frac{\#\ mol.\ x10^{18}}{cm^2}$).

4.2 Linearity

Inverse methods which operate under linear assumptions are used to retrieve CO from measured atmospheric radiance, where the forward function (RTE) that

p_{eff} (mb)	785	55
σ_a (%)	18.4	14.8
z_a ($\frac{\#\ mol.\ x10^{18}}{cm^2}$)	0.99	1.08
Height (m)	4000	TOA

Table 4.4: 2 Layer *a priori*: Note that the *a priori* is on the order of 10^{18}. p_{eff} is the mean p_{eff} for all 57 retrieval grids in a 5 layer scheme.

governs the relationship between CO and radiance is non-linear. kCARTA approximates the non-linear forward function and therefore it must be understood over what range in CO is the forward function still linear. A qualitative set of definitions for linearity have been developed in [67] and are presented below:

- **Linear:** The forward model can assume the form $y = Kx$ and a solution can be reached without any knowledge of *a priori*. Few inverse problems are of this nature.

- **Nearly Linear:** The problem is non-linear, however a linearisation about some base state allows for adequate solutions.

- **Moderately non-linear:** Linearisation around a base state allows for error analysis, however the step size in reaching a solution results in unacceptable errors from the Jacobian.

- **Grossly non-linear:** Problems are non-linear in the range of errors.

Examples of linear, nearly linear, and moderately non-linear functions are all shown in Figure 4.3. For both the nearly linear and moderately non-linear case, a tangent

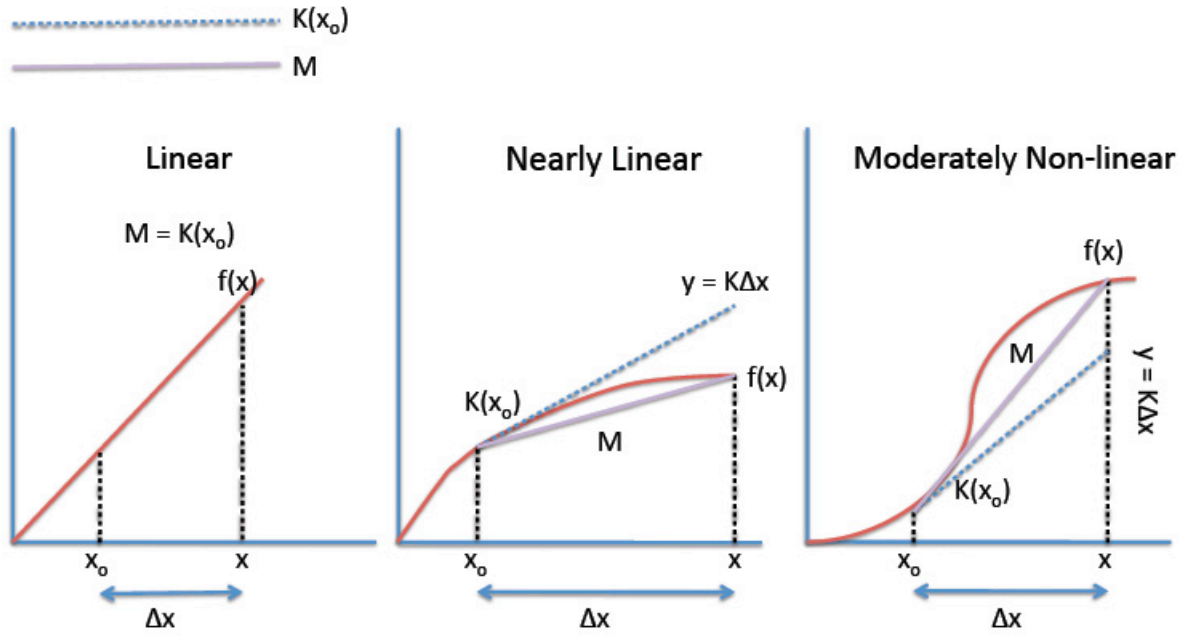

Figure 4.3: Examples of linear, nearly linear, and moderately non-linear functions. Also shown is how the Jacobian would calculate y for a given step size of Δx. The Jacobian is not shown for the linear case because it would be the same as $f(x)$.

line is drawn on the surface of the function $f(x)$. The slope of the tangent line represents K, and the dashed blue line connecting to $y = K\Delta x$ represents the approximation to $f(x)$ by using a linear assumption (In this scenario K represents the instantaneous derivative, which for radiative transfer is the analytic solution to the derivative of the RTE). The difference between y and $f(x)$ is the error due to this assumption.

A violet colored line labeled M is drawn from $f(x_o)$ to $f(x)$ in Figure 4.3. The slope of this line represents what the true linear approximation would be to correctly approximate $f(x)$. The calculation of this slope is shown in Equation 4.5.

$$M = \frac{F(x_o + \Delta x) - F(x_o)}{\Delta x} \tag{4.5}$$

For the linear case M equals K for any base state x_o and the exact solution can be attained from any assumption of a base state. In the nearly linear case, K's approximation to M improves as x_o is moved closer to x. In the moderately non-linear case, K does not necessarily improve by moving the base state x_o close to x.

The degree of linearity for the RTE is tested by examining the percent difference between the K and M for different sizes of Δx, where the difference of K from M is the error for a given step size in approximating the RTE as linear. For this linearity test the step size is measured as a percent change to part of an RTP profile for CO. The RTP profile for CO represents the base state x_n, where it is defined on n pressure layers. The relationship for the step size is seen in Equation 4.6.

$$\Delta x_n(\sigma_n) = \sigma_n x(p_n) \tag{4.6}$$

Equation 4.7 displays the calculation for M, where $F()$ represents a $mx1$ vector of synthetic spectra calculated by kCARTA.

$$M(\nu_m, \sigma_n) = \frac{F(x_n + \sigma_n x_n, \nu_m) - F(x_n, \nu_m)}{\sigma_n x_n(\sigma_n)} \tag{4.7}$$

This expression is identical to the expression for K shown in Equation 2.15; however, M is different from K in that M is calculated for many different values of σ_n. The

step size (σ_n) for K is small enough such that K can be approximated as the analytic solution to the instantaneous derivative. A step size of 1% ($\sigma_{n(L)} = .01$) is used to calculate K. This form is used because kCARTA at this time can not produce analytic Jacobians for super layers.

Percent difference is calculated as a percent change to CO in a layer. The calculation takes absolute difference between K and M and averages it over 172 channel indices that range from 2107 - 2190 cm^{-1}. The exact calculation is shown in Equation 4.8. The factor of 100 changes the decimal error to percent error. The spectrum representing the base state $F(x_o)$ is calculated using profiles of temperature, water, and carbon monoxide from May 20, 2007. CO step sizes range from 1-40% ($\sigma_n : .01 \rightarrow .40$). This calculation is done for two layers.

$$\textit{Percent Error } (\sigma_n) = \frac{100}{N} \sum_{i=1}^{N} \left| \frac{M(\nu_m, \sigma_n) - K(\nu_m)}{K(\nu_m)} \right| \tag{4.8}$$

Figure 4.4 displays the results from the linearity test described above. It is immediately obvious that the forward model, kCARTA, is not linear for any given change in CO. If it were, the percent difference would be zero, or at least not increase with positive changes in CO.

Results from Section 4.1.2 show that for any layer the percent variation is 20%. This results in a 1 and 2% error for the Jacobians in layers 1 and 2 respectively. On first inspection, this may not seem significant, however the measurement error from chapter 3 was around 1%. As layers are increased higher in the atmosphere, the error from this approximation increases. Therefore, the step sizes in CO for retrievals are constrained to 15%. Because the percent variation is larger than the step size, 2 or

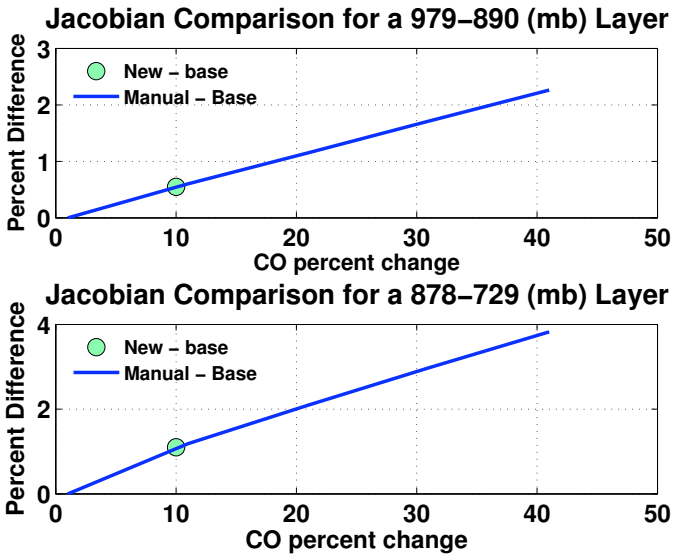

Figure 4.4: Two level linearity analysis. Each figure represents the percent difference between using a linear approximation (K) and true linear relationship (M) for a given step size in CO (Δx_n). The top graph is the result from perturbing the first 23 layers in the RTP CO profile (979-890mb). The bottom graph is the result from perturbing the layers with pressures between 878 and 729 mb in the RTP CO profile. In the Legend, "$New-base$" represents the 10% perturbation that is used to calculate kCARTA Jacobians. "$Manual - Base$" represents the percent uncertainty calculation from Equation 4.8

3 iterations will be needed to reach a reasonable solution. This classifies the forward modeling process somewhere between non-linear and moderately non-linear. In each case the error analysis is linear [67] and the forward model is linearized by expanding it about an *a priori* value shown in Equation 4.9

$$y - F(x_o) \approx \frac{\partial F}{\partial x}(x - x_o)$$
$$\Delta y \approx K \Delta x \tag{4.9}$$

4.3 Retrieval Equations

The previous section classified the forward problem as nearly linear or moderately non-linear (MNL). Therefore, two forms of retrieval equations are used to measure CO. The first form is derived under the nearly linear assumption and allowed to iterate to a solution. A second solution is derived that assumes that the forward model is moderately non-linear.

4.3.1 Nearly Linear Solution (LSQ)

A solution to the nearly linear problem is presented first. Equation 4.9 displayed that the final form of the nearly linear case is $\Delta y = K \Delta x$. While deriving the retrieval equation the Δ will be dropped for the simplicity of writing and the final solution will be adjusted accordingly in the end. The cost function for the nearly linear forward problem is defined in Equation 4.10, where the error covariance matrix (S_e) is included to reduce the effect of uncertainty between AERI and kCARTA

spectra, and $x^T Hx$ is a constraint matrix which adds information to the null space of the measurement.

$$J_{NL} = (Kx - y)^T S_e^{-1}(Kx - y) + x^T Hx \tag{4.10}$$

As seen in Equation 4.11, the nearly linear cost function (J_{NL}) looks quite similar to the linear case once the terms in the cost function are multiplied out. The inclusion of terms S_e^{-1} and $x^T Hx$ is the difference between the nearly linear case and the linear case.

$$J_{NL} = x^T K^T S_e^{-1} Kx - y^T S_e^{-1} Kx - x^T K^T S_e^{-1} y + x^T Hx \tag{4.11}$$

Next, the value of x is found that minimizes J_{NL}. This is done by setting $\frac{\partial J_{NL}}{\partial x} = 0$ and solving for $\hat{x}$. Because it is necessary to take derivatives of matrices, the derivative relation from [67, A.6] is used again to evaluate the derivative of J_{NL}. This relation is presented below:

$$\frac{\partial}{\partial x}[x^T Ax + \gamma^2 b^T x] = A^T x + Ax + \gamma^2 b$$

Terms $x^T Hx$ and $x^T K^T S_e^{-1} Kx$ are combined to $x^T(K^T S_e^{-1} K + H)x$ and is substituted into $x^T Ax$, where $A = K^T S_e^{-1} K + H$. Next, $y^T S_e^{-1} K$ is substituted for b^T. After making the substitutions above the derivative of J_{NL} with respect to x is displayed in Equation 4.12.

$$\frac{\partial J_{NL}}{\partial x} = 2(K^T S_e^{-1} K\hat{x} + H\hat{x} - K^T S_e^{-1} y) = 0 \tag{4.12}$$

Next, solving Equation 4.12 for $\hat{x}$ yields the relationship shown in Equation 4.13.

$$\hat{x} = (K^T S_e^{-1} K + H)^{-1} K^T S_e^{-1} y \tag{4.13}$$

Substitutions from the Taylor expansion ($\hat{x} = \Delta x$) and ($y = \Delta y$) are put back in for $\hat{x}$ and y. The Taylor expansion in Equation 4.9 showed that $\Delta x = x - x_o$ and $\Delta y = y - F(x_o)$. After these substitutions are made, the solution is written in Equation 4.14. In Equation 4.14 the terms $\hat{x}_i$ and $\hat{x}_{i+1}$ are used in place of x_o and x respectively. These forms are used because the retrieval equation here is allowed to iterate to the solution; however, at iteration 1 the x_i equals the base state (First Guess) CO profile.

$$\hat{x}_{i+1} = \hat{x}_i + (K^T S_e^{-1} K + H)^{-1} K^T [y - F(x_i)] \tag{4.14}$$

Two final steps must be made to assure that the inverse in Equation 4.14 can be evaluated with Matlab, and that changes to the state vector are in the linear regime ($\approx 20\%$).

First, the retrieval equation is reformed so that percentage changes to x_i are retrieved. This change is needed because column density Jacobians from kCARTA are in units of $\frac{Radiance}{Kilomole}$ and have a magnitude on the order of 1E8. The retrieved quantity, $\hat{x}$, has units of $\frac{molecules}{cm^2}$ and has typical values from 1E16 to 1E18 depending on the size for a retrieval layer. Computational roundoff error made the inverse not usable when retrieving the absolute change in column density for CO.

To change the retrieval equation to measure percent changes a substitution is made in Equation 4.14 such that $\tilde{\mathrm{K}} = x_i K$. This is not a matrix multiplication; rather, each layer's Jacobian is multiplied by the corresponding layer's partial column density in x_i. This scaling changes the Jacobian and the retrieval equation from raw change in column density to a percentage change.

The substitution process begins with Equation 4.15 where the term x_i is multiplied and divided throughout the equation so the retrieval equation is reformed rather than changed.

$$x_{i+1} = x_i + (\frac{x_i}{x_i} K^T S_e^{-1} K \frac{x_i}{x_i} + \frac{x_i^2}{x_i^2} H)^{-1} K^T \frac{x_i}{x_i} S_e^{-1} [y - F(x_i)] \tag{4.15}$$

Next, the substitution of $\tilde{\mathrm{K}} = x_i K$ is shown in Equation 4.16.

$$x_{i+1} = x_i + (\frac{1}{x_i^2} \tilde{K}^T S_e^{-1} \tilde{K} + \frac{x_i^2}{x_i^2} H)^{-1} \tilde{K}^T \frac{1}{x_i} S_e^{-1} [y - F(x_i)] \tag{4.16}$$

The term $(\frac{1}{x_i^2} \tilde{K}^T S_e^{-1} \tilde{K} + \frac{x_i^2}{x_i^2} H)^{-1}$ is equivalent to $x_i^2 (\tilde{K}^T S_e^{-1} \tilde{K} + x_i^2 H)^{-1}$, thus Equation 4.16 is reformed and written out in Equation 4.17

$$x_{i+1} = x_i + x_i (\tilde{K}^T S_e^{-1} \tilde{K} + x_i^2 H)^{-1} \tilde{K}^T S_e^{-1} [y - F(x_i)] \tag{4.17}$$

The next step is done to assure that changes to x_i are not more than 20%. An *ad hoc* term is factored through Equation 4.17 that has 100 values between 0.01 and 1. This term (a) is factored through Equation 4.17 in the same way that x_i was above and results in 100 retrieval results for x_{i+1}. Equation 4.18 displays the retrieval equation once a is factored through it.

$$x_{i+1} = x_i + a^2 x_i (\tilde{K}^T S_e^{-1} \tilde{K} + \frac{x_i^2}{a^2} H)^{-1} (a \tilde{K}^T) S_e^{-1} [y - F(x_i)] \tag{4.18}$$

Both terms in the right hand side of Equation 4.18 contain the term x_i. This can be factored out, and the final form of the retrieval is shown below:

$$x_{i+1} = (1 + \alpha) x_i \tag{4.19}$$

where,

$$\alpha = a^2 (\tilde{K}^T S_e^{-1} \tilde{K} + \frac{x_i^2}{a^2} H)^{-1} (a \tilde{K}^T) S_e^{-1} [y - F(x_i)]$$

For each iteration i, Equation 4.19 has 100 solutions corresponding to the 100 values of a. The α created with the largest value while not being greater than a linear step size is chosen to update x_i. It should be pointed out that at iteration $i+1$ in the retrieval the Jacobian is recalculated with x_i as its base point. **LSQ** is a shorthand reference used in the rest of the dissertation to reference the solution to the nearly linear problem in equation 4.19.

4.3.2 Moderately non-linear (LSQwAP)

One more solution is developed for the moderately non-linear problem. The moderately non-linear problem starts with the equation $y = F(x) + \epsilon$. The cost function for the moderately non-linear (MNL) problem is displayed below:

$$J_{MNL} = (y - F(x))^T S_e^{-1}(y - F(x)) + (x - x_a)^T H(x - x_a) \tag{4.20}$$

The value of x which minimizes J_{MNL} is presented in Equation 4.21.

$$\hat{x}_{i+1} = x_a + (K_i^T S_e^{-1} K_i + H)^{-1} K_i^T S_e^{-1}[y - F(x_i) + K_i(x_i - x_a)] \tag{4.21}$$

Details for deriving this solution are found in [67, 5.3]. In deriving this solution [67, 5.3] states that $\nabla_x K^T$ is sufficiently small and can be ignored for moderately non-linear problems. The $\nabla_x K^T$ term is a vector that represents the second derivative of the forward model. Each value in this vector is a matrix. Once this term is ignored, Gauss-Newton iteration methods are used to solve the non-linear least square problem.

Just as in Section 4.3.1 the substitutions $\tilde{\mathrm{K}} = x_i K$, and the factor a are put into the retrieval equation. The retrieval equation with these substitutions made is

shown in Equation 4.22:

$$\hat{x}_{i+1} = x_a + a^2 x_i (\tilde{K}_i^T S_e^{-1} \tilde{K}_i + \frac{x_i^2}{a^2} H)^{-1} (a\tilde{K}_i^T) S_e^{-1} [y - F(x_i) + a\tilde{K}_i (1 - \frac{x_a}{x_i})] \quad (4.22)$$

The relationship representing the percentage change update to the previous iteration is in Equation 4.23.

$$\hat{x}_{i+1} = x_a + \alpha x_i \quad (4.23)$$

where, $\alpha = a^2 (\tilde{K}_i^T S_e^{-1} \tilde{K}_i + \frac{x_i^2}{a^2} H)^{-1} (a\tilde{K}_i^T) S_e^{-1} [y - F(x_i) + a\tilde{K}_i (1 - \frac{x_a}{x_i})]$

To ensure that changes are in the linear regime one final reorganization of the previous equation is made

$$x_{i+1} = \beta x_i \quad (4.24)$$

where, $\beta = (\frac{x_a}{x_i} + \alpha)$

The difference between the retrieval equation for the nearly linear problem in Section 4.3.1 and the retrieval equations shown here is inclusion of the first guess term x_a. This means that the solution here is constrained to the *a priori* CO profile, where the size of the constraint is determined by H. **LSQwAP** is used as a reference to solution of the moderately non-linear problem in equation 4.24.

4.3.3 Constraint Matrix (H_{TT})

The proper form of the constraint matrix H from both retrieval equations (LSQ and LSQwAP) is found by analyzing the *maximum a posteriori* (MAP) solution from [67]. This solution is found using Bayes theorem and is the expected value $\overline{x}$ from a Gaussian distribution of states governed by its conditional probability P($\mathbf{x}$|$\mathbf{y}$). The

solution, taken from [67, Ch.2], is shown below in Equation 4.25.

$$\hat{x} = x_a + \left[K^T S_e^{-1} K + S_a^{-1}\right]^{-1} K^T S_e^{-1}(y - Kx_a) \tag{4.25}$$

The solution for $\hat{x}$ shown below is quite similar to the one derived by maximizing a cost function seen in Equation 4.14. The solution in Equation 4.25 is constrained by the inverse of the *apriori* covariance S_a^{-1}. Parts of the state x which vary little from their expected value $\overline{x}$ have a small variance. Smaller percent variations will greater constrain Equation 4.25 to the first guess. This constraint adds information to the null space of the measurement [40].

Equation 4.18 showed that an *ad hoc* constraint matrix H is used in the formal solution. This is chosen over the *a priori* covariance matrix because there is not enough true CO profiles to capture the true atmospheric variability in CO. This is demonstrated by calculations of the weighted covariance matrix which showed layer to layer correlations as high as 80%.

Factoring x_i out of Equation 4.25 produces a constraint term $x_i^2 S_a^{-1}$ that is very similar to the term $x_i^2 H$, which is found in the LSQ and LSQwAP retrieval equations. This redefines the units in the *a priori* covariance from $\Delta\ \frac{Molecules}{cm^2}$ to the square of percent variation (σ_a^2). Therefore, the *apriori* percent variations (σ_a) from Tables 4.2, 4.3 and 4.4 are used to build the constraint matrix. For each retrieval grid defined on P layers, a diagonal constraint matrix (H_{TT}) is created. The calculation for the diagonal of H_{TT} is shown in Equation 4.26, where $\sigma_a(L)$ comes from the *a priori* percent variation from Tables 4.2, 4.3 or 4.4. For the single layer retrieval grid, H_{TT} is defined as σ_a for 1 layer.

$$H_{TT}(L,L) = \frac{1}{\sigma_a^2(L)} \tag{4.26}$$

4.4 Error Covariance Matrix

The total error covariance matrix (S_e) contains the variance and covariance of the spectral channels due to the uncertainty between the forward model kCARTA and AERI measurements. Each measurement technique has its own error covariance matrix (S_y for AERI and S_f for kCARTA) due to the uncertainty between its own measurement and the true atmospheric state y_{atm}. The relationship of the total error covariance matrix to the instrumental covariance matrix (S_y) and the model covariance matrix (S_f) is shown below:

$$S_e = S_y + S_f \tag{4.27}$$

The model covariance matrix (S_f) can be further broken down so that the total error covariance matrix is calculated with Equation 4.28.

$$S_e = S_{mod} + S_{h2o} + S_{temp} + S_y \tag{4.28}$$

where,

S_e = *refers to the total error covariance*

S_{mod} = *estimated from uncertainties in line parameters inside of kCARTA*

S_{h2o} = *estimated from uncertainties in WVMR profiles used as input to kCARTA*

S_{temp} = *estimated from uncertainties in temperature profiles used as input to kCARTA*

S_{AERI} = *estimated from uncertainties in measured spectra from AERI*

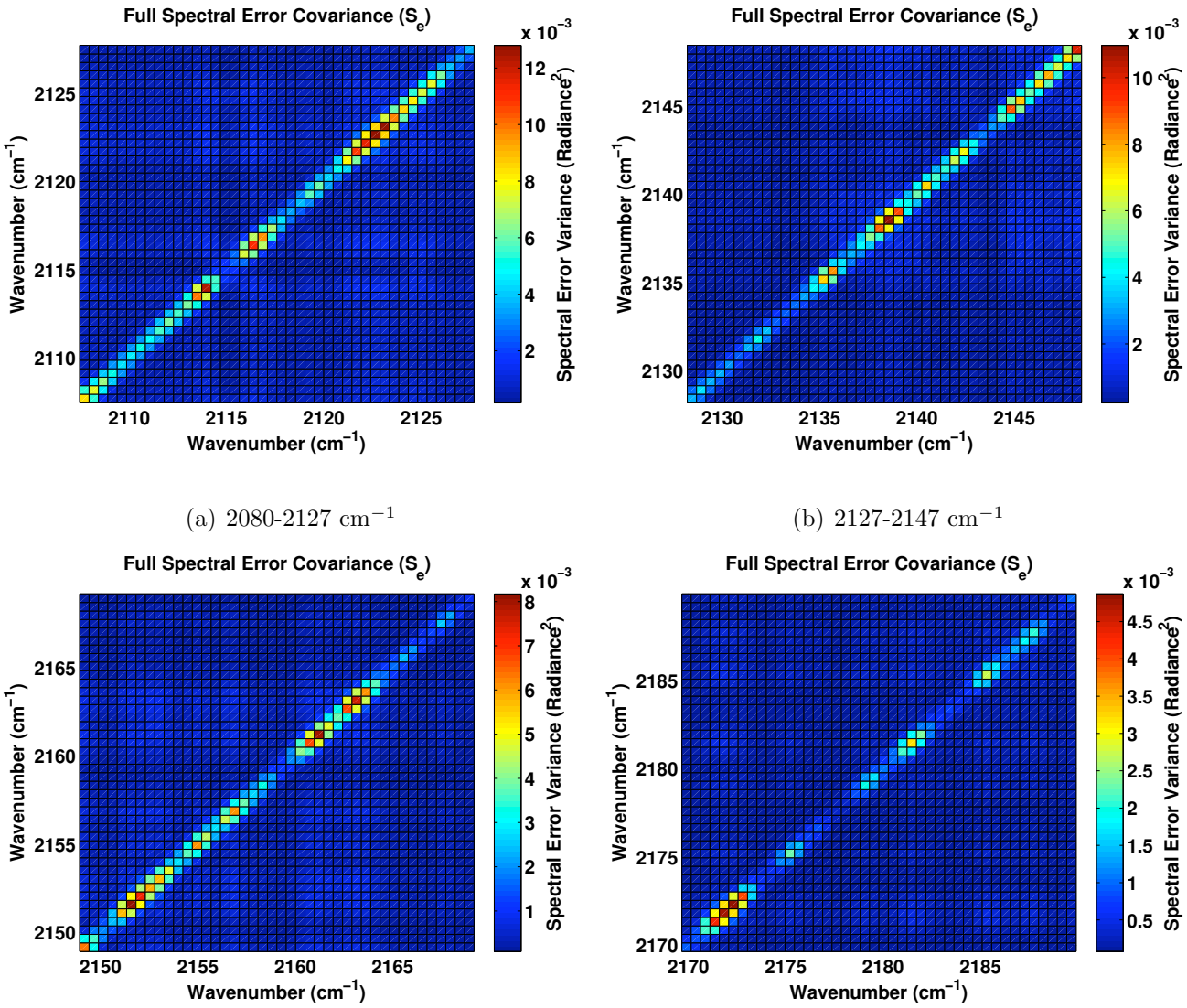

(a) 2080-2127 cm^{-1}

(b) 2127-2147 cm^{-1}

(c) 2147-2169 cm^{-1}

(d) 2169-2197 cm^{-1}

Figure 4.5: (a) - (d) represent the full error covariance (S_e) calculated using Equation 4.28. The full CO band from 2080 - 2197 (cm^{-1} is broken up into 4 spectral intervals.)

The total error covariance (S_e) is broken up into four subsections of the entire CO band and is shown in Figures 4.5(a) through 4.5(d).Correlation of off-diagonal terms goes to zero after the first few terms, thus S_e is a highly diagonal matrix and is easily invertible using standard computer programs.

4.4.1 Total Model Error Covariance (S_f)

Six different quantities contributing to the uncertainty in synthetic spectra from kCARTA are modeled. These six quantities are broken down into two separate groups:

1. **Inputs to kCARTA:** Temperature, WVMR, and carbon monoxide profiles are used as inputs to kCARTA. Simulated error is added onto 13735 temperature and WVMR retrievals from a year's worth of AERI data. A description of the simulation for temperature and water is covered in sections 3.3.2 and 3.3.1 respectively. The error covariances for temperature and water are termed S_{temp} and S_{h2o} respectively.

2. **Modeled Physics Uncertainties** Uncertainties in the absorption line parameters are given in Table 3.2 for water, CO, and the self and foreign broadening of water. These represent a lack in knowledge of the physics governing radiative transfer for this region. The combined error covariance from these terms is called S_{mod} for this dissertation.

4.4.1.1 kCARTA Input Covariance (S_{temp},S_{h2o})

Both error covariance matrices (S_{temp},S_{h2o}) due to the uncertainty in one of Feltz profiles (temperature or water) are calculated using Equation 4.29, where $\Delta F_b(\nu) = F_b(\nu, b + \Delta b) - F_{base}(\nu, b)$. $F_{base}(\nu, b)$ refers to the mxn base state matrix referenced in Section 3.3.5, and consists of $m = 13735$ kCARTA simulations. $F_b(\nu, b + \Delta b)$ refers to either one of mxn perturbed matrices (F_{temp}, F_{h2o}) from the same section relating to perturbations in temperature or WVMR. In Equation 4.29 T denotes the transpose of a matrix.

$$S_b(\nu) = \frac{1}{m-1} \Delta F_b^T \Delta F_b \tag{4.29}$$

Figures 4.6(a) through 4.6(d) show the results from simulating errors to the temperature profiles used by kCARTA and Figures 4.7(a) through 4.7(d) represent the results from the water simulation. Each set of subplots when put together represent the entire 172 channel error covariance matrix for each term. The error covariance for water has many significant off-diagonal terms indicating a strong correlation of uncertainty between channels. The Jacobians in Figure 3.4(a) show that water does not have many window channels, therefore an error to input water would offset the entire band to some degree. The temperature Jacobians shown in Figure 3.4(a) have more separation between absorption lines. Thus spectral error resulting from errors in the temperature profile is less correlated from channel to channel compared to the water; however, as seen in Figure 4.7(d), the R branch in the CO band does have strong off-diagonal terms for temperature indicating spectral error due to

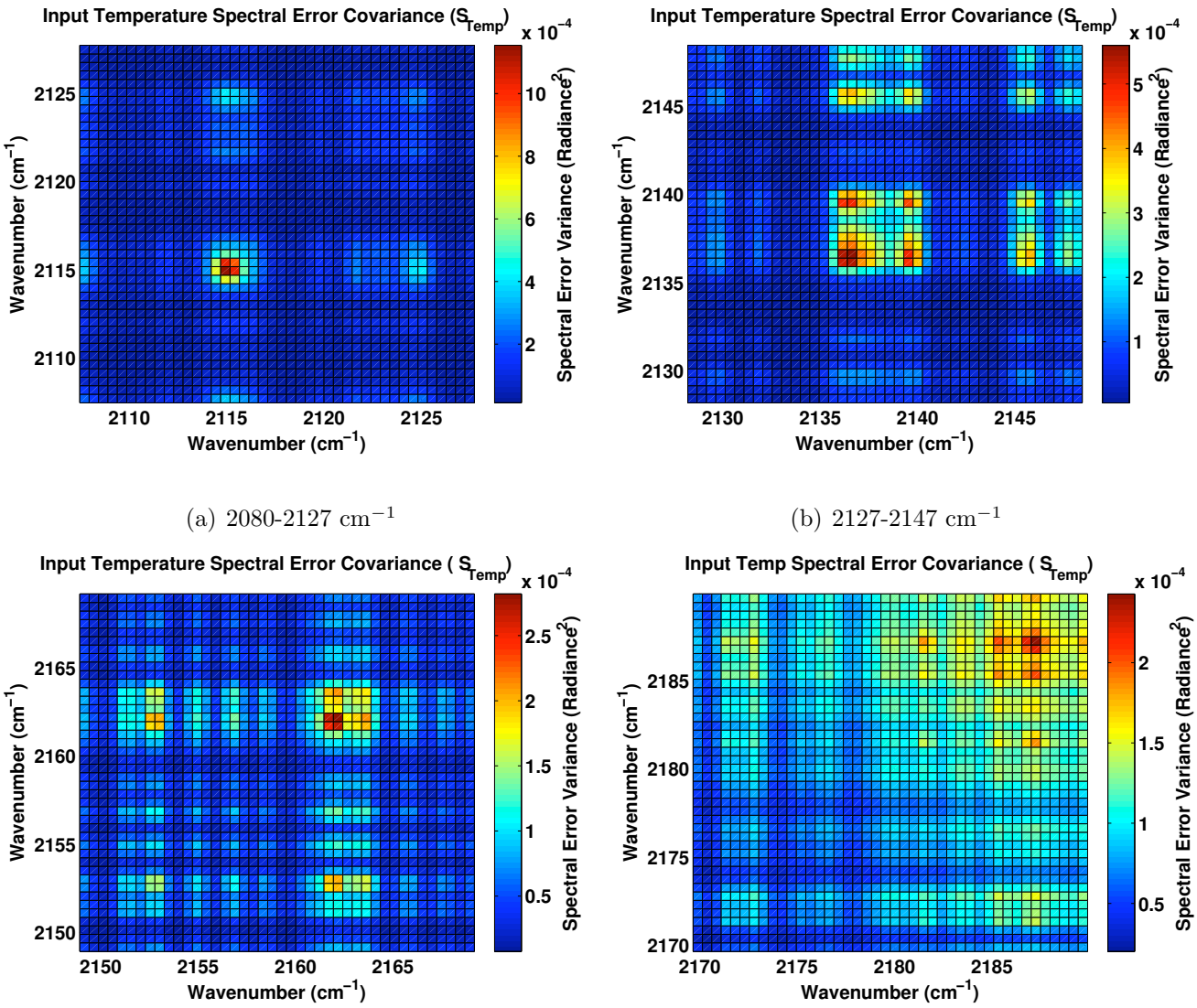

(a) 2080-2127 cm^{-1}

(b) 2127-2147 cm^{-1}

(c) 2147-2169 cm^{-1}

(d) 2169-2197 cm^{-1}

Figure 4.6: (a) through (d) represent the error covariance from uncertainties in temperature profiles used by kCARTA (S_{Temp}). The full CO band from 2080 - 2197 (cm^{-1} is broken up into four spectral intervals.)

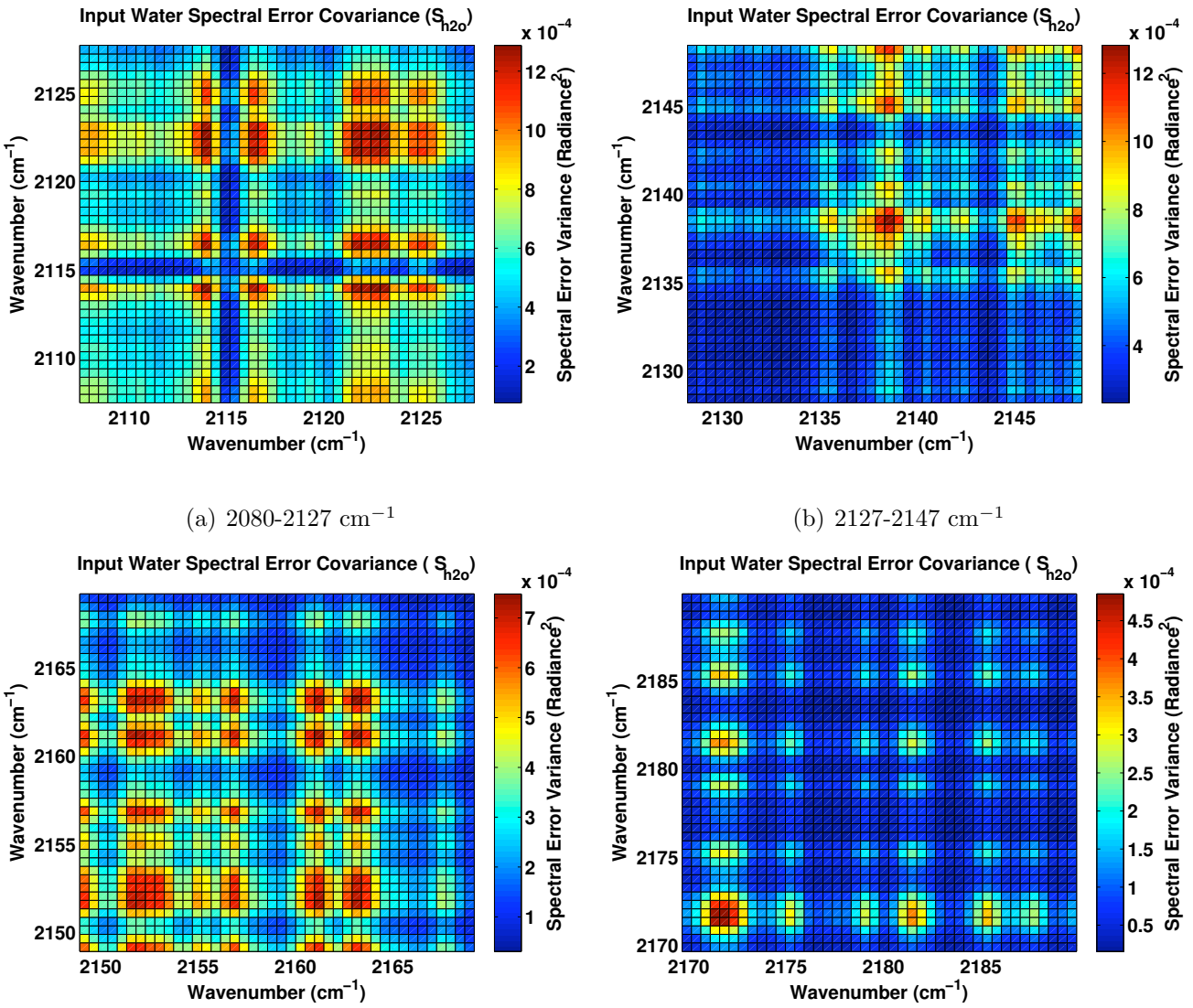

(a) 2080-2127 cm^{-1}

(b) 2127-2147 cm^{-1}

(c) 2147-2169 cm^{-1}

(d) 2169-2197 cm^{-1}

Figure 4.7: (a) through (d) represent the error covariance from uncertainties in water profiles used in kCARTA (S_{water}). The full CO band from 2080 - 2197 (cm^{-1} is broken up into four spectral intervals.)

uncertainty in temperature profiles is correlated.

4.4.1.2 kCARTA Model Covariance (S_{mod})

An error covariance matrix is calculated using Equation 4.30, where ϵ_{mod} is a $1xn$ error vector whose values are taken from the total modeled uncertainty values in Figure 3.8(b), and C is an nxn matrix of Beer apodization correlation coefficients displayed in Figure 4.8. The $\otimes$ is used to represent element by element multiplication between two matrices. The Beer correlation matrix, displayed in Figure 4.8, describes correlations between channels when spectra is Beer-apodized and is constructed using known correlation coefficients [39]. Beer correlation coefficients have significant correlation up to 3 channels away from the central channel.

$$S_{mod} = C \otimes \epsilon_{mod}(\nu)\epsilon_{mod}^{T}(\nu) \tag{4.30}$$

Large off-diagonal correlations are found when using the typical calculation of an

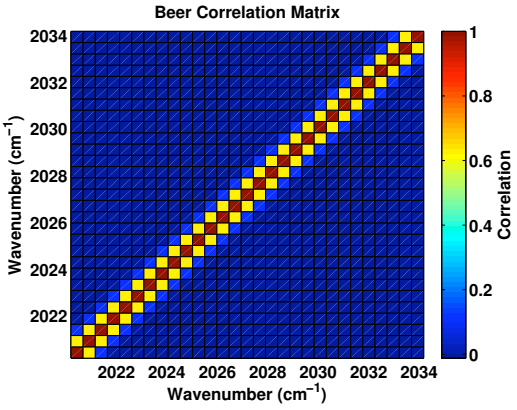

Figure 4.8: Displays the correlation among channels from a Beer apodization [39]

error covariance matrix for S_{mod} ($S_{mod} = \epsilon_{mod}\epsilon_{mod}^{T}$). Because S_{mod} makes the biggest contribution to S_e, it too had large off-diagonal correlation. This form of S_e is found

to not be invertible as is required by retrieval equations. Therefore, the *ad hoc* form of S_{mod} in Equation 4.30 is used because it preserves the covariance of the first few off-diagonal terms, while allowing S_e to be invertible.

Figures 4.9(a) through 4.9(d) show modeled covariance matrix (S_{mod}). This matrix is highly diagonal and easily inverted. Because this matrix dominates the contributions to the total error covariance matrix, it too is easily invertible.

4.4.2 AERI Error Covariance (S_y)

The instrumental error covariance for AERI is determined from the unapodized estimated uncertainty shown in Figure 3.11(b), and the theoretical correlation coefficients from Beer apodization. This *ad hoc* method is logical as the primary source of error in AERI measurements results from scene to scene variation in the black body stability of AERI and is likely to be random. Thus, the off-diagonal terms are a result of the Beer apodization of the random scene to scene blackbody error. The calculation of the AERI error covariance is displayed in Equation 4.31.

$$S_y = C \otimes \frac{\epsilon_{AERI}(\nu)\epsilon_{AERI}^T(\nu)}{NR} \tag{4.31}$$

where,

S_y = *AERI instrumental error covariance*

C = *Beer correlation matrix from Figure 4.8*

ϵ_{AERI} = *Unapodized uncertainty in AERI as shown in Figure 3.11(b)*

NR = *Theoretical noise reduction factor due to Beer apodization.* $NR = 1.568738$

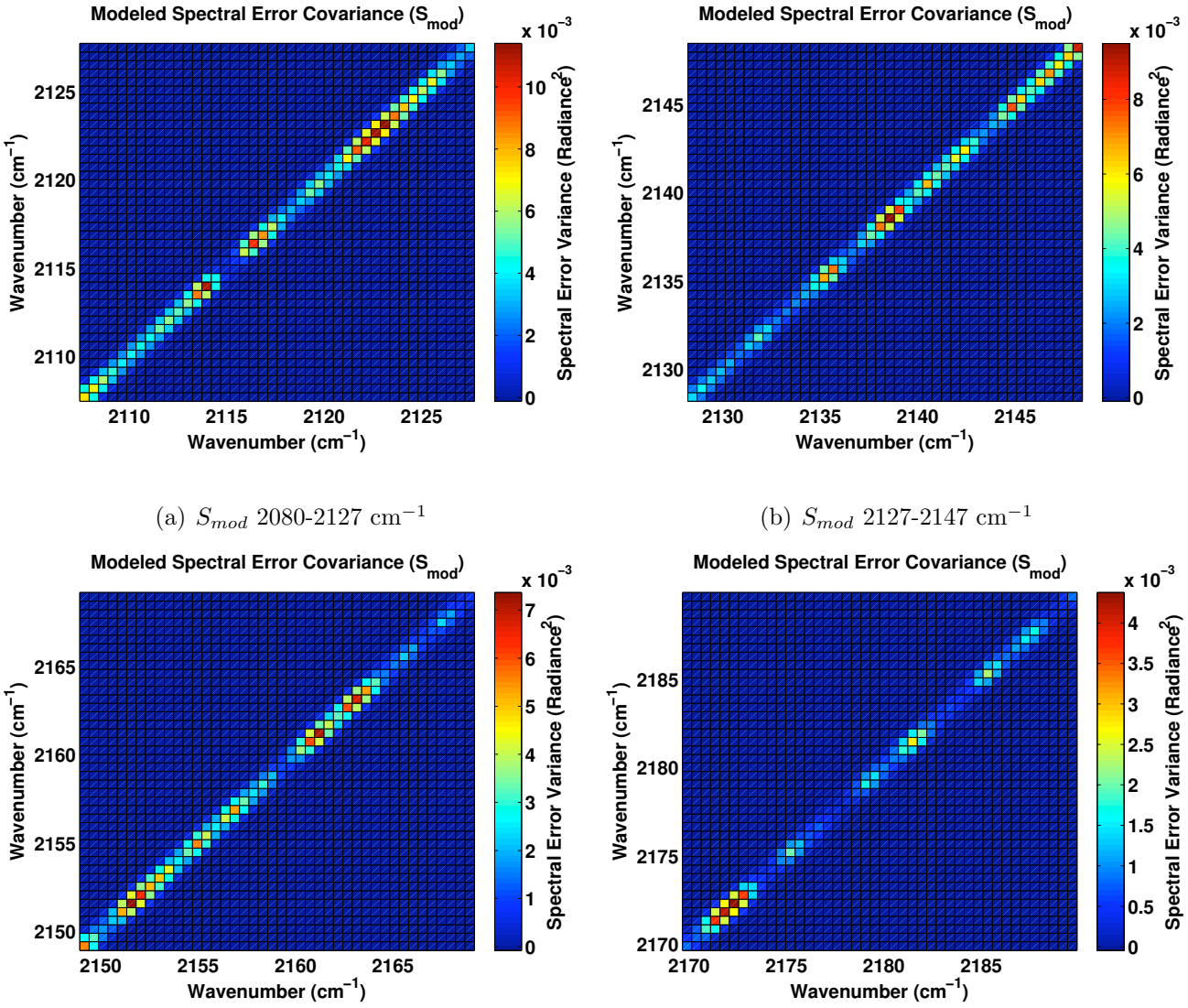

(a) S_{mod} 2080-2127 cm^{-1}

(b) S_{mod} 2127-2147 cm^{-1}

(c) S_{mod} 2147-2169 cm^{-1}

(d) S_{mod} 2169-2197 cm^{-1}

Figure 4.9: (a) through (d) represent the error covariance from uncertainties in absorption lines used by kCARTA to calculate synthetic spectra (S_{mod}). This is the total of all different modeling terms ($S_{modwater}, S_{self}, S_{foreign}, S_{CO}$). The full CO band from 2080 - 2197 (cm^{-1} is broken up into four spectral intervals.

4.5 Channel Selection

An iterative algorithm based on the Shannon information content of a retrieval system is created that determines what AERI channels to use in the SAAC retrieval. A similar iterative scheme for choosing channels in a measurement was first described by [18], where the information content of each individual channel is calculated. The iterative scheme begins by selecting the channel that adds the highest amount of information to the retrieval system, and then information content for each channel is recalculated. The process continues until some desired goal is reached, or no channels are left to sort through. Information content is described by the Shannon information content (H_S), or degrees of freedom (DOF).

The method from [18] works well for error covariance matrices that are purely diagonal indicating that the spectral error is not correlated. Unfortunately, the error covariance in the CO band has channel to channel correlation that is demonstrated by the off-diagonal terms in the error covariance plots from Section 4.4. A new iterative scheme is presented here which modifies the scheme from [18] to incorporate the channel to channel spectrally correlated error from the error covariance matrix, and then selects the appropriate channels for use in retrievals.

The process begins by first sorting the channels using a signal to noise term which is similar to the term $S_e^{-1/2} K S_a^{1/2}$. This term is described in [67, Ch. 2] as being comprised of singular values made from both signal and noise, whose values greater than one signify independent pieces of information. The signal to noise term used in this work is displayed below in Equation 4.32. This produces a symmetric

matrix where each diagonal element represents the square of a signal to noise term.

$$SN = \sqrt{trace\left[(S_e^{-1}K^T S_a)(S_e^{-1}K^T S_a)^T\right]} \tag{4.32}$$

Once the channels are sorted, the routine simulates what the Shannon information content of the retrieval system would be with a subset of channels. The full error covariance from Figures 4.5(a)-4.5(d) can be broken down into the individual uncertainties of from their channels (ϵ_i) and the correlation between them ($corr(l,j)$). This decomposition is shown in Equation 4.33 and represents an element representation of the new error covariance matrix. Each channel's uncertainty is calculated by taking the square root on the diagonal of S_e.

$$S_e(l,j) = \epsilon_l \epsilon_j corr(l,j) \tag{4.33}$$

At each iteration (i) a new channel is tested by building a new error covariance matrix (S_e), gain matrix (G_i), Jacobian matrix ($\tilde{K}_i$), and averaging kernel (A_i). Then the Shannon information content ($H_S(\nu_i)$) is calculated. The subset of channels determined from iteration ($i-1$) plus the new channel is used to select the appropriate rows in G_i and K_i which are mxn matrices. Each element in the new error covariance matrix is calculated using the product of uncertainty between the two channels times their correlation coefficient found from Equation 4.33. Iterative calculations for H_S, G_i, and A_i are shown below.

$$H_S(i) = -\frac{1}{2}\left|I_i - A_i\right| \tag{4.34}$$

$$G_i = (\tilde{K}_i^T S_i^{-1}\tilde{K} + H_{TT})^{-1}\tilde{K}^T S_i^{-1} \tag{4.35}$$

$$A_i = G_i \tilde{K}_i \tag{4.36}$$

Using these calculations the routine proceeds as listed below:

1. Calculate H_S for the channel with the highest signal to noise as defined by Equation 4.32.

2. Calculate $H_S(i = 1)$ for the channel with the next highest signal to noise. If H_S increase by 0.02 then include in set of channels used for the retrieval.

3. Repeat step 2 for all subsequent channels sorted by signal to noise.

Including a channel never decreases the knowledge about a state, therefore a small threshold was chosen to distinguish channels which added almost nothing. At iteration i, if the Shannon information content is not more than 0.02 greater than the previous iteration, then the channel is not included. Figure 4.10(a) shows the channel selection process and the increase in information as each channel is included. Figure 4.10(b) shows a plot of a Jacobian versus the spectral indices. The P branch contains many more water lines and therefore contains more uncertainty in the measurement. This method is effective in placing most of the spectral indices in the R branch where the influence of errors due to water is diminished.

This method identifies 19-21 channels which added the most information from the 172 channels in the CO band. Two and three layers have the 19 channel indices listed in Table 4.5, and the five layer retrieval grid has the same 19 channels plus channel indices 795 and 798. The channel indices along with the respective wavenumbers are displayed in Table 4.5. The similarity among the channels gives further indication that only one real piece of information exists in the retrieval system. Table 4.6 shows the DOF results from all 3 layering schemes. It is seen that

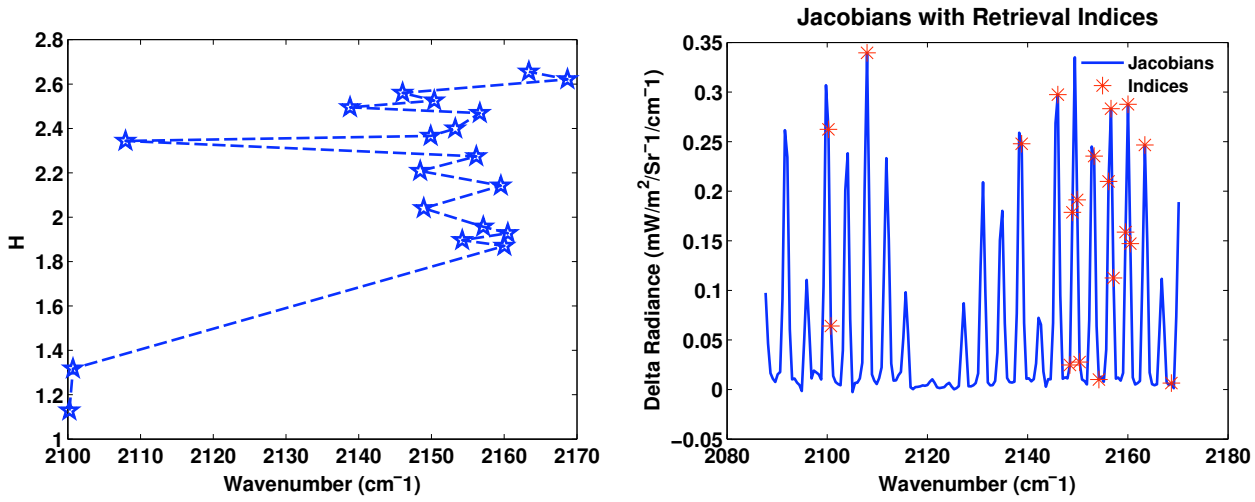

(a) (b)

Figure 4.10: (a) Plot of indices that increased H by more than 0.02. (b) The first layer Jacobian defined on the 2 layer retrieval grid. The retrieval indices used are plotted in red as well.

Channel	665	666	681	745	760	765	766	768
Wavenumber (cm^{-1})	2100.2	2100.7	2107.9	2138.8	2146.0	2148.4	2148.9	2149.9
Channel	769	775	777	781	782	783	789	790
Wavenumber (cm^{-1})	2150.4	2153.3	2154.2	2156.2	2157.1	2159.5	2160.0	2160.5
Channel	796	807						
Wavenumber (cm^{-1})	2163.4	2168.7						

Table 4.5: The channel indices and corresponding wavenumber from the AERI instrument used in the retrieval are shown. These are the base 19 channel indices that were common to all of the different layer and constraint schemes.

increasing the number of layers in the system adds little information.

2 Layer	1.02
3 Layer	1.06
5 Layer	1.07

Table 4.6: DOF are shown here for the different layering schemes using the H_{TT} constraint matrix.

4.5.1 Final Error Covariance Matrices

Figures 4.11(a) through 4.11(c) present the error covariance matrices for all forward model terms after the channel selection process from Section 4.5 is done. Uncertainty in water profiles and line parameters are the dominating terms, both having variances higher compared with the variance temperature; however, in the region near the last retrieval indices, variance from temperature and water are nearly the same. Comparing Figure 4.11(a) to Figure 4.11(d) reveals that the total error covariance is highly diagonal and mostly made up of contributions from the modeled error covariance.

Estimated error from uncertainty in absorption lines strongly resembles the WVMR Jacobian plots shown. Therefore, it is reasonable to assume that the model error covariance should strongly resemble WVMR input error covariance. A procedure using many trials, such as the method used to estimate uncertainty in the input profiles would improve the error estimate and result in the correct channel

to channel correlation coefficients; however, a highly diagonal error matrix is easily invertible and therefore quite useful in the retrieval equation.

The error covariance matrix shown in Figure 4.12 shows that the variance due to error from AERI is much smaller than the total error, and at its maximum is only comparable in size to the smallest variances seen in the input temperature error covariance matrix.

4.6 Information Content of the Retrieval

Figures 4.13(a)- 4.13(c) are averaging kernels described by the gain matrix from Equation 4.18 and calculated using the relationship for the averaging kernel ($A = GK$). These figures demonstrate that the CO retrieval is mostly sensitive to changes in parts of the atmosphere with pressures greater than 800 mb. Moreover, the averaging kernels from Figures 4.13(b) and 4.13(c) indicate that differences between true upper atmospheric CO and first guess upper atmospheric CO cause changes to the retrieved CO profile below 800 mb.

Figures 4.14(a)- 4.14(c) are the corresponding cumulative sum DOF for 2, 3 and 5 layer retrieval grids. These figures demonstrate that the majority of the information that AERI retrieves comes near the surface. Comparisons of the 3 and 5 layer schemes show that a slight amount of information is contained around 600 mb. Figures 4.14(a) - 4.14(c) have DOF's ranging from 0.72 - 0.81.

At maximum, the DOF of the retrieval system is 0.95. The requirement that retrieval updates are linear is the primary reason for the difference of the DOF

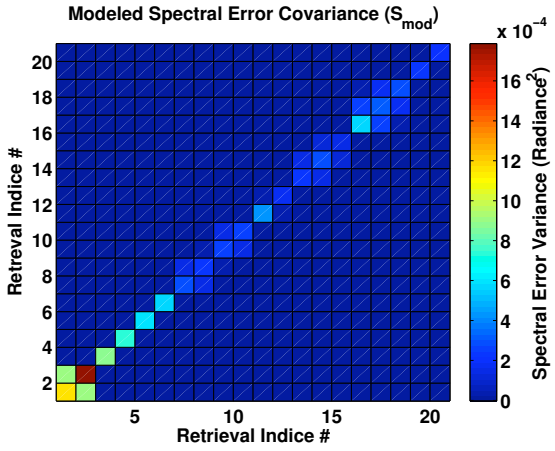

(a) Model Error

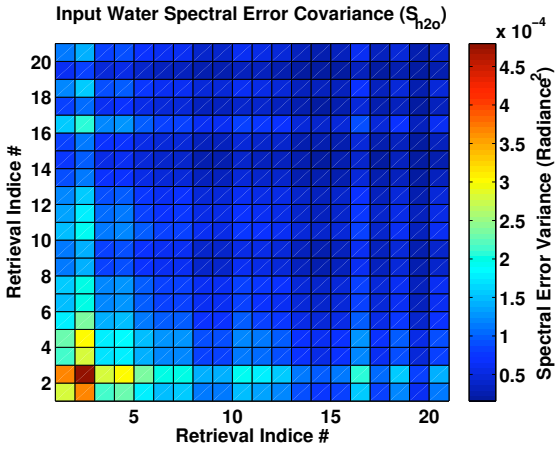

(b) WVMR Input Error

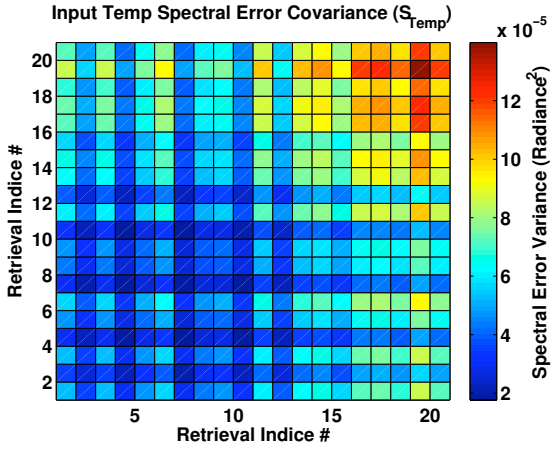

(c) Temperature Input Error

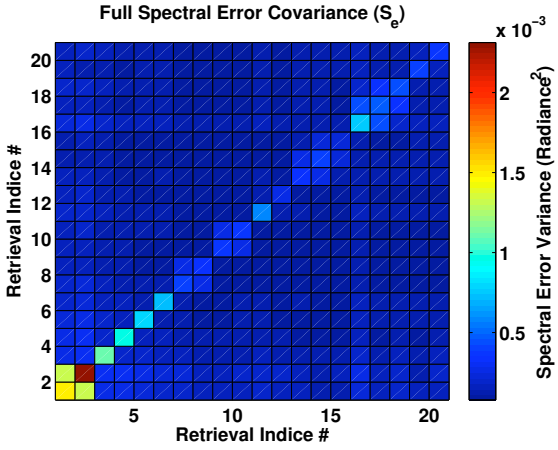

(d) Total Error

Figure 4.11: (a) through (d) show the covariance matrices for modeled kCARTA error, Input Water, Input Temperature, and total error respectively. Retrieval indice # correspond to the 21 channel indices listed in table 4.5. Retrieval indice # 1 starts with AERI channel index 665.

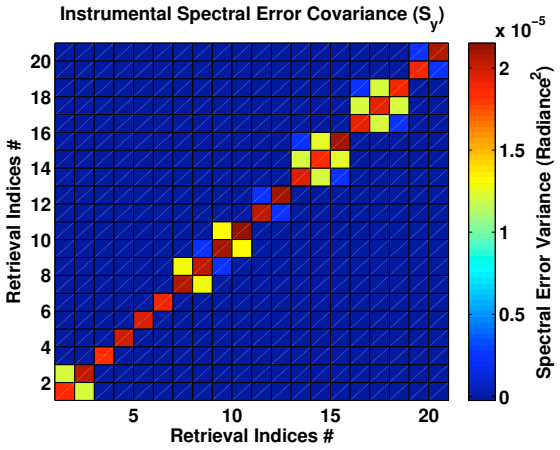

Figure 4.12: The estimated error covariance matrix (S_y) due to instrumental uncertainty.

between retrievals, and why DOF in retrievals are not at their maximum. When changes to x_i are outside the linear regime, that solution is disregarded, and a smaller change corresponding to a smaller linearity factor (a in Equations 4.19 or 4.24) is chosen. Consequently, the DOF for the retrieval are smaller then the maximum.

The original goal of this work was to create a product capable of monitoring boundary layer venting. In order to do boundary layer venting the vertical resolution needed is less than 1 km [16]. Because AERI CO measurements are sensitive to the first 2 - 3km, and contain around 1 piece of independent information, it is not possible to monitor boundary layer venting of CO.

4.7 Retrieval Update

Both retrieval equations presented in Section 4.3.2 calculate a percent change to CO column density distributed on retrieval grids made up of super layers. Mea-

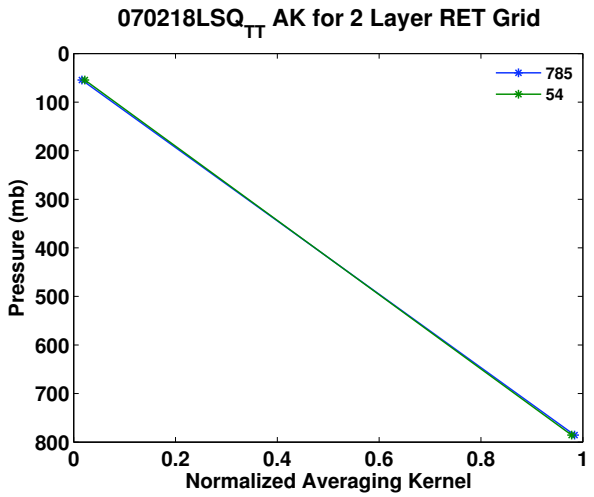

(a) 2 Layer Retrieval Grid

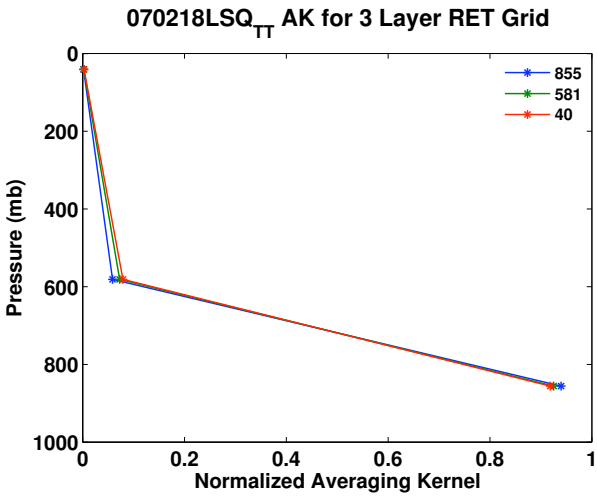

(b) 3 Layer Retrieval Grid

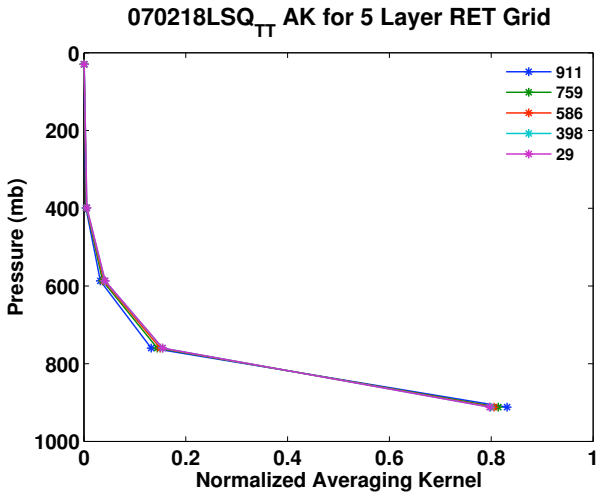

(c) 5 Layer Retrieval Grid

Figure 4.13: (a) 2 layer AK for 20070218. (b) A 3 layer AK for the same day. (c) A 5 layer scheme for the same day. All three averaging kernels are calculated using Equation 2.28.

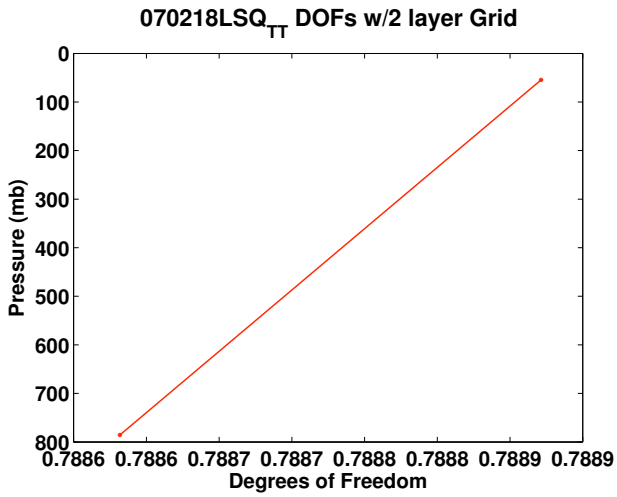

(a) 2 Layer Retrieval Grid

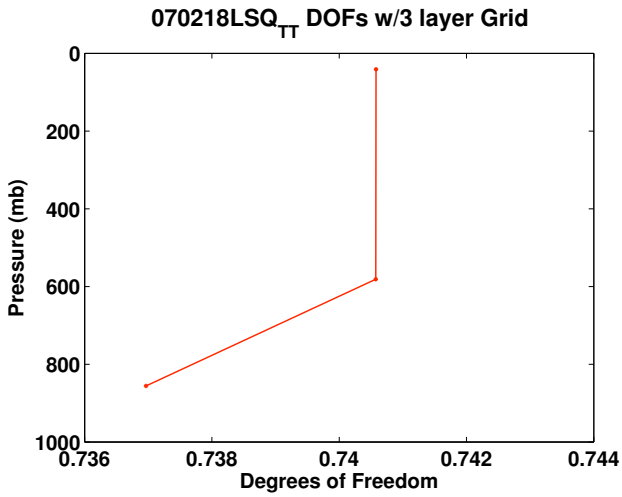

(b) 3 Layer Retrieval Grid

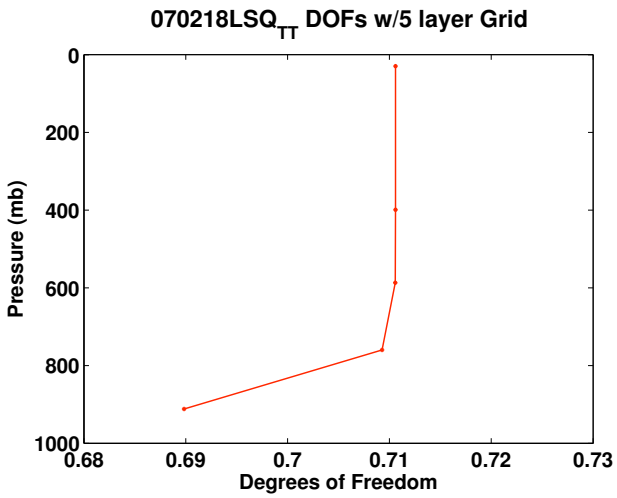

(c) 5 Layer Retrieval Grid

Figure 4.14: (a) 2 layer cumulative DOF for 20070218. (b) 3 layer cumulative DOF for 20070218. (c) Same as (a) and (b), except for 5 layers. Each cumulative sum is calculated along the diagonal of the corresponding averaging kernels shown in Figures 4.13(a)- 4.13(c).

sured percentage changes defined on 1, 2, 3 or 5 layers are linearly interpolated to the full RTP profile grid; specifically, CO values defined on the effective pressures corresponding to the super layers are linearly interpolated to the effective pressures of layers on the RTP profile grid. Retrieved CO values on the RTP grid are then correlated due to the linear interpolation.

Below is a summary of the two different equations used to update the RTP CO profile described in Section 4.3.2:

$$\begin{aligned} \textbf{Nearly Linear (LSQ)} x_{i+1} &= (1+\alpha)x_i \\ \textbf{Moderately Nonlinear (LSQwAP} \; x_{i+1} &= x_a + \alpha x_i = (\alpha + \frac{x_a}{x_i})x_i = \beta x_i \end{aligned}$$

A summary of the steps to update the RTP CO profile using the LSQ equation is provided below:

1. Percentage change (α) from iteration i to i+1 is determined from Equation 4.19 at either 1 ,2, 3 or 5 super layers.

2. The percentage change (α) is interpolated from the super layers to the full RTP grid using the effective pressures of each grid system.

3. x_{i+1} is updated using the relation for LSQ written above.

4. If the number of iterations is less than 4 and the RMS error among the spectral channels is more than .001 than the process is repeated.

Next, a summary of the steps used to update the RTP CO profile using the LSQwAP is presented below:

1. Percentage change (α) from iteration i to i+1 is determined from Equation 4.24 at either 1, 2, 3 or 5 super layers.

2. β is calculated from α, x_i, and x_a, and interpolated to the RTP grid.

3. x_{i+1} is updated using the relation for LSQwAP written above.

4. If the number of iterations is less than 4 and the RMS error among the spectral channels is less than .001, then the process is repeated.

4.7.1 First Guess profiles

The two first guess profiles used in this dissertation are AIRSv5 retrieved CO or an *a priori* profile defined as the mean of the 56 RTP profiles defined on one of the retrieval grids. Each first guess has small differences in how they are created for use in the retrieval.

- *a priori*: The mean of the merged CO profiles is used as the first guess profile input to KLAYERS. The output, an RTP CO profile from KLAYERS, is converted to the retrieval grid through the relationship $z(L) = Wx(n)$. The fractional difference between $z(L)$ and $z_a(L)$ is calculated as $\theta(L) = \frac{z_a}{z(L)}$. The next step takes $\theta(L)$ and linearly interpolates it to the RTP grid ($\theta(n)$). Finally, the *a priori* on the RTP grid is calculated as $x_a(n) = \theta(n) \otimes x(n)$. x_a is the RTP profile that is updated at the first iteration of the retrieval.

- *AIRS*: The profiles used from the AIRSv5 are gridded on 100 levels. Above 150 mb, the profile is chopped off and merged to a reference profile. This profile is

then converted to the merged profile representation and fed into KLAYERS. Finally, KLAYERS outputs the CO profile on the RTP grid. This CO profile is used as x_a in the retrieval equations as the first guess.

Chapter 5

SAAC Retrieval System

This chapter presents results from the SAAC retrieval system using the *a priori* profile (z_a) defined on 1, 2, 3 and 5 super layers. Results presented here meet the goal of modifying the existing AERI CO retrieval in order to better determine carbon monoxide distribution in the atmosphere.

57 true composite CO profiles over 2007 and 2008 are used here to determine the quality of the AERI CO retrieval system [90]. Table 5.1 list the 28 dates that correspond to each true composite CO profile case that have been determined to be cloud free by the neural network.

20070123	20070126	20070216	20070218	20070307	20070309
20070402	20070404	20070826	20070827	20070828	20071001
20071106	20071108	20071203	20080227	20080310	20080413
20080721	20080804	20080928	20081001	20081016	20081027
20081030	20081108	20081116	20081118		

Table 5.1: 28 dates corresponding to true composite CO profiles which were determined to be free of clouds by the NN cloud flag. Each date contained one measured true profile around local noon at the SGP site.

5.1 Spectral Tuning Effect (Centering)

The error analysis from Chapter 3 demonstrates that synthetic spectra from kCARTA is biased low when it is compared with measured AERI spectra. Two bias spectrums are created from the direct comparisons between AERI and kCARTA spectrums that remove bias for either the BT or NN cloud flagged data sets. As demonstrated in Chapter 3, the BT bias spectrum is larger across the CO band compared to the NN bias spectrum. This section presents the results from centering with BT or NN bias spectrums.

The single super layer retrieval grid is chosen to examine the effect of adding bias to synthetic spectra. Single super layer measurements are equivalent to measuring the total column CO column density. The total column measurement is chosen to avoid effects from smoothing and oscillations from unconstrained portions of multilevel retrievals, thereby providing the best metric to determine best bias spectrum.

Table 5.2 presents the results from retrievals that use no bias spectrum, a BT bias spectrum, or a NN bias spectrum on kCARTA spectra. A trial with each one of the bias spectra is used with the two different retrieval equations (LSQ and LSQwAP), where a trial consists of performing the CO retrieval for the entire 28 cloud-free days. Results in Table 5.2 are the linear regression coefficients found from the lines of linear fit along with RMSE between the retrieved total column CO measurement and the true composite CO measurement. The scatter plots for the trials that used bias spectrums are seen in Figures 5.1(a) - 5.1(d). For both LSQ,

	LSQ				LSQwAP			
Bias Spectrum	Slope	Intercept	R^2	RMSE (%)	Slope	Intercept	R^2	RMSE (%)
No Bias	0.92	-.05	0.90	12	0.87	.06	0.89	11
BT bias	1.05	-0.14	0.89	6	0.99	0.01	0.89	6
NN bias	1.09	-0.18	0.89	6	1.02	-0.05	0.89	6

Table 5.2: Linear regression coefficients for retrieval trials using no bias, BT bias, and NN bias spectrums. These trials compute linear regression coefficients from retrieved vs. *in situ* total column CO measurements, where both LSQ and LSQwAP retrieval equations are used. Root mean square error (RMSE) computed as a percent error (%) as well.

and LSQwAP retrieval equations, using no bias spectrum is found to produce the worst results. RMSE errors are the approximately the same for all combinations of bias spectrum and retrieval equation.

These results show that retrievals run using the BT bias spectrum measured the total column with less bias and more accuracy compared to retrievals using NN bias spectrum; however both agree very well with *in situ* total column measurements. Lastly, the results show that LSQwAP retrievals agree better with *in situ* measurements compared to the retrieval results using the LSQ retrieval equation. The trial using LSQwAP and the BT bias spectrum is the most successful of all the trials.

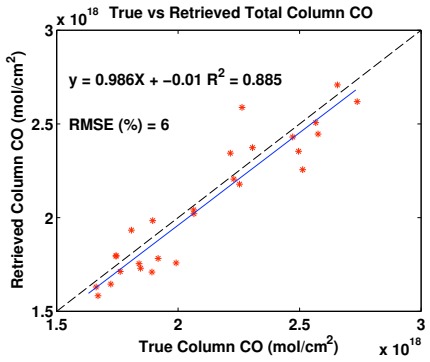

(a) BT bias and LSQwAP

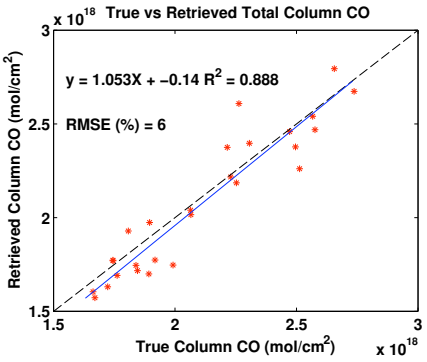

(b) BT bias and LSQ

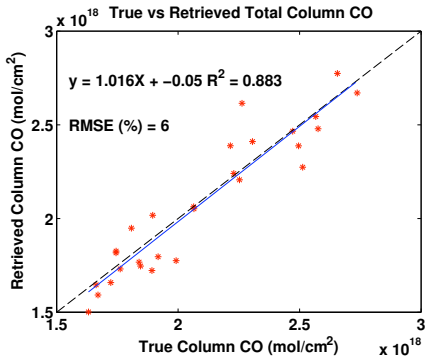

(c) NN bias and LSQwAP

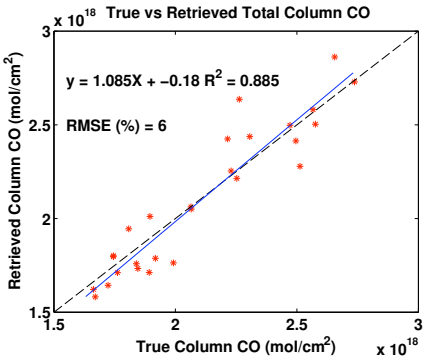

(d) NN bias and LSQ

Figure 5.1: Scatter plots and linear fit coefficients using (a) LSQwAP and BT bias spectrum (b) LSQ and BT bias spectrum (c) LSQwAP and NN bias spectrum (d) LSQ and NN bias spectrum.

5.2 SAAC vs. Version 1 CO Retrieval

Figure 5.2(c) presents the version 1 CO retrieval measured as a total column CO measurement and compared to true composite CO profiles. The version 1 CO retrieval reports one VMR in *ppbv* that represents a constant tropospheric VMR profile. The single VMR is used to create a merged profile with a constant VMR. This merged profile is input into KLAYERS to create an RTP profile and then is summed up to create the Version 1 total column measurement.

Comparing Figure 5.2(c) to Figures 5.2(a) and 5.2(b) shows that total column CO, measured by either retrieval equation, exhibits the same systematic bias as the version 1 CO. This bias exists even after the data set, consisting of the true composite CO profiles, is cloud flagged by NN. This is the same systematic bias found in version 1 CO validation study [90] and demonstrates that spectral tuning is needed for SAAC or Version 1 CO retrievals to account for the modeling deficiencies in the water vapor continuum and kCARTA.

5.3 Retrieval Grid Layer Analysis

This section examines trials using LSQ and LSQwAP retrievals for the 2, 3 and 5 layer retrieval grids.

5.3.1 LSQ Trials

This section presents the retrieval results for the LSQ retrieval equation on 2, 3 and 5 layered retrieval grids. RMS and bias calculated from the difference

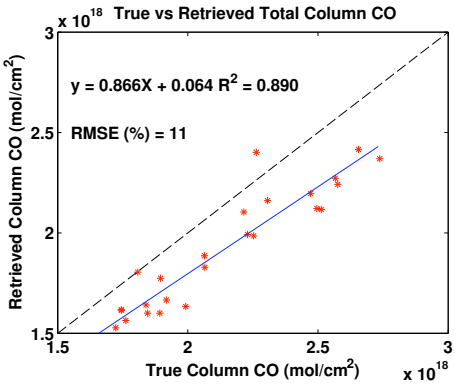

(a) No bias and LSQwAP

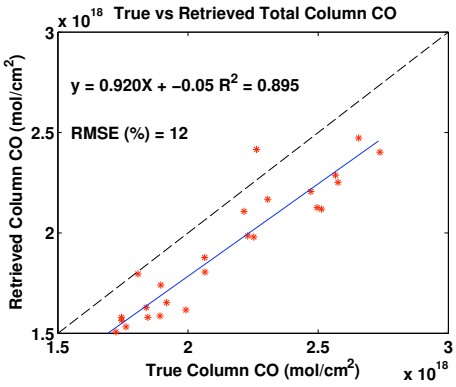

(b) No Bias and LSQ

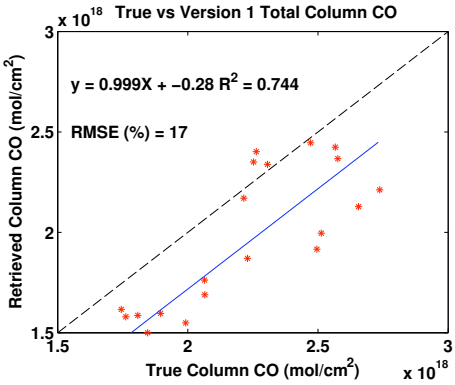

(c) Version 1 CO Retrieval

Figure 5.2: Scatter plots and linear fit coefficients using (a) LSQwAP and no bias spectrum (b) LSQ and no bias spectrum (c) Version 1 CO Retrieval.

between the retrieved CO value (z) and the true composite CO value mapped onto the same retrieval grid. Figures 5.3(a) - 5.3(f) present the error analysis. Figures 5.3(b), 5.3(d), and 5.3(f) all show a decrease in the RMS error below 800 mb of at least 10% when compared to the RMS error for the *a priori*.

The RMS error for the 2 layer case improves from 15 to 8%. The improvement is explained by the interpolation process used to update the retrieved profile, where interpolation creates correlation among layers which is similar to the correlation from the true composite CO profiles. The improved RMS in the three layer case at 600 mb is partially due to the measurement, as AERI averaging kernels indicate small amounts of information come from the region just above 800 mb. The five layer case shown in Figure 5.3(f) demonstrates that the RMS error is reduced from 23% to 10% near the surface, and has improvements of 2-3% for values above 600 mb. Again, some of the improvement is due to the interpolation process which correlates the layers.

By definition of the *a priori*, a bias should not exist for the *a priori* profile; however, the *a priori* profile is built on all 56 profiles, and not the subset of cloud-free days. This explains why a bias is present in Figures 5.3(a), 5.3(c),and 5.3(e). In all cases a bias of approximately 5% exists in the *a priori* value for the first layer in each retrieval grid. Figures 5.3(a) show that the LSQ retrieval reduces the bias to zero in the first retrieval layer; however, the bias in the second retrieval layer increases to 5%. The 3 and 5 layer retrievals change the bias from an approximately 6% to -3%. This oscillation coincides with an induced positive bias for both 3 and 5 layer retrievals. This oscillatory pattern is a result of the lack of vertical information

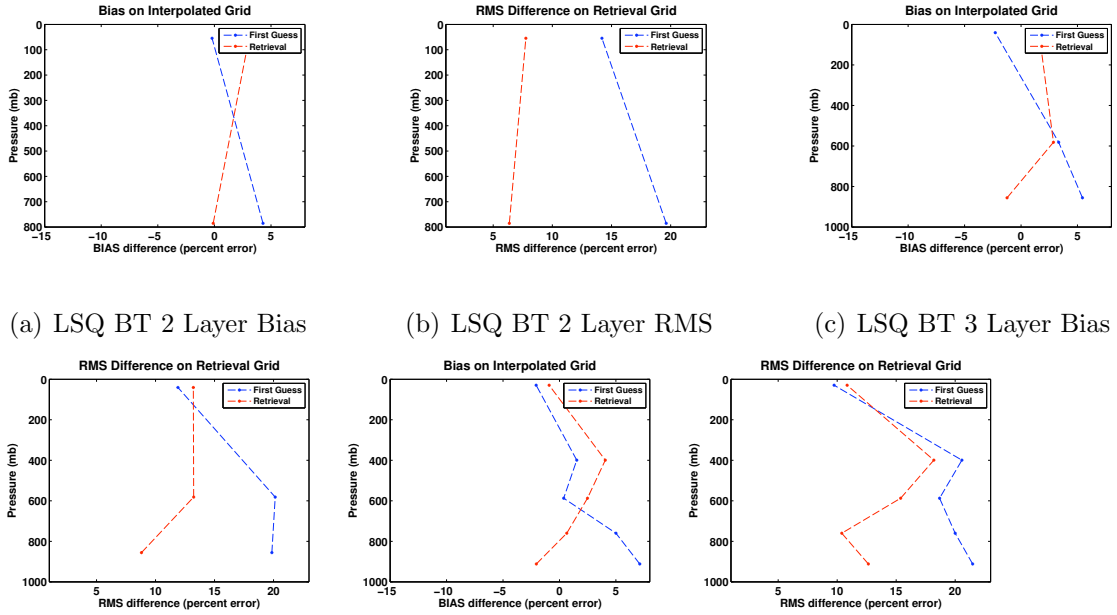

(a) LSQ BT 2 Layer Bias (b) LSQ BT 2 Layer RMS (c) LSQ BT 3 Layer Bias

(d) LSQ BT 3 Layer RMS (e) LSQ BT 5 Layer Bias (f) LSQ BT 5 Layer Bias

Figure 5.3: RMS and bias calculations for the 28 days determined to be cloud-free for LSQ on the 2, 3 and 5 layer retrieval grid. True composite CO profiles are mapped to the retrieval grid representation through relation $z = Wx$ described in Section 4.1. All results presented here use the LSQ retrieval equation, *a priori* first guess, and the BT bias spectrum. The retrieval grids used in each figure are (a) and (b) 2 layer, (c) and (d) 3 layer, and (e) and (f) 5 layer.

from AERI spectra.

Table 5.3 presents the results from applying lines of linear fit to scatter plots of retrieved total column CO vs. true composite CO profiles converted to total column. The total column measurement is calculated as the sum of the RTP CO profile ($\hat{x}$) for 2,3 and 5 layered retrievals. Moving left to right across Table 5.3 shows the the linear regression coefficients and RMSE for retrievals with NN or BT bias spectrums. Comparing left to right reveals no difference for RMSE and little difference for linear regression coefficients; thus, indicating that there is little difference in effect from using either BT or NN bias spectrums. Moving from the top of Table 5.3 to the bottom reveals that as more layers are added to retrieval grid the total column measurement increases in RMSE error; however, the 5% RMSE for the 2 layer retrieval grid may not be totally representative for larger CO data sets with less vertical correlation.

5.3.2 LSQwAP Trials

This section presents the retrieval results for the LSQwAP retreival equation on 2,3 and 5 layered retrieval grids. RMS and bias calculated from the difference between the retrieved CO value (z) and the true composite CO value mapped onto the same retrieval grid. Figures 5.4(a) - 5.4(f) present results for the error analysis, where the BT bias spectrum is used to tune kCARTA spectra. Trials using the NN bias spectrum are nearly identical to trials using the BT bias spectrum, and therefore not shown here.

	LSQ							
	BT				NN			
Ret. Grid	Slope	Intercept	R^2	RMSE (%)	Slope	Intercept	R^2	RMSE (%)
2 Layer	0.86	.25	0.89	5	0.88	0.23	0.88	5
3 Layer	0.55	0.90	0.85	8	0.53	0.95	0.85	8
5 Layer	0.47	1.06	0.85	10	0.40	1.21	0.83	10

Table 5.3: Linear regression coefficients for retrieval trials using 2, 3 and 5 layer retrieval grids. These trials compute linear regression coefficients from retrieved vs. *in situ* total column CO measurements, where both BT or NN bias spectrums are used. Root mean square error (RMSE) computed as a percent error (%) as well. All results in this table are for the LSQ retrieval.

Examining bias results in Figures 5.4(a), 5.4(c), and 5.4(e) reveal different results for LSQwAP trials compared with LSQ trials. Just as it is in the LSQ trial, the bias in the first layer for the 2 layer retrieval grid layer is reduced to zero; however, unlike the LSQ case, layer 1 biases are reduced to zero for both the 3 layer and 5 layer retrieval trials. Also unseen in the bias results for trials using 3 and 5 layers is the induced positive bias for the upper parts of the profiles resulting in the retrieval process. This observation is a result of the LSQwAP retrieval equation's constraint to the first guess CO profile, where the size of the constraint is determined by the diagonal of the constraint matrix H. The fact that Figures 5.4(a), 5.4(c), and 5.4(e) all present near zero bias for all retrieval layers suggests that the magnitude of the diagonal terms in constraint matrix appropriately models the variation in this CO data set. The two exceptions are the 2% biases shown for layer 3 in Figures 5.4(c) and 5.4(e).

Comparing the RMS results for the LSQwAP trials (Figures 5.4(b), 5.4(d), 5.4(f)) to the RMS results for the LSQ trials (Figures 5.3(b), 5.3(d), 5.3(f)) two general results trends are seen:

1. Compared to the LSQwAP retrieval trials, RMS error is lower in the LSQ retrieval trials for retrieval layers greater than 1 in all retrieval grids.

2. RMS error is 1-2% less for the LSQwAP trials compared to the LSQ trials in the first layer; specifically, for the 3 and 5 layer case.

This shows that the LSQwAP is only constrained to the first guess in portions of the atmosphere where the retrieval has little sensitivity; however this constraint allows

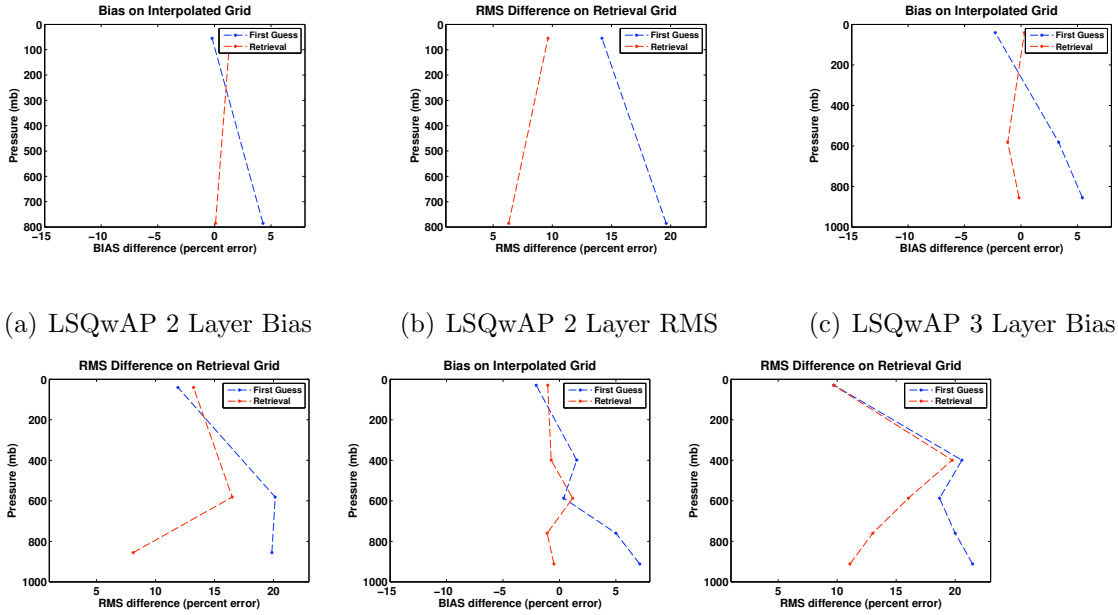

(a) LSQwAP 2 Layer Bias (b) LSQwAP 2 Layer RMS (c) LSQwAP 3 Layer Bias

(d) LSQwAP 3 Layer RMS (e) LSQwAP 5 Layer Bias (f) LSQwAP 5 Layer RMS

Figure 5.4: RMS and bias calculations for the 28 days determined to be cloud-free for LSQ on the 2,3 and 5 layer retrieval grid. True composite CO profiles are mapped to the retrieval grid representation through relation $z = Wx$ described in Section 4.1. All results presented here use the LSQwAP retrieval equation, *a priori* first guess and the BT bias spectrum. The retrieval grid used in each figure is (a) and (b) 2 Layer, (c) and (d) 3 Layer, and (e) and (f) 5 layer.

the LSQwAP to measure CO near the surface.

	LSQwAP							
	BT				NN			
Ret. Grid	Slope	Intercept	R^2	RMSE (%)	Slope	Intercept	R^2	RMSE (%)
2 Layer	0.72	0.56	0.88	6	0.73	0.55	0.88	6
3 Layer	0.46	1.10	0.83	9	0.45	1.13	0.84	9
5 Layer	0.43	1.15	0.83	9	0.40	1.25	0.80	10

Table 5.4: Linear regression coefficients for retrieval trials using 2, 3 and 5 layer retrieval grids. These trials compute linear regression coefficients from retrieved vs. *in situ* total column CO measurements, where both BT or NN bias spectrums are used. Root mean square error (RMSE) computed as a percent error (%) as well. This is for the LSQwAP retrieval equation

Table 5.4 presents the results from applying lines of linear fit to scatter plots of retrieved total column CO vs. true composite CO profiles converted to total column for LSQwAP trials. The total column measurement is calculated the same way it was for the Table 5.3. Moving left to right across Table 5.4 reveals that there is little difference in using the BT or NN bias spectrums. Moving from the top of Table 5.4 to the bottom shows that adding layers reduces the effectiveness of the total column measurement from AERI. This observation is made because retrievals performed with more layers corresponds to worse coefficients of linear fit between the true total column of CO and a total column of CO calculated from AERI retrievals.

This is the same trend as is seen in the LSQ trials; however, it is more pronounced here. This is because the LSQwAP retrieval equation sticks to the first guess, and as more layers are added, the retrieved profile becomes more like the *a priori* profile.

5.4 Single Day Profile

To demonstrate the retrieval a single case from 20070126 is presented. Merged profile representations are created from retrieved RTP CO profiles and are presented as a VMR. The resulting VMR is then listed on a pressure level corresponding to the effective pressure of the layer.

Figure 5.5(a) shows that the version 1 CO retrieval (cyan) measures a VMR of 120 *ppbv*. This displays the vertical uncertainty of the version 1 retrieval, as 120 *ppbv* represents a weighted average of the true Composite CO profile (green). Figures 5.5(a) and 5.5(c) show the LSQ and LSQwAP retrievals, converted from the RTP profiles to the merged profiles. Merged profiles are created by taking the column density CO amount for each layer in the RTP profile and dividing by the total amount of air molecules in the layer. Both LSQ and LSQwAP overestimate the surface value by approximately 30 *ppbv* while relaxing back to the first guess profile above 800 mb. Figures 5.5(b) and 5.5(d) are the corresponding normalized averaging kernels for the LSQ and LSQwAP retrievals respectively. These averaging kernels display that any perturbations to the true atmospheric profile cause the retrieved profile to have its largest change in the first layer.

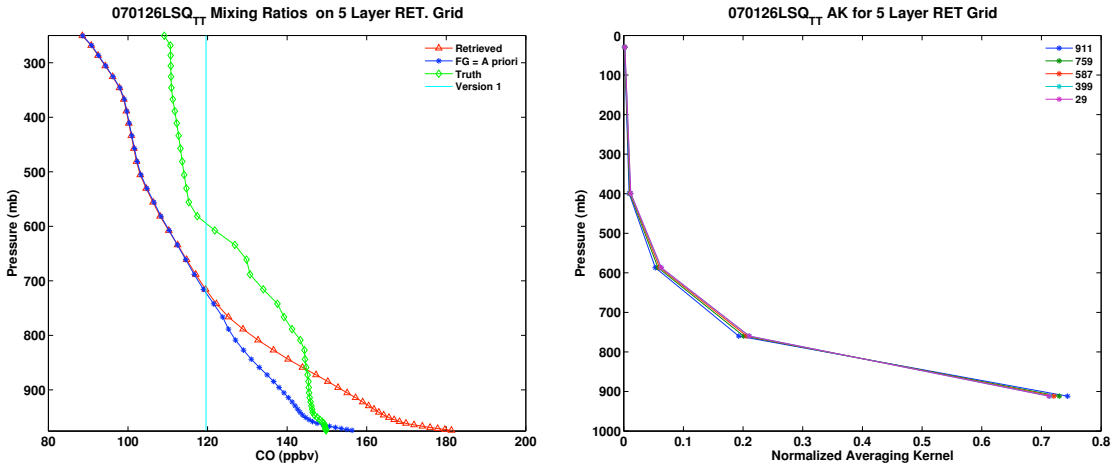

(a) LSQ Merged Profile Grid

(b) LSQ

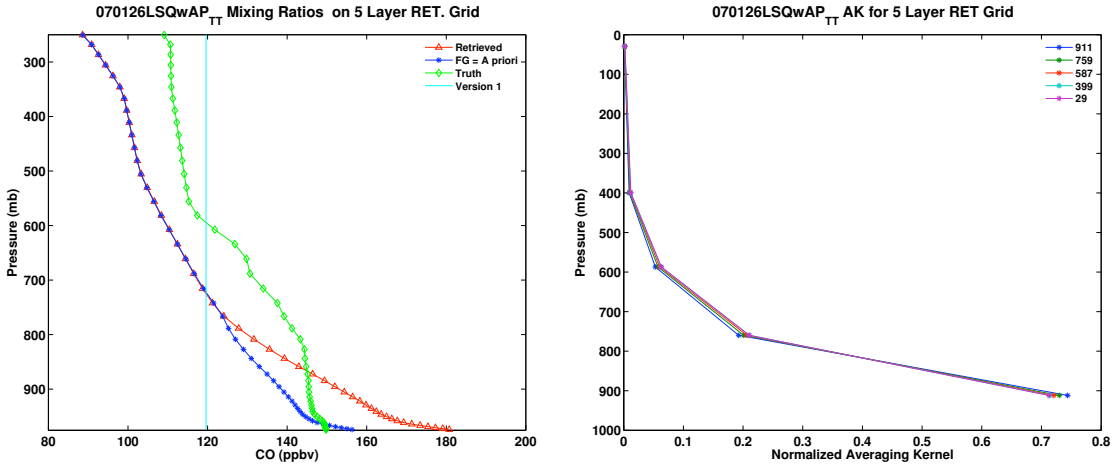

(c) LSQwAP Merged Profile Grid

(d) LSQwAP

Figure 5.5: (a) CO retrieval on the merged profile grid (*ppbv*) using a 5 layer LSQ retrieval equation and the NN bias spectrum for 20070126 (b) Averaging kernel for the 5 layer retrieval grid using LSQ and the NN bias spectrum for 20070126. (c) CO retrieval on the merged profile grid (*ppbv*) using a 5 layer LSQwAP retrieval equation and the NN bias spectrum for 20070126. (d) Averaging kernel for the 5 layer retrieval grid using LSQwAP and the NN bias spectrum for 20070126.

The retrieval equation can be broken down into three components:

$$\hat{z} = Az_{true} + (I_n - A)z_a + G\epsilon \tag{5.1}$$

where, Az represents how the true profile is smoothed by the averaging kernel, $(I_n - A)z_a$ represents the the contribution from the first guess, and $G\epsilon$ represents how measurement error is propagated to the retrieved solution ($\hat{z}$).

Using this breakdown it's possible to understand the contributions to the over-estimated retrieved solutions seen in Figures 5.5(a) and 5.5(c).

Figure 5.6 presents the retrieval profile (red), true composite CO profile (green), and first guess profile (blue). Also shown in black is the convolved truth profile which is calculated as ($\grave{z} = Az + (I_n - A)z$). The convolved truth represents the true profile after it is smoothed by the retrievals vertical sensitivity. Examining Equation 5.1 reveals that the convolved truth represents the retrieval minus contributions from error. Using this relation it is seen that the convolved true profile in Figure 5.6 overestimates the true profile, indicating that the LSQwAP retrieval compensates for the difference in layers 2-5 between the truth and first guess profiles by perturbing the first layer (bottom layer). The difference in the bottom layer between the retrieved value and the convolved true profile is a result from the measurement errors contribution to the retrieved value.

5.5 SAAC Conclusions

Using a 1 super layer retrieval grid it is demonstrated that SAAC retrievals can measure total column CO to better than 6%. This is a significant improvement over

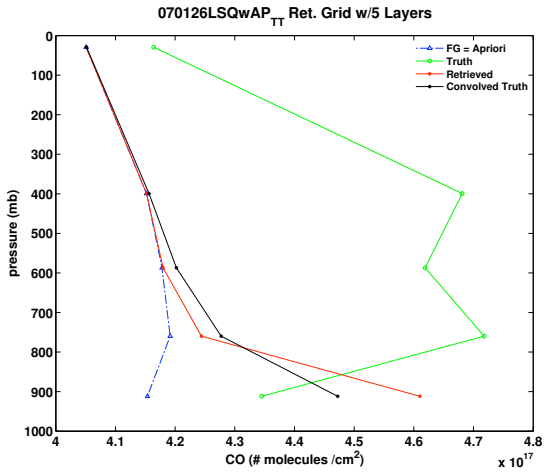

Figure 5.6: CO retrieval on the 5 layer retrieval grid using the LSQwAP retrieval equation and the NN bias spectrum for 20070126. The first guess profile is the *a priori* profile.

the 15% variation from the *a priori*. Both LSQ and LSQwAP retrieval equations measure the single layer CO (total column) to within 6% of the true total columns. The range of slopes from true total column vs retrieved total columns scatterplots are 0.99-1.09 for any combination of bias spectrum (NN,BT) or retrieval equation (LSQ, LSQwAP). The best total column measurement is found when using the LSQwAP retrieval equation with the BT bias spectrum.

Direct comparisons of the 28 cloud-free true composite CO profiles showed that the systematic bias that existed in [90] still persists for the version 1 retrieval. SAAC retrievals using LSQ and LSQwAP had the same systematic low bias when no bias spectrum is used. This indicates the reason for the systematic low bias in the previous AERI CO study is a result of the bias present in modeling the CO band from kCARTA. Version 1 total column results indicated a 17% RMSE. LSQ and LSQwAP single layer retrievals both showed no systematic bias and a much

greater accuracy and therefore are superior to the version 1 CO retrieval.

When retrieving profiles the biggest improvement came in the first layer of each retrieval grid. The improvement in RMS error ranged from 10 - 13%, with the biggest improvement coming for the 2 layer retrieval grid. RMS error improved by 2-3% over the *a priori* for retrieval grid layers above the first layer. Some of this improvement comes from the linear interpolation method used to update the RTP CO profile. This causes correlation between the layers. Using the five layer grid scheme is the best choice to effectively decouple the atmosphere into portions that AERI is sensitive to ($\geq$ 700 mb), from portions it's not sensitive to.

Bias results suggest LSQwAP better constrains the top profiles. This suggests that the constraint matrix is providing proper amounts of constraint for this data set. An independent data set is needed to better characterize whether the constraint matrix works and no bias will exist again. Also, LSQwAP does a better job removing bias compared to the LSQ, which says that by constraining the top to the *a priori* rather than letting it oscillate, allows for a better solution to the bottom.

Trials using retrieval grids of 2, 3 and 5 layers to calculate total column measurements showed degrading results in comparison to total column calculated from true composite CO profiles. These results saw decreases in slopes from approximately .8 for 2 layers to approximately .4 for 5 layers. This further demonstrates the lack of vertical information in AERI spectra with respect to CO.

The new retrieval system creates averaging kernels that characterize the vertical sensitivity SAAC has with respect to the true atmospheric profile. Through the use of these averaging kernels, it is shown that both LSQ and LSQwAP retrievals

compensate for differences between the first guess free tropospheric values and the true CO free tropospheric values by perturbing the layer closest to the surface. This illustrates the need to include more information in the retrieval, either by introducing correlation coefficients in the off-diagonals of H_{TT} or through a dynamic first guess.

Lastly, the LSQ and LSQwAP retrieval equations provided nearly identical RMS error and bias results, for all cases and trials shown in this chapter.

Chapter 6

SAAC plus AIRS

This chapter presents results from using AIRSv5 retrieved CO [47] as the first guess to the SAAC retrieval. As demonstrated in Chapter 5 AERI spectra has limited sensitivity above 3km (less than 700 mb); therefore, AIRS is used as a first guess to better constrain portions of the atmopshere where SAAC has limited sensitivity. The two different retrieval equations are presented again below:

$$\begin{aligned} \textbf{Nearly Linear (LSQ)} x_{i+1} &= (1+\alpha)x_i \\ \textbf{Moderately Nonlinear (LSQwAP)} x_{i+1} &= x_a + \alpha x_i = (\alpha + \frac{x_a}{x_i})x_i = \beta x_i \end{aligned}$$

These are the same equations developed in Chapter 4 and used in Chapter 5 however, AIRS first guess profiles are now used for x_a and x_i for LSQwAP and LSQ retrieval equations respectively. A new constraint matrix is made for use with the AIRSv5 first guess. A nominal variation of 30% is used which corresponds to a diagonal constraint matrix with values of 0.09 on the diagonal.

The version of AIRS retrieved CO profiles used to create the true composite CO is on a 9 level grid. This is different than the version used to create the first guess which is gridded onto 100 levels. For this work, it is assumed that the AIRS CO retrievals used to create the upper portions of the true composite CO profiles accurately represent truth. In reality they are not, and even contain a 10% bias

[47]; however, for assessing the quality of the retrieval it is important to use days where the first guess provides an accurate representation of the upper atmosphere. Therefore, only cases where the two different AIRS versions are in agreement are used.

The 28-day cloud-flagged profiles from chapter 5 are examined to assure the similarity between the two AIRS data sets. Good cases are chosen by examining the similarity between the two different types of AIRS profiles above 600 mb. This results in 13 possible days to use AIRSv5 CO retrievals as the first guess CO profile for LSQ and LSQwAP retrieval equations. The specific days to use are listed in Table 6.1.

20070218	20070307	20070404	20070826	20070828	20071001	20071106
20071108	20080227	20080721	20080721	20081016	20081030	

Table 6.1: Cloud-free dates where AIRS first guess profiles from [89] match up well with the upper portion of the true composite CO profiles. Cloud clearing is done using the neural network discussed in Section 3.1.

6.1 An Example Profile

This section presents a single retrieval case using AIRSv5 CO as the first guess. The single case chosen is taken from 20070218. Both LSQwAP and LSQ retrieval equations are examined below.

6.1.1 LSQwAP

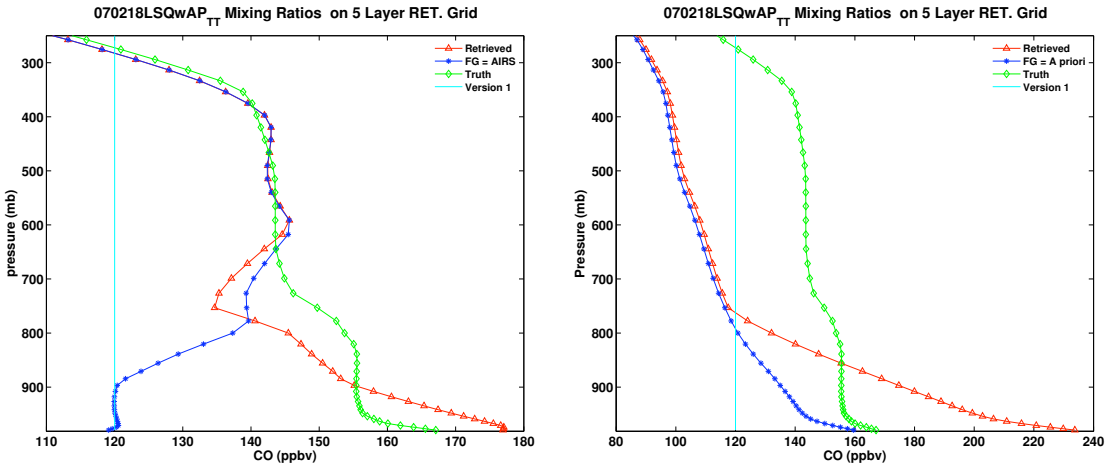

(a) AIRS First Guess LSQwAP (SAAC+AIRS) (b) *a priori* First Guess LSQwAP (SAAC)

Figure 6.1: (a) Retrieval using the LSQwAP retrieval equation with the NN bias spectrum, and AIRSv5 first guess. (b) Retrieval using the LSQwAP retrieval equation with the NN bias spectrum, and the *a priori* profile used as the first guess. Both retrieval results take the RTP CO profiles and convert them to merged profiles.

Figures 6.1(a) and 6.1(b) show merged profile retrieval results for the LSQwAP retrieval equation using either a AIRSv5 CO profile or the *a priori* as the first guess profile. Figure 6.1(a) shows that the version 1 CO retrieval significantly underestimates any portion of the true profile and clearly is affected by errors in synthetic spectra.

One result from Chapter 5 states that when CO is underestimated by the first guess above 700 mb, the resulting effect is to perturb the bottom portion of the retrieved profile. The inclusion of the AIRS retrieval as a first guess is

shown in Figure 6.1(a) to provide a better first guess compared with the *a priori* first guess, and removes the large perturbation in retrieved CO below 800 mb seen in Figure 6.1(b). The first guess profile in Figure 6.1(a) displays that AIRSv5 underestimates the first layer of the true profile by 30%, however the retrieval in SAAC+AIRS is able to measure that 30%. Therefore, through comparisons for retrieved merged profiles in Figures 6.1(a) and 6.1(b), it is determined that in this case SAAC+AIRS is superior to either SAAC or AIRS.

6.1.2 LSQ and Type of Problem

The functional difference between the retrieval equation LSQ, and LSQwAP is that at each iteration LSQwAP is constrained to the first guess, whereas LSQ is constrained to the previous iteration. Figures 6.2(a) and 6.2(b) present the retrieval of CO for the LSQwAP on the merged grid when using AIRS or the *a priori* as a first guess profile. Comparing the LSQ retrieval solution from Figures 6.2(a) and 6.2(b) to the results for the LSQwAP solution in Figures 6.1(a) and 6.1(b), no noticeable difference is found for either choices of first guess profiles (AIRSv5, *a priori*).

Examining the retrieval equations for LSQ and LSQwAP gives insight to why there is no significant difference. The same first guess profile (x_a) is used at the first iteration for both retrieval equations. Through substitution of $x_a = x_i$ into Equations 4.21 and 4.14 respectively, a comparison between the retrieval equations at the first iteration can be made.

First, the substitution is made into Equation 4.21 that represents the solution

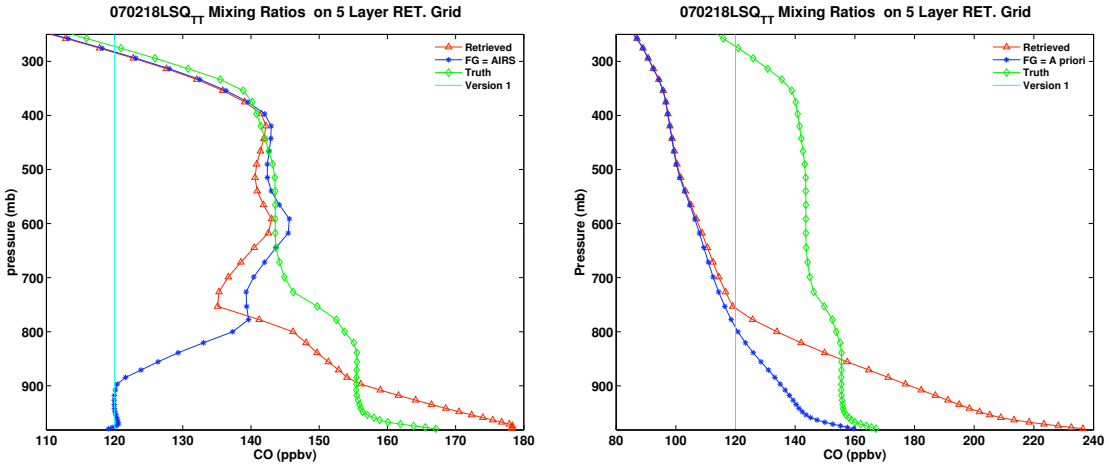

(a) AIRS First Guess LSQ (SAAC+AIRS)

(b) *a priori* First Guess LSQ (SAAC)

Figure 6.2: (a) Retrieval using the LSQ retrieval equation with the NN bias spectrum, and AIRSv5 first guess.(b) Retrieval using the LSQ retrieval equation with the NN bias spectrum, and the *a priori* profile used as the first guess. Both retrieval results take the RTP CO profiles and convert them to merged profiles.

to the moderately non-linear problem:

$$\begin{aligned} x_{i+1} &= x_a + (K_i^T S_e^{-1} K_i + H^{-1} K_i^T S_e^{-1}[y - F(x_a) + K_i(x_a - x_a)] \\ x_{i+1} &= x_a + (K_i^T S_e^{-1} K_i + H^{-1} K_i^T S_e^{-1}[y - F(x_a)] \end{aligned}$$

Next, the substitution of $x_a = x_i$ for the nearly linear case represented by Equation 4.14 is done but not presented here. By inspection of Equation 4.14 it's easy to confirm that this substitution yields the identical solution as the moderately non-linear problem shown above. Therefore, at the first iteration both LSQ and LSQwAP retrieval solutions are identical. As the retrieval continues on to the next iteration the LSQ and LSQwAP retrievals have their normal forms given by Equations 4.14 and 4.21 respectively. If the variation in the true state of CO is large enough that it required multiple iterations to reach the solution, then the results from LSQ and LSQwAP would be different; however, all results display that the solutions are within 1% of each other. This is true even for results using AIRSv5 CO as the first guess, where the AIRSv5 CO percent error for the atmospheric region greater than 800 mb can be as high as 30% for this data set. Therefore, over the range of true composite CO profiles shown in this data set (variation $\approx$ 20% from the *a priori* profile) the forward problem is nearly linear; however, this data set does not contain the same variation as locations that have significant amounts of pollution outflow. These regions are shown to vary 50-100% [17, 52]. In these locations the LSQwAP retrieval is expected to work better because it does not make assumptions about linearity.

6.2 Error Statistics

The RMS error for the 5 layer retrieval grid is presented in Figures 6.3(a), 6.3(b), 6.3(c), and 6.3(d). The trial here consists of calculating the RMS difference between true composite CO and retrieved CO profiles on the retrieval grid for different first guesses, bias tuning spectrums, and channels included in the retrieval.

Next, the retrieval is adjusted to use all 172 channels between 2107 - 2189 cm^{-1}. It was found that every channel carried some information as defined by the Shannon information content (H_s), and the degrees of freedom is approximately 1.1 when all channels are used. The error covariance for this whole band retrieval trial uses the full error covariance matrix shown in Chapter 4 on page 116 (Figures 4.5(a)- 4.5(d)). As shown in Figure 6.3(d), the retrieved first layer RMS error is 12%, which is more than the 9% from the trial using the selected channels and the BT bias spectrum (Figure 6.3(c)). Moreover, the error in retrieval layer 2 doubles for the trial using the whole band and the rest of the retrieval layers increase in error as well. These results validate the use of the channel selection method in this retrieval.

Comparing either figure using the AIRS first guess (Figures 6.3(a), 6.3(a)) to the trial using *a priori* (Figure 6.3(b)) reveals the improvement by using the AIRSv5 CO first guess. The layer 1 retrieval RMS error improves from approximately 11% to 8-9% by using AIRSv5 CO as the first guess. Therefore, it is possible to estimate the effect of using a free tropospheric guess which is in error by 10 - 15%. This effect contributes 1 -2% in the layer 1 results. Thus, the 10% systematic high bias in AIRS [47] should result in a 1% bias in layer 1 retrieval grid.

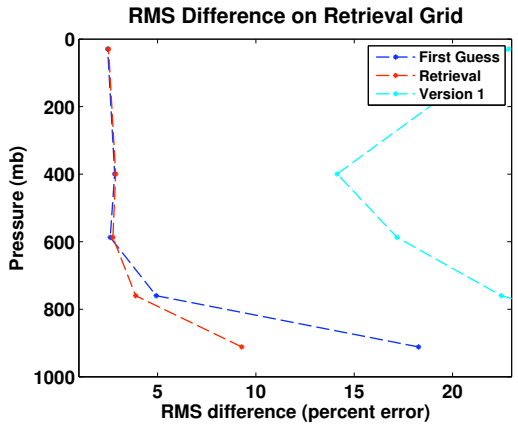

(a) AIRS First Guess NN bias spectrum

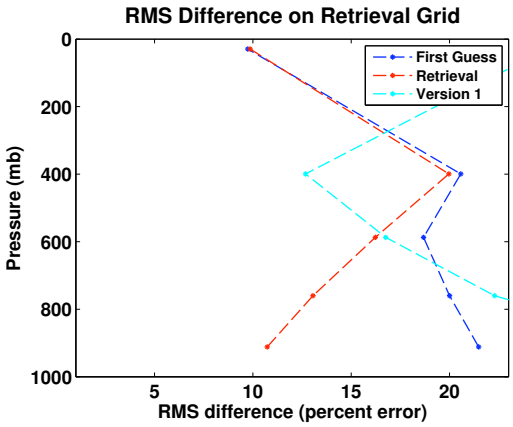

(b) *a priori* NN bias spectrum

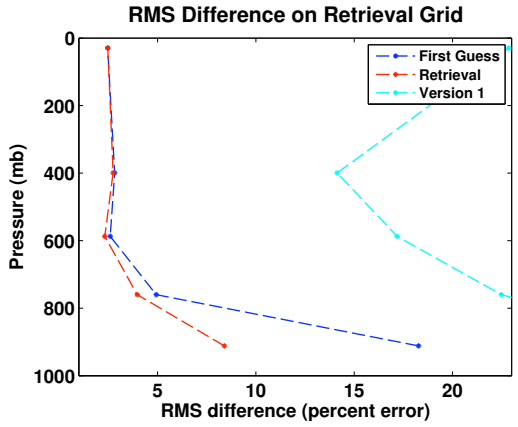

(c) AIRS First Guess BT bias spectrum

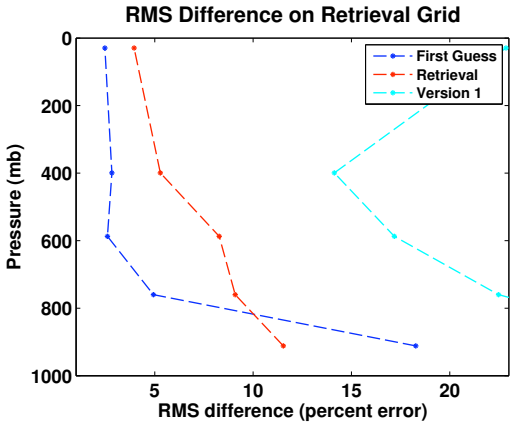

(d) AIRS First guess Whole Band NN Bias Spectrum

Figure 6.3: RMS error calculations for LSQwAP retrieval equation on the retrieval grid. (a) AIRS first guess and NN bias spectrum (b) *a priori* and NN bias spectrum(c) AIRS first guess and BT bias spectrum (d) AIRS first guess, NN bias spectrum, and using all channels from 2107-2189 cm^{-1}.

The largest improvement resulting from using the AIRSv5 CO is in layer 2, which reports an RMS error of approximately 4%. This is less than half the RMS error from layer 2 which is 13 - 14%. This region represents the overlap where retreivals from AIRS and AERI both contain small amounts of information. Layers 3 - 5 show an improvement because SAAC has no sensitivity there and is entirely made up of whatever first guess profile is used.

Finally, some context must be given about the 4% RMS error seen in Figures 6.3(a) and 6.3(c). Because different versions of AIRS CO retrievals are used for the first guess, and the SAAC retrieval does not change layers 3-5, then this represents the agreement between the two versions of AIRS CO retrievals. Layers 3-5 in the SAAC retrieval will contain the same error as the AIRS CO profile, or whatever first guess profile is chosen.

Figures 6.4(a) and 6.4(b) both show the total column calculations from the 5 layer retrievals using an AIRSv5 first guess and the *a priori* first guess respectively. All three linear fit parameters improve by using the AIRSv5 first guess. Furthermore, the linear fit parameters and RMS error are comparable to SAAC using *a priori* on 1 super layer to retrieve total column.

6.3 Future Uses and Work

The satellites AIRS [47], IASI [83, 42], TES [6, 38], and MOPITT [14] are all instruments that retrieve CO profiles and can be used as a first guess to SAAC. These satellites have been measuring global CO data since 2000. Table 6.2 gives the data

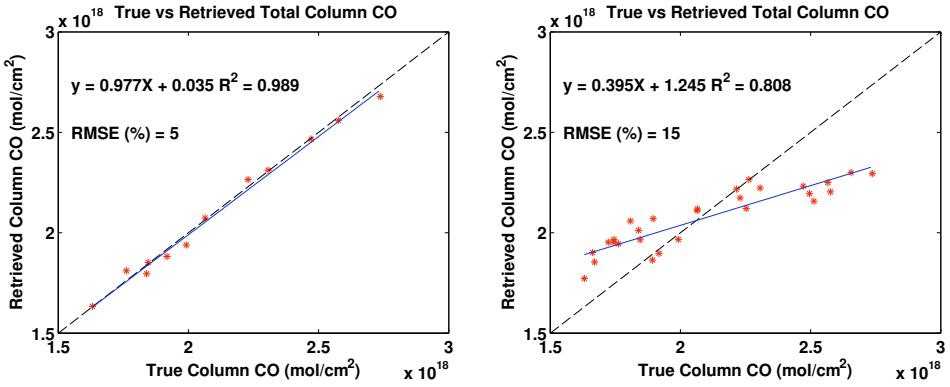

(a) AIRS First Guess

(b) *a priori*

Figure 6.4: (a) Total column CO scatter plot and linear regression coefficients for retrieval vs *in situ* using LSQwAP, AIRS first guess, and bias spectrum for days listed in Table 6.1. (b) Total column CO scatter plot and linear regression coefficients for retrieval vs true composite CO using LSQwAP, *a priori*, and bias spectrum for days listed in Table 5.1.

taking periods for the different satellites. With each one of these satellites providing nearly daily global CO profiles, there is ample opportunity to get multiple profiles per day, create diurnal trends going back to 2000, and do inter-comparisons with different satellite first guess profiles. Moreover, different satellites can be combined with tower and aircraft measuring *in situ* CO. This would create the independent CO profile data set needed to truly validate the SAAC retrieval scheme. Also, more information can be added to the SAAC retrieval by using optimal estimation retrievals [67]. In order to create an optimal estimation retrieval method, many more CO profiles should be used to develop true layer-to-layer correlation for the SAAC retrieval grids. The layer-to-layer correlation is then described by the off-diagonal terms in the constraint matrix used in the retrieval.

MOPITT	IASI	TES	AIRS
2000 - present	2007 - present	2004 - present	2002 - present

Table 6.2: Data taking periods for satellites measuring CO profiles [9].

The SGP site in Oklahoma contains all the necessary instruments to analyze the error in the CO band. In fact, other parts of the band have been analyzed [82] using AERI data to better constrain the LBLRTM. Results here showed that part of the error in the AERI retrievals are due to undetermined amounts of error in the CO band, and could be improved with such a study.

6.4 Conclusion

An in depth error analysis on each point of the retrieval system finds that the dominate sources of error for CO come from cloud contamination and the modeling of water from kCARTA. This is in contrast of previous studies which assumed the dominant source of error in modeled spectra was from errors in water vapor profiles input to kCARTA [28, 90], or from scattered solar photons [90]. This conclusion was drawn from observing that even by constraining the input water vapor profile with MWR, the error between model and measurement still exists and has a seasonal variation correlated to MWR measurements. The cloud effect is observed from the side by side observations of a brightness temperature contrast method [28, 34] and a neural network used to filter out clouds. [80]. Using the neural network as a cloud flag reduced the uncertainty between modeled spectra and AERI measured spectra by 30%. This improvement does not vary when comparing kCARTA models 114 and 115, or continuum models MTCKD1 and CKD24.

A new channel selection method is created which accounts for the channel-to-channel correlated error. Using this channel selection, it is found that one degree of freedom is contained in the retrieval system using AERI measurements. One degree of freedom is similar to that of the AIRS satellite [47]; however, the degree of freedom for AERI measurements is heavily weighted to the portions of the atmosphere greater than 700 mb, whereas AIRS is weighted to 500 mb.

A retrieval system using AERI measurements is created that uses two types of first guess profiles and follows a constrained least square retrieval methodology

in [67]. In both cases, the retrieval results are shown to be highly sensitive to the first guess profile due to the limited information content from carbon monoxide. An *a priori* profile has been constructed from the mean of 56 composite CO profiles. For the 2, 3 and 5 layer cases the variance in the *a priori* was between 20% at the surface and between 12 and 20% for the layers above 800 mb. Using the *a priori* as the first guess and a diagonal constraint matrix in the retrieval the improved the RMS error was between 7 and 12% for the first retrieval layer ($\approx$ 910 mb). As more layers are added to the system the RMS error relaxes back to the *a priori* RMS error.

A total column CO measurement from AERI is developed by using one super layer to represent the entire atmosphere. This total column measurement demonstrates the importance of centering modeled spectra by adding in a bias spectrum. It has been demonstrated that using the BT or NN bias spectrum reduces percent error in total column measurements from 12 to 6%. No significant difference in RMSE is found between using NN or BT bias spectrums; however, the coefficients of linear fit are slightly better for the BT bias spectrum. This may suggest a larger bias is present in modeled spectra from kCARTA that is not completely accounted for by the NN bias spectrum. The Using the *a priori* as a first guess, a BT bias spectrum, and LSQwAP retrieval methodology, it has been found that the linear fit statistics between true and measured total column CO has a slope of 0.99 with an intercept of 0.01 and an R^2 value of 0.89. Using this set of parameters showed the best overall results for the total column CO retrieval.

A dynamic first guess profile from AIRSv5 CO retrievals [47] improves the

upper and lower atmospheric retrieval RMS error. A direct comparison between the five layer retrieval using the two different first guess profiles indicate that below 800 mb the RMS error is improved by 3% when using the AIRSv5 CO as a first guess profile rather than the *a priori*. The upper atmosphere RMS error is improved between 5 and 15% when using the AIRSv5 CO profile. A constrained least square with *a priori* method proved unsuccessful due to the constraint matrix chosen; however this analysis was able to classify the retrieval problem as nearly linear for the variance shown in the data set; however, more data is needed to make a general statement about linearity of this problem.

This retrieval system improves upon previous CO retrievals from AERI [28, 90] through error analysis and algorithm implementation. With each retrieval, averaging kernels, gain matrices, and degrees of freedom are output which provide the information about sensitivity to CO distribution and error propagation in the system. Furthermore, by following the methods presented in the dissertation, the retrieval is easily updated when new error estimations are determined from research into forward modeling or AERI.

The original goal of this work was to create a product capable of monitoring boundary layer venting. In order to do boundary layer venting the vertical resolution needed is less than 1 km [16]. The vertical resolution of the first layer in AERI is more than 1 km. Therefore monitoring boundary layer venting is not possible.

Appendix A

AIRSv5 vs *A priori* First Guess

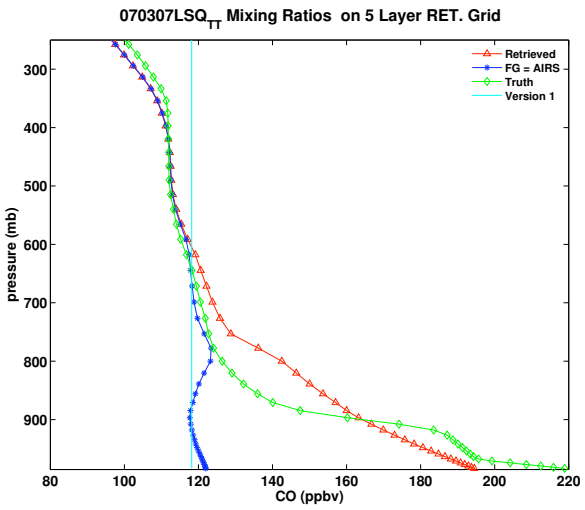

(a) AIRS First Guess

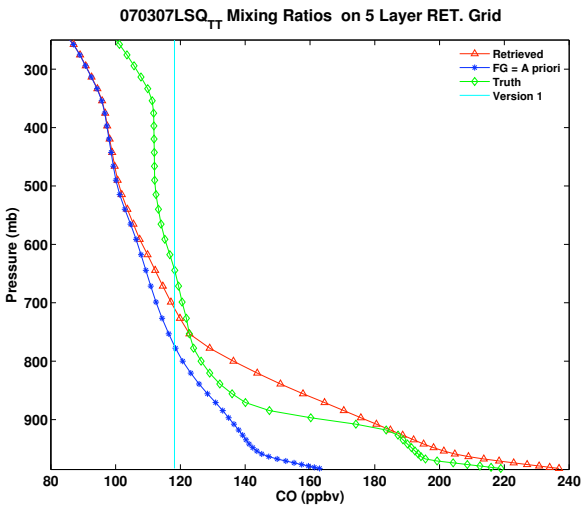

(b) *a priori*

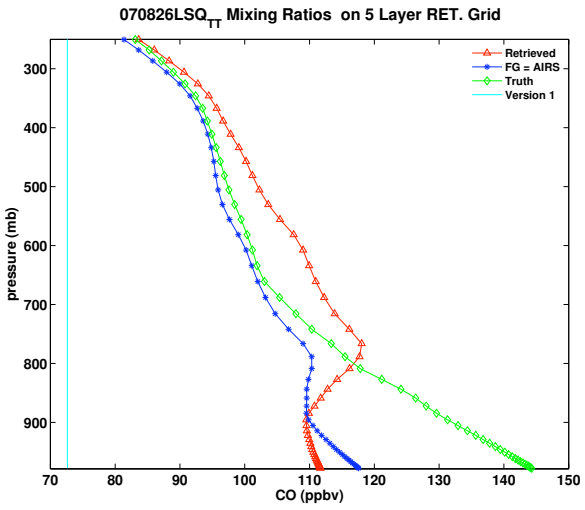

(c) AIRS First Guess

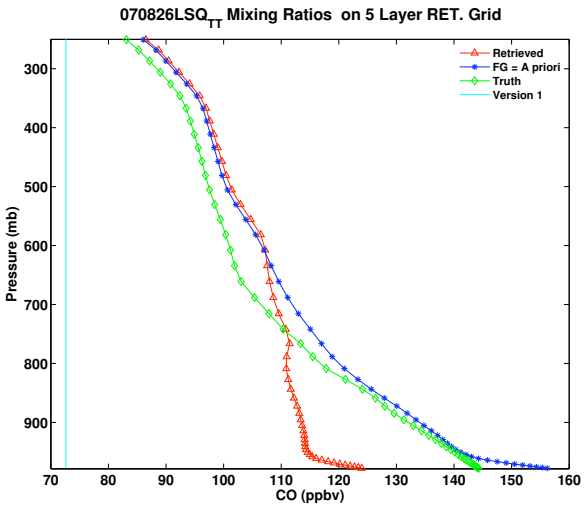

(d) *a priori*

Figure A.1: 5 layer retrieval using the NN bias spectruum and the LSQwAP retrieval equation on the merged profile grid measured in *ppbv*. (a) and (c) represent the retrieval days using AIRSv5 CO as the first guess profile. (b) and (d) represent the retrieval results using an *a priori* first guess.

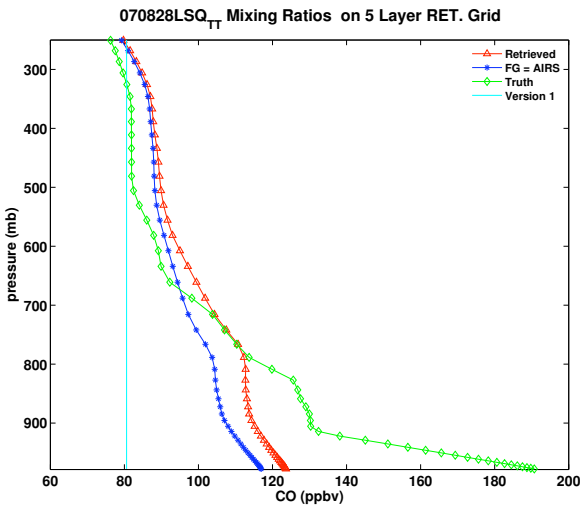

(a) AIRS First Guess

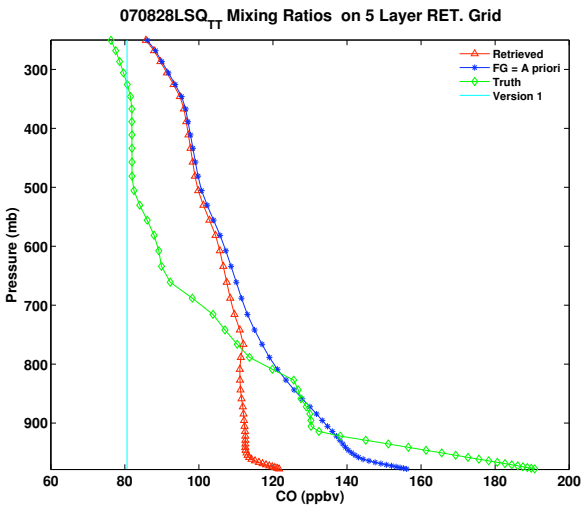

(b) *a priori*

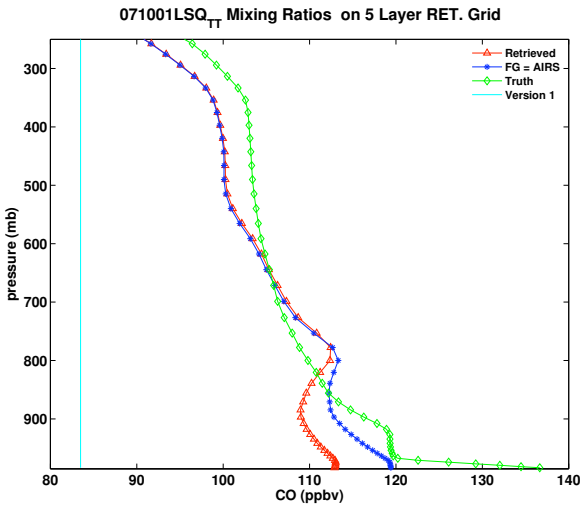

(c) AIRS First Guess

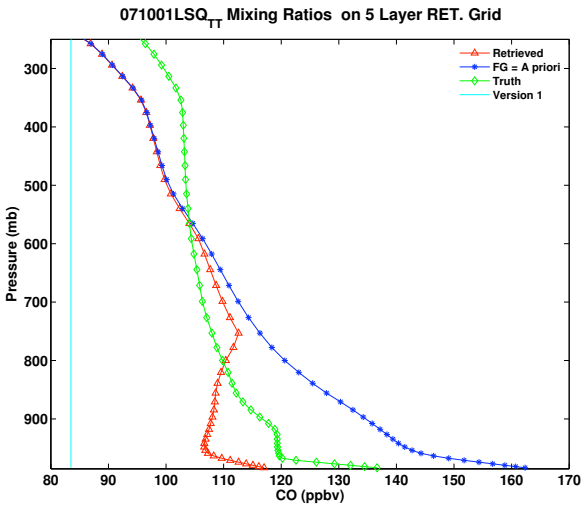

(d) *a priori*

Figure A.2: 5 layer retrieval using the NN bias spectruum and the LSQwAP retrieval equation on the merged profile grid measured in *ppbv*. (a) and (c) represent the retrieval days using AIRSv5 CO as the first guess profile. (b) and (d) represent the retrieval results using an *a priori* first guess.

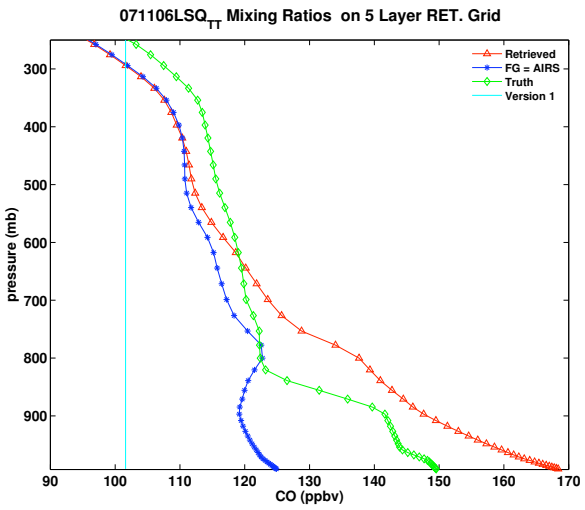

(a) AIRS First Guess

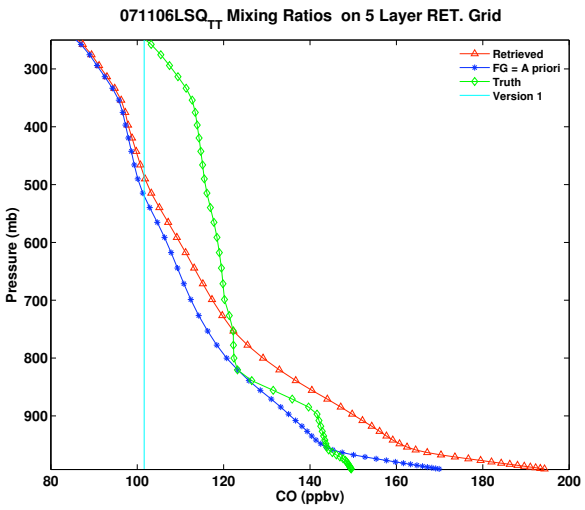

(b) *a priori*

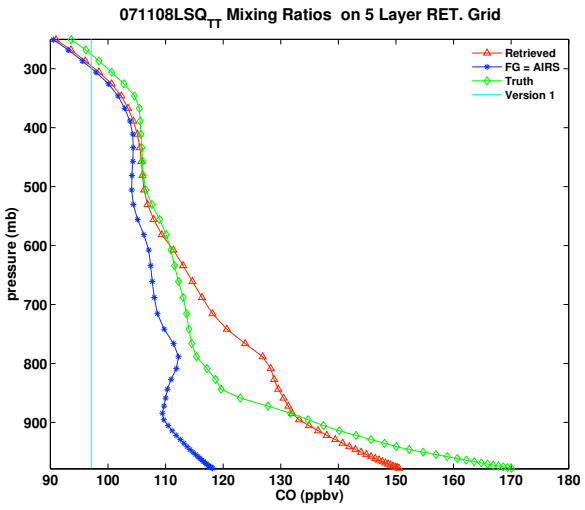

(c) AIRS First Guess

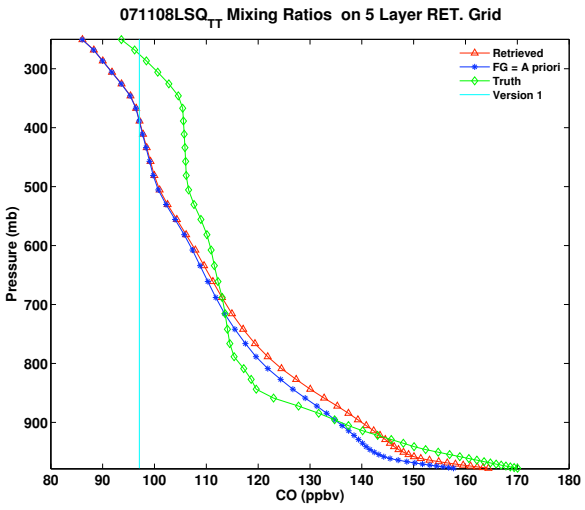

(d) *a priori*

Figure A.3: 5 layer retrieval using the NN bias spectruum and the LSQwAP retrieval equation on the merged profile grid measured in *ppbv*. (a) and (c) represent the retrieval days using AIRSv5 CO as the first guess profile. (b) and (d) represent the retrieval results using an *a priori* first guess.

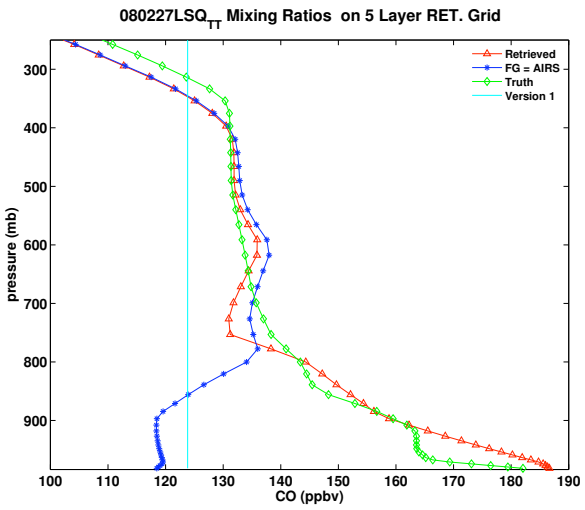

(a) AIRS First Guess

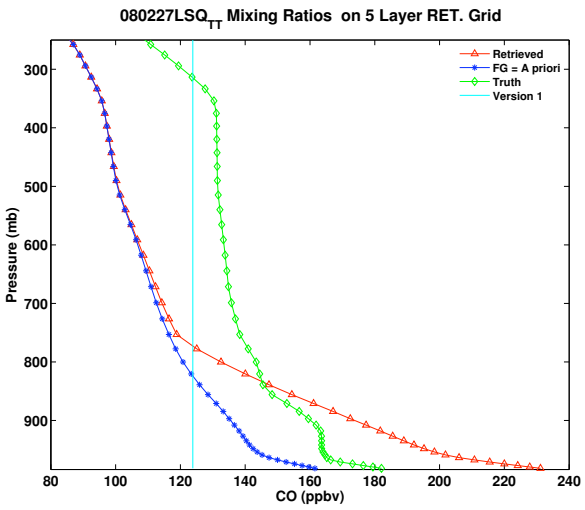

(b) *a priori*

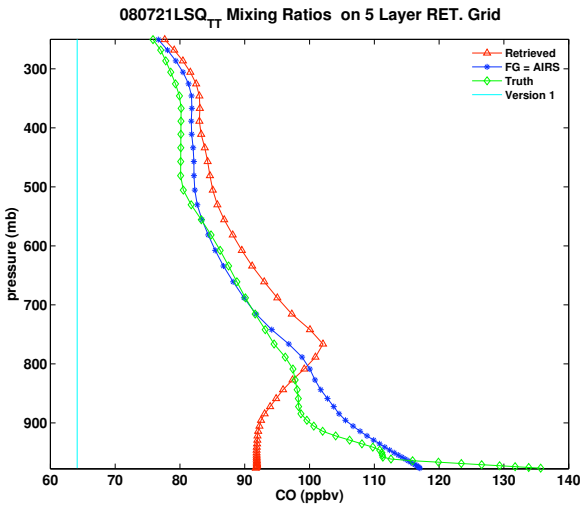

(c) AIRS First Guess

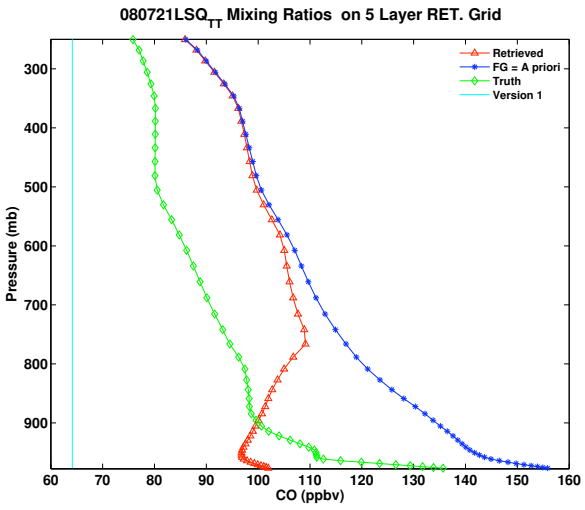

(d) *a priori*

Figure A.4: 5 layer retrieval using the NN bias spectruum and the LSQwAP retrieval equation on the merged profile grid measured in *ppbv*. (a) and (c) represent the retrieval days using AIRSv5 CO as the first guess profile. (b) and (d) represent the retrieval results using an *a priori* first guess.

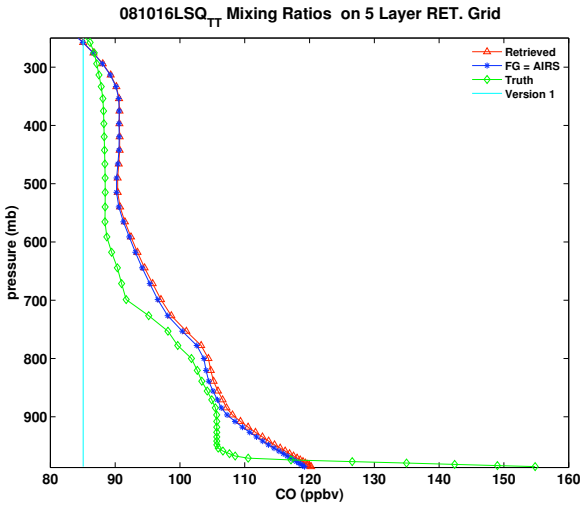

(a) AIRS First Guess

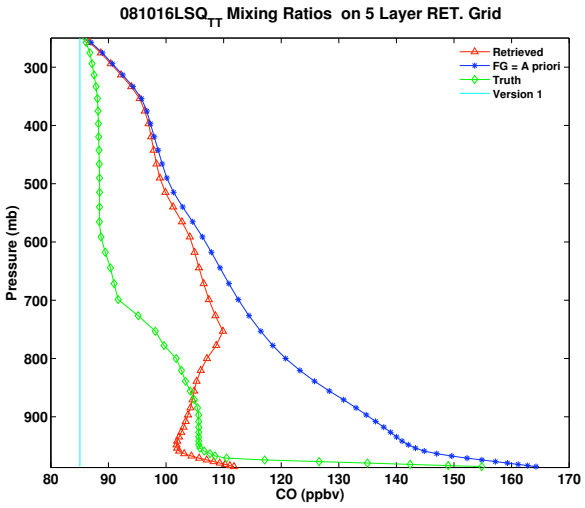

(b) *a priori*

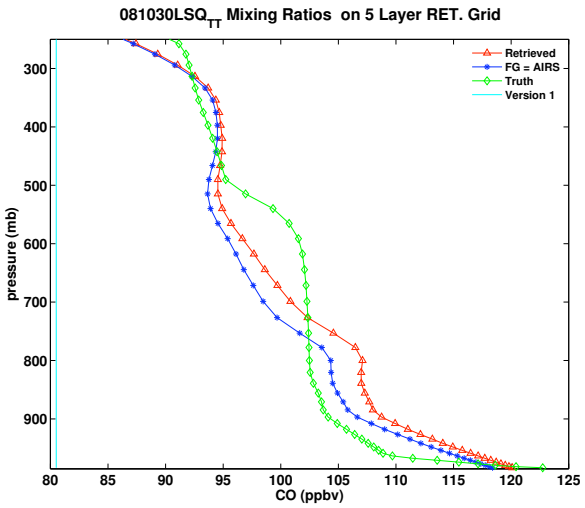

(c) AIRS First Guess

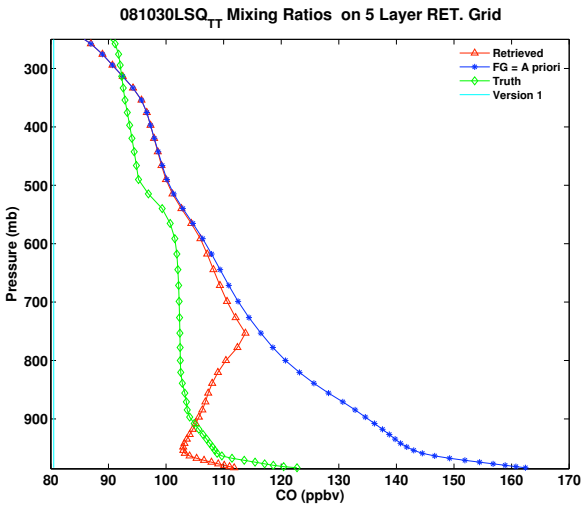

(d) *a priori*

Figure A.5: 5 layer retrieval using the NN bias spectruum and the LSQwAP retrieval equation on the merged profile grid measured in *ppbv*. (a) and (c) represent the retrieval days using AIRSv5 CO as the first guess profile. (b) and (d) represent the retrieval results using an *a priori* first guess.

References

[1] Antonelli, P., Revercomb, H., Sromovsky, L., Smith, W., Knuteson, R., Tobin, D., Garcia, R., Howell, H., Huang, H., and Best, F. A principal component noise filter for high spectral resolution infrared measurements. *J. Geophys. Res. 109*, D23102, doi:10.1029/2004JD004862 (2004).

[2] Aumann, H., and Pagano, R. Atmospheric infrared sounder on the earth observing system. *Opt. Eng. 33(3)* (March 1994), 776–784.

[3] Backus, G., and Gilbert, J. Uniqueness in the inversion of inaccurate gross earth data. *Phil. Trans. R. Soc. Lond. 266*, 123 (1970).

[4] Bakwin, P., Tans, P., and Novelli, P. Carbon monoxide budget in the northern hemisphere. *Geophys. Res. Lett 21* (1994), 433–436.

[5] Barnet, C., Blaisdell, J., and Susskind, J. Practical methods for rapid and accurate computation of interferometric spectra for remote sensing applications. *IEEE Trans. Geosci. Remote Sens. 38*, 1 (2000), 169–183.

[6] Beer, R. TES on the Aura mission: Scientific objectives, measurements and analysis overview. *IEEE Trans. Geosci. Remote Sens.* (44), 1102–1105.

[7] Biraud, S., Torn, M., and Riley, W. Regional carbon fluxes and atmospheric carbon dynamics in the southern great plains during the 2007 CLASIC intensive. In *Fall Meet. Suppl., Abstract* (2007), vol. 88(52) of *Eos Trans.*, AGU.

[8] Candy, J. *Signal processing, the modern approach*. McGraw-Hill Book Company, New York, 1988.

[9] Clerbaux, C., Edwards, D., Deeter, M., Emmons, L., Lamarque, J., Tie, X., Massie, S., and Gille, J. Carbon monoxide pollution from cities and urban areas observed by the Terra/MOPITT mission. *Geophys. Res. Lett 35, L03817*, doi:10.1029/2007GL03200 (2008).

[10] Clough, S., Kneizys, F., and Davies, R. Line shape and the water vapor continuum. *Atmos. Res. 23* (1989), 229–241.

[11] Crutzen, P. A discussion of the chemistry of some minor constituents in the stratosphere and troposphere. *Pure Appl. Geophys. 106-108* (1973), 1385–1399.

[12] Daniel, J., and Solomon, S. On the climate forcing of carbon monoxide. *J. Geophys. Res.* (1988).

[13] De Souza-Machado, S., Strow, L., Motteler, H., and Hannon, S. kCARTA: An atmospheric radiative transfer algorithm using compressed lookup tables. Tech. rep., Univ. Maryland Baltimore County, Dept. Physics, 2002.

[14] Deeter, M., Edwards, D., and Gille, J. Retrievals of carbon monoxide profiles from MOPITT observations using lognormal a priori statistics. *J. Geophys. Res. 112*, D11311, doi:10.1029/2006/JD007999 (2007).

[15] Dianov-Klokov, V., and Yurganov, L. A spectroscopic study of the global space-time distribution of atmospheric CO. *Tellus 33* (1981), 262–273.

[16] Dickerson, R. Boundary layer venting. Private Communication, 2011.

[17] Dickerson, R., Doddridge, B., Rhoads, K., and Kelley, P. Large-scale pollution of the atmopshere over the remote atlantic ocean: Evidence from Bermuda. *J. Geophys. Res. 100* (1995), 8945–8952.

[18] Dudhia, A., Victoria, L., and Rodgers, C. Microwindow selection for high spectral resolution sounders. *Appl. Opt. 41* (2002), 3665–3673.

[19] Duncan, B., Logan, J., Bey, I., Megretskaia, I., Yantosca, R., Novelli, P., Jones, N., and Rinsland, C. Global budget of CO, 1988-1997: Source estimates and validation with a global model. *J. Geophys. Res. 112*, D22301, doi:10.1029/2007JD008459 (2007).

[20] Fante, R. *Signal analysis and estimation: an introduction.* John Wiley and Sons, New York, 1988.

[21] Feltz, W., and Mecikalski, J. Monitoring High-Temporal-Resolution Convective Stability Indices Using the Ground-Based Atmospheric Emitted Radiance Interferometer (AERI) during the 3 may 1999 Oklahoma-Kansas Tornado Outbreak. *Wea. Forecasting 17* (2002), 445–455.

[22] Feltz, W., Smith, W., Howell, H., Knuteson, R., Woolf, H., and Revercomb, H. Near-continuous profiling of temperature, moisture, and atmospheric stability using the atmospheric emitted radiance interferometer (AERI). *J. Appl. Meteor. 42* (2002), 584–597.

[23] Firsov, K., and Chesnokova, T. Sensitivity of downward long-wave radiative fluxes to water vapor continuum absorption. *Enviromental Spectroscopy 23*, 6 (2010), 462–468.

[24] Fishman, J., and Crutzen, P. The origin of ozone in the troposphere. *Nature 274* (1978), 855–857.

[25] Han, Y., Shaw, J., Churnside, J., Brown, P., and Clough, S. Infrared spectral measurements in the tropical Pacific atmosphere. *J. Geophys. Res. 102* (1997).

[26] Hannon, S. KLAYERS operations. Private Communication, 2009.

[27] Hannon, S. Uncertainties of line strengths in kCARTA. Private Communication, 2011.

[28] He, H., McMillan, W., Knuteson, R., and Feltz, W. Tropospheric carbon monoxide column density retrieval during Prelaunch MOPITT Validation exercise. *Atmos. Environ. 35(3)*, ISSN 1352-2310, doi:10.1016/S1352-2310(00)00334-4 (2001), 509–514.

[29] Knuteson, R., Best, F., Ciganovich, N., Garcia, R., Hackel, D., Revercomb, H., Taylor, J., and Turner, D. E-AERI calibration performance certification. In *Multispectral, Hyperspectral, and Ultraspectral Remote Sensing Technologies, Techniques and Applications III, Incheon, Korea, 13-14 October 2010 (Proceedings)* (Bellingham, WA, 2010), no. Paper 78571L, SPIE International Society for Optical Engineering.

[30] Knuteson, R., Revercomb, H., Best, F., Ciganovich, N., Dedecker, R., Dirkx, T., Ellington, S., Feltz, W., Garcia, R., Howell, H., Smith, W., Short, J., and Tobin, D. Atmospheric emitted radiance interferometer. Part I: Instrument design. *J. Atmos. Oceanic Technol. 21* (2004), 1763–1776.

[31] Knuteson, R., Revercomb, H., Best, F., Ciganovich, N., Dedecker, R., Dirkx, T., Ellington, S., Feltz, W., Garcia, R., Howell, H., Smith, W., Short, J., and Tobin, D. Atmospheric emitted radiance interferometer. Part II: Instrument performance. *J. Atmos. Oceanic Technol. 21* (2004), 1777–1789.

[32] Kopacz, M., Jacob, D., Fisher, J., Logan, J., Zhang, L., Megretskaia, I., Yantosca, R., Singh, K., Henze, D., Burrows, J., Buchwitz, M., Khlystova, I., McMillan, W., Gille, J., Edwards, D., Eldering, A., Thouret, V., and Nedelec, P. Global estimates of CO sources with high resolution by adjoint inversion of multiple satellite datasets (MOPITT,AIRS,SCIAMACHY,TES). *Atmos. Chem. Phys. 10*, doi:10.5194/acp-10-855-2010 (2010), 855–876.

[33] Levy, H. Normal atmosphere: Large radical and formaldehyde concentrations predicted. *Science 173* (1971), 141–143.

[34] Lightner, K. *A Tropospheric Ozone Retrieval Using a Ground-Based Up-Looking Infrared Interferometer*. PhD thesis, University of Maryland Baltimore County, 2004.

[35] Liljergen, J. Two-channel microwave radiometer for observations of total column precipitable water vapor and cloud liquid water path. American Meteorological Society, pp. 262–269.

[36] Logan, J., Prather, M., Wofsy, S., and McElroy, M. Tropospheric chemistry: A global perspective. *J. Geophys. Res. 86(C8)* (1981), 7210–7254.

[37] Luke, W., Dickerson, R., Ryan, W., Pickering, K., and Nunnermacker, L. Tropospheric chemistry over the lower great plains of the United

States, 2, trace gas profiles and distributions. *J. Geophys. Res. 97* (1992), 20647–20670.

[38] Luo, M., and et al. TES carbon monoxide validation with DACOM aircraft measurements during INTEX-B 2006. *J. Geophys. Res. 112*, D24S48, doi:10.1029/2007JD008803 (2006).

[39] Maddy, E. Beer correlation coefficients. Private Communication, 2011.

[40] Maddy, E. Inverse methods class notes: Least square methods. Private Communication, 2011.

[41] Maddy, E., and Barnet, C. Vertical resolution estimates in version 5 of AIRS operational retrievals. *IEEE Trans. Geosci. Remote Sens. 46* (2008), 2375–2384.

[42] Maddy, E., Barnet, C., and Gambacorta, A. A computationally efficient retrieval algorithm for hyperspectral sounders incorporating a *priori* information. *IEEE Trans. Geosci. Remote Sens. Vol. 6*, NO. 4 (2009), 802 – 806.

[43] Malinowski, E. Determination of the number of factors and the experimental error in a data matrix. *Anal. Chem. 49* (1977), 612–617.

[44] Malinowski, E. Theory of error in factor analysis. *Anal. Chem. 49* (1977), 606–612.

[45] Mattioli, V., Westwater, E., and Morris, V. Monitoring of precipitable water vapor and cloud liquid path from scanning microwave radiometers during the 2003 cloudiness inter-comparisons experiment. In *Fourteenth ARM Science Team Meeting Proceedings* (March 2004), ARM.

[46] McMillan, W., Barnet, C., Strow, L., Chahine, M., McCourt, M., Warner, J., Novelli, P., Korontzi, S., Maddy, E., and Datta, S. Daily global maps of carbon monoxide from NASA's atmospheric infrared sounder. *Geophys. Res. Lett 32*, doi:10.1029/2004GL021821 (2005), L11801.

[47] McMillan, W., Evans, K., Barnet, C., Maddy, E., Sachse, G., and Diskin, G. Validating the AIRS version 5 CO retrieval with DACOM in situ measurements during INTEX-A and -B. *IEEE Trans. Geosci. Remote Sens. VOL. 49*, NO. 7 (2011), 2802 – 2813.

[48] McMillan, W., He, H., Doddridge, B., Feltz, W., Knuteson, R., McKernan, E., Pougatchev, N., Smith, W., Strow, L., Wang, J., and Yurganov, L. Validation of carbon monoxide retrievals from up-looking FTIR atmospheric thermal emission spectra in: Optical remote sensing of the atmosphere. *Optical Society of America Technical Digest 27* (1999), 163–165.

[49] McMillan, W., He, H., Strow, L., Doddridge, B., Knuteson, R., and Feltz, W. Sensitivity testing of carbon monoxide retrievals from uplooking FTIR atmospheric thermal emission spectra. Eos. Transactions Spring Meeting Supplement, 2000.

[50] McMillan, W., McCourt, M., Revercomb, H., Knuteson, R., Christian, T.J. Doddridge, B., Hobbs, P., Lukovich, J., Novelli, P., S.J., P., Sparling, L., Stein, D., Swap, R., and Yokelson, R. Tropospheric carbon monoxide measurements from the Scanning High-resolution Interferometer Sounder on 7 September 2000, in southern Africa during SAFARI. *J. Geophys. Res. 108*, doi:10.1029/2002JD002335 (2003), 8492.

[51] McMillan, W., Strow, L., Smith, W., and Revercomb, H. The detection of enhanced carbon monoxide abundances in remotely sensed infrared spectra of a forest fire smoke plume. *Geophys. Res. Lett 23*, 22 (1996), 3199–3202.

[52] McMillan, W., Strow, L., Smith, W., Revercomb, H., Huang, H., Ryan, W., Thompson, A., and McNamara, D. Remote sensing of CO over the continental US on September 12-13, 1993. *J. Geophys. Res. 102*, D9 (1997), 10695–10709.

[53] Mecikalski, J., Bedka, K., Turner, D., Feltz, W., and Paech, S. Ability to quantify coherent turbulent structures in the convective boundary layer using thermodynamic profiling instruments. *J. Geophys. Res. 111*, D12203, doi:10.1029/2005JD006456 (2006).

[54] Mickley, L. J., Murti, P., Jacob, D., Logan, J., Rind, D., and Koch, D. Radiative forcing from tropospheric ozone calculated with a unified chemistry-climate model. *J. Geophys. Res.* (1999).

[55] Mlawer, E., Clough, S., Brown, P., and Tobin, D. Recent developments in the water vapor continuum. In *of the 9th Atmospheric Radiation Measurement (ARM)* (San Antonio, Texas, 1999), ARM, pp. 503–511.

[56] Mlawer, E., Clough, S., and Tobin, D. A new water vapor continuum model: MT_CKD_1.0. In *Proc. 13th ARM Science Team Meeting* (2003), U.S. Dept. of Energy.

[57] Norton, R., and Beer, R. New apodizing functions for Fourier spectrometry. *J. Opt. Soc. Am. 66* (1976), 259–264.

[58] Norton, R., and Beer, R. Errata - New apodizing functions for Fourier spectrometry. *J. Opt. Soc. Am. 67* (1977), 419.

[59] Novelli, P., Connors, V., and Reichle Jr, H. An internally consistent set of globally distributed atmospheric carbon monoxide mixing ratios developed using results from an intercomparison of measurements. *J. Geophys. Res. 103*, (D15) (1998), 19285–19293.

[60] Novelli, P., Elkins, J., and Steele, L. The development and evaluation of a gravimetric reference scale for measurements of atmospheric carbon monoxide. *J. Geophys. Res. 96* (1991), 13109–13121.

[61] Novelli, P., Masarie, K., Lang, P., Hall, B., Myers, R., and Elkins, J. Reanalysis of tropospheric CO trends: Effects of the 1997-1998 wildfires. *J. Geophys. Res. 108(D15)*, doi:10.1029/2002JD003031 (2003), 4464.

[62] Potosnak, M., Wofsy, S., Denning, A., Conway, T., Munger, J., and Barnes, D. Influence of biotic exchange and combustion sources on atmospheric CO_2 concentrations in New England from observations at a forest flux tower. *J. Geophys. Res. 104* (1999), 9561–9569.

[63] Pougatchev, N., and Rinsland, C. Spectrscopic study of the seasonal variation of carbon monoxide vertical distribution above Kitt Peak. *J. Geophys. Res. 100* (1995), 1409–1416.

[64] Press, W., Teukolsky, S., Vetterling, W., and Flannery, B. *Numerical Recipes in C: The Art of Scientific Computing*, 2nd ed. Cambridge University Press, 1992.

[65] Revercomb, H., and Coauthors. The atmospheric radiation measurement (ARM) programs water vapor intensive observation periods: Overview, initial accomplishments, and future challenges. *Bull. Amer. Meteor. Soc. 84* (2003), 217–236.

[66] Rodgers, C. Characterization and error analysis of profiles retrieved from remote sounding measurements. *J. Geophys. Res. 95(D5)* (1990), 5587–5595.

[67] Rodgers, C. *Inverse Methods for Atmospheric Sounding Theory and Practice*, vol. 2. World Sci. Singapore, 2000.

[68] Rothman, L., Gordan, I., Barbe, A., Benner, D., Bernath, P., Birk, M., Boudon, V., Brown, L., Campargue, A., Champion, J., Chance, K., Coudert, L., Dana, V., Devi, V., Fally, S., Flaud, J., Gamache, R., Goldman, A., Jacquemart, D., Kleiner, I., Lacome, N., Lafferty, W., Mandin, J., Massie, S., Mikhailenko, S., Miller, C., Moazzen-Ahmadi, N., Naumenko, O., Nikitin, A., Orphal, J., Perevalov, V., Perrin, A., Predoi-Cross, A., Rinsland, C., Rotger, M., Simeckova, M., Smith, M., Sung, K., Tashkun, S., Tennyson, J., Toth, R., Vandaele, A., and Vander-Auwera, J. The HITRAN 2008 molecular spectroscopic database. *J. Quant. Spectrosc. Rad. Transfer 110*, doi:10.1016/j.jqsrt.2009.02.013 (2009), 533–572.

[69] Rothman, L., Jacquemart, D., Barbe, A. an Benner, D., Birk, M., Brown, L., Carleer, M., Chackerian, C., Chance, K., Coudert, L., Dana, V., Devi, V., Flaud, J., Gamache, R., Goldman, A., Hartmann, J., Jucks, K., Maki, A., Mandin, J., Massie, S., Orphal, J.,

Perrin, A., Rinsland, C., Smith, M., Tennyson, J., Tolchenov, R., Toth, R., Vander-Auwera, J., Varanasi, P., and Wagner, G. The HITRAN 2004 molecular spectroscopic database. *J. Quant. Spectrosc. Rad. Transfer 96* (2005), 139–204.

[70] Shannon, C., and Weaver, W. *The Mathematical Theory of Communication.* University of Illinois Press, Urbana, 1962.

[71] Shindell, D., Faluvegi, G., Stevenson, D., Krol, M., Emmons, L., Lamarque, J. P. G., Dentener, F., Ellingsen, K., Schultz, M., Wild, O., Amann, M., Atherton, C., Bergmann, D., Bey, I., Butler, T., Cofala, J., Collins, W. J., Derwent, R., Doherty, R., Drevet, J., Eskes, H., Fiore, A., Gauss, M., Hauglustaine, D., Horowitz, L., Isaken, I., Lawrence, M., Montanaro, V., Muller, J., Pitari, G., Prather, M., Pyle, J., Rast, S., Rodriguez, J., Sanderson, M., Savage, N., Strahan, S., Sudo, K., Szopa, S., Unger, N., Van Noije, T., and Zeng, G. Multimodel simulations of carbon monoxide: Comparison with observations and projected near-future changes. *J. Geophys. Res. 111*, D08302, doi:10.1029/2006JD007100 (2006).

[72] Smith, W., Feltz, W., Knuteson, R., Revercomb, H., Woolf, H., and Howell, H. The retrieval of planetary boundary layer structure using ground-based infrared spectral radiance measurements. *J. Atmos. Oceanic Technol. 16* (1999), 323–333.

[73] Stephens, G. *Remote sensing of the lower atmosphere.* Oxford University Press, 1994.

[74] Susskind, J., Barnet, C., and Blaisdell, J. Retrieval of atmospheric and surface parameters from AIRS/AMSU/HSB data in the presence of clouds. *IEEE Trans. Geosci. Remote Sens. 41*, doi 10.1109/TGRS.2002.808236 (2003), 390–409.

[75] Susskind, J., Blaisdell, J., Iredell, L., and Keita, F. Improved temperature sounding and quality control methodology using AIRS/AMSU data: The airs science team version 5 retrieval algorithm. *IEEE Trans. Geosci. Remote Sens.* (2011).

[76] Sussmann, R., and Borsdorff, T. Technical note: Interference errors in infrared remote sounding of the atmosphere. *Atmos. Chem. Phys. 7*, doi:10.5194/acp-7-3537-2007 (2007), 3537–3557.

[77] Tobin, D., and Coauthors. Downwelling spectral radiance observations at the SHEBA ice station: Water vapor continuum measurements from 17 to 26 μm. *J. Geophys. Res. 104* (1999), 2081–2092.

[78] Turner, D. Turner cloud flags. Private Communication, 2011.

[79] Turner, D., Feltz, W., and Ferrare, R. Continuous water profiles from operational ground-based active and passive remote sensors. *Bull. Amer. Meteor. Soc. 81* (2000), 1301–1317.

[80] Turner, D., and Gero, P. Downwelling 10 μm radiance temperature climatology for the atmospheric radiation measurement southern great plains site. *J. Geophys. Res. 116*, D08212, doi:10.1029/2010JD015135 (2011).

[81] Turner, D., Knuteson, R., Revercomb, H., Lo, C., and Dedecker, R. Noise reduction of atmospheric emitted radiance interferometer (AERI) observations using principal component analysis. *J. Atmos. Oceanic Technol. 23* (2006), 1223–1238.

[82] Turner, D., Tobin, D., Clough, S., Brown, P., Ellingson, R., Mlawer, E., Knuteson, R., Revercomb, H., Shippert, T., and Smith, W. The QME AERI LBLRTM: A closure experiment for downwelling high-spectral resolution infrared radiance. *J. Atmos. Sci. 61*, doi:10.1175/JAS3300.1 (2004), 2657–2675.

[83] Turquety, S., Hurtmans, D., Hadji-Lazzaro, J., Coheur, P., Clerbaux, C., Josset, D., and Tsamalis, C. Tracking the emission and transport of pollution from wildfires using the IASI CO retrievals: analysis of the summer 2007 Greek fires. *Atmos. Chem. Phys. 9*, doi:10.5194/acp-9-4897-2009 (2009), 4897–4913.

[84] Twomey, S. *Introduction to the Mathematics of Inversion in Remote Sensing and Indirect Measurements*. Developments in Geomathematics 3. Elsevier Scientific Publishing Company New York, 1977.

[85] Vanasse, G., Ed. *Spectrometric Techniques*, vol. I. Academic Press, New York, 1977.

[86] Wark, D., and Fleming, H. Indirect measurements of atmospheric temperature profiles from satellites: I. introduction. *Monthly Weather Review 94*, 6 (1966).

[87] Warner, J. Class notes on a priori. Inverse Methods Class Notes: A priori, 2011.

[88] Warner, J., Strow, L., Barnet, C., Sparling, L., Diskin, G., and Sachse, G. Improved agreement of AIRS tropospheric carbon monoxide products with other EOS sensors using optimal estimation retrievals. *Atmos. Chem. Phys. 10* (2010), 9521–9533.

[89] Wei, Z., and Warner, J. AIRS CO measurements over SGP. Private Communication, 2011.

[90] Yurganov, L., McMillan, W., Wilson, C., Fischer, M., Biraud, S., and Sweeney, C. Carbon monoxide mixing ratios over oklahoma between 2002 and 2009 retrieved from atmospheric emitted radiance interferometer spectra. *Atmos. Meas. Tech. 3*, doi:10.5194/amt-3-1319-2010 (2010), 1319–1331.

[91] Zander, R., Demoulin, P., Ehhalt, D., Schmidt, U., and Rinsland, C. Secular increase of total vertical column abundance of carbon monoxide above central europe since 1950. *J. Geophys. Res. 94* (1989), 11021–11028.